Faculdade de Engenharia da Universidade do Porto

FEUP

Computational techniques for automated analysis of animal tissue histological images

Frederico A. R. B. Junqueira

Master Thesis

Integrated Masters in Bioengineering

Supervisor:
Prof. João Manuel R. S. Tavares
Associate Professor of the Mechanical Engineering Department, FEUP

Co-Supervisor:
Augusto Manuel Rodrigues Faustino
Associate Professor of the Pathology and Molecular Immunology Department ICBAS

June 2015

Agradecimentos

Em primeiro lugar quero agradecer ao Professor João Tavares pela disponibilidade e aconselhamento fornecidos ao longo destes últimos meses. Sem a sua orientação este trabalho não seria possível. Quero agradecer também ao Professor Augusto Faustino pela sua disponibilidade, simpatia e vontade de ajudar.

Quero agradecer do fundo do coração à Lia, que me acompanhou a 100% nesta jornada longa e nunca me deixou perder o Norte. Sem o seu carinho, muita paciência e apoio incondicional este trabalho não estaria completo.

À minha mãe, ao meu pai, à minha irmã, ao meu irmão e a minha avó pelas gargalhadas, carinho e todo o apoio nesta etapa final.

Ao Pedro pelos bons conselhos e ombro amigo sempre que precisei.

Ao companheiros da tese Morgana, Jessica e Ricardo por me ouvirem nos momentos de stress.

“Everybody has a plan until he gets punched in the face.”
Myke Tyson

Resumo

O estudo de tecidos celulares fornece uma incontestável fonte de conhecimento e compreensão acerca do corpo humano e do ambiente que o rodeia. Aceder a esta informação é, portanto, crucial para determinar e diagnosticar uma grande variedade de patologias, detetáveis somente ao nível microscópico. A histologia desempenha um papel importante na observação de células e suas características anatómicas, e igualmente para o diagnóstico clínico de patologias involvendo uma anormal conformação celular. Nas imagens histológicas, algoritmos de segmentação semi-automáticos ou automáticos são capazes de separar e identificar estruturas celulares de acordo com as suas diferenças morfológicas. Estes algoritmos de segmentação são a primeira abordagem a sistemas de visão computacional e, no que respeita à histopatologia, o diagnóstico automático de imagens histológicas. Como as amostras histológicas têm uma espessura reduzida, as características volumétricas são quase imperceptíveis, correespondendo a perdas de informação valiosas, principalmente topográficas e volumétricas, críticas para um correcto diagnóstico.

Consequentemente, a combinação de algoritmos de segmentação e reconstrução 3D aplicados a datasets de imagens histológicas fornecem uma maior informação acerca da patologia analisada e estruturas microscópicas, destacando regiões anormais.

Tendo isto em consideração, o presente trabalho focou-se em desenvolver algoritmo computacional automático capaz de realizar reconstrução 3D de superfícies de tecidos relevantes em secções histológicas 2D. Uma primeira abordagem foi desenvolvida focada em destacar as estruturas relevantes nas secções de tecido. Depois, um estudo feito com base em algoritmos de registo de imagem foi levado a cabo para descobrir qual a metodologia mais indicada para alinhar as secções provenientes de datasets de imagens. Combinando os melhores métodos de processamento e registo de imagem (resultado DICE para caso 1: ; resultado DICE para caso 2: ; resultado DICE para caso 3:), avaliados em abordagens prévias, em conjunto com um algoritmo de reconstrução 3D foi possível uma representação volumétrica das estruturas de tecidos pertinentes do dataset de imagens alinhadas.

Abstract

The study of cellular tissues provides an incontestable source of information and comprehension about the human body and the surrounding environment. Accessing this information is, therefore, crucial to determine and diagnose a wide variety of pathologies detectable only at a microscopic scale. Histology plays an important role in the observation of cells and their anatomical features, and so for clinical diagnosis of all the pathologies involving abnormal cellular conformation. In the histological images, semi-automated or automated segmentation algorithms are able to separate and identify cellular structures according to morphological differences. These segmentation algorithms are the first approach for computational vision systems and, concerning histopathology, the automated diagnose of histological images. Since the histological samples are thin, the volumetric features are almost unnoticeable, corresponding to losses of valuable information, mainly topographical and volumetric data, critical for a correct diagnostic.

Hence, the combination of segmentation and 3D reconstruction algorithms applied to histological image datasets provides more information about the analysed pathology and microscopic structures, highlighting abnormal areas.

Taking this into consideration, the present work focussed on developing an automatic computational algorithm capable of performing the 3D surface reconstruction of relevant tissue structures of 2D histological slices. A first approach was developed fixed on highlighting the relevant structures from the tissue sections. After that, a study on image registration algorithms was conducted to find the most suited methodology to align the slices from histological image datasets. Combining the top-performing image processing and registration methods (DICE score: 0.9267±0.0337 for Case 1; 0.9367±0.0356 for Case 2; 0.9683±0.0283 for Case 3), evaluated in the previous approaches, with a 3D surface reconstruction algorithm it was possible to calculate a volumetric representation of the pertinent tissue structures from the aligned image dataset.

Contents

List of Figures

List of Tables

Abbreviations and Acronyms

CNS	Central Nervous System
CT	Computer Tomography
ECM	Extracellular Matrix
H & E	Haematoxylin and Eosin
HSV	Hue – Saturation - Value
ITK	Insight Segmentation and Registration Toolkit
μm	Micrometer
mm	Millimeter
MRI	Magnetic Resonance Imaging
nm	Nanometer
PCA	Principal Component analysis
PET	Positron Emission Tomography
PNS	Peripheral Nervous System
3D	Three Dimensions
2D	Two Dimensions
RGB	Red – Green - Blue
CLAHE	Contrast Limited Adaptive Histogram Equalization
OD	Optical Density

Chapter 1

Introduction

1.1 - Motivation

Histological studies provide an important help in the understanding of some complex pathophysiological processes concerning diseases at the cellular scale. These studies are considered the gold standard for assessing the natural response of a cellular tissue in face of a pathology or therapeutic intervention (Chakravarty, Bedell et al. 2008). To produce histopathology slides, a rather complex protocol must be executed involving a substantial amount of human labor and information processing (Randell, Ruddle et al. 2012).

Although in-vivo imaging techniques, such as the MRI and PET, assess anatomical and pathological information without invasive procedures, they require extensive validation when compared to histological ex-vivo examinations (Chakravarty, Bedell et al. 2008).

Visual interpretation, the core of most medical diagnostic procedures and the final diagnostic decision for cancer and other diseases, is based on tissue examination. This method requires a long time, intensive manual labor to produce viable results and presents a sampling bias that promotes intra- and inter-reviewer discrepancies when analysing histological tissues (Sertel, Kong et al. 2009). Thus, it is clear the need for automated processes concerning morphology diagnostics in medicine, to improve the diagnostic accuracy and provide a fast and reliable second opinion to histopathologists. Automated systems can reduce human factor mistakes and increase the speed of diagnostic processes (Nedzved, Belotserkovsky et al. 2005).

The volumetric data analysis from relevant tissue structures visible from 2D histological slices is not often a straightforward process, requiring a great amount of experience from histopathologists (Koshi, Holla et al. 1997). Therefore, three dimensional reconstruction of tissue samples at a microscopic resolution reveals significant potential to improve the study of disease processes when structural or spatial modifications are involved (D. 1978). The combination of 3D image reconstruction methodologies with staining techniques provides a better understanding on functional information concerning the cellular structures (Roberts, Magee et al. 2012).

Hence, there is an urge to develop fully automated approaches for tissue analysis in histological section images, combining the best computational methods to produce an accurate and reliable 3D reconstruction algorithm, enhancing this way the medical study and clinical diagnostic of various diseases. The implementation of these algorithms could provide a better insight into the intricate spatial relations between the studied cell tissues and surrounding tissues.

With this in mind, a computational framework was developed in this study, composed by several image processing and registration algorithms and culminating in a 3D tissue reconstruction method. To accomplish this, a previous literature review was performed on the most suited methods to perform each task, as well as histological image notions, crucial to correctly analyse the image datasets tested to validate the developed algorithm, and also to define the relevant tissue structure to be reconstructed.

1.2 - Objectives

The present study aimed, primarily, the review and evaluation of currently implemented image processing and registration techniques in the literature, ranging from standard pre-processing methods to complex image registration frameworks, and recently developed algorithms for histological image analysis.

With all the concepts and information gathered from the literature review, it was possible to pursue the main goal of this study, which consisted in the development of a completely automatic computational framework, capable of performing accurate histological image alignment and 3D reconstruction of tissues. Therefore, providing detailed volumetric information concerning relevant tissues features, unobtainable through 2D conventional slice analysis. The objectives behind each step developed for the final framework, are explained below.

Image pre-processing – first step, developed to accomplish the highest color differentiation between tissues with distinct stains, with several contrast enhancement methods being tested.

Image segmentation – aiming to provide the most accurate discrimination between different tissue stains and/or other interesting structures in the histological images, previously pre-processed.

Image registration – for the implementation of this step, the great focus was to achieve the most correct slice alignment, thus, mimicking the original disposition of histological tissues in natural conditions, before the tissue preparation procedure.

3D surface reconstruction – this final procedure enables the interpolation and surface reconstruction of the previously processed and aligned stack of slices. The main objective with this step is to provide detailed three dimensional insight over commonly studied 2D tissue structures, such as neoplasic tissues.

1.3 - Document Structure

The present work is divided in 4 chapters, besides the introduction. A brief description on the contents and subjects addressed in each one is provided below.

Chapter 2 - Literature Review: On this chapter, an introduction to histology and its importance as a way to assess cellular responses to pathogens or treatments at a microscopic level is addressed, as well as the standard histological tissue sample preparation, for microscopic observation. This last topic is also discussed, including standard and recent techniques to perform microscopic observation on histological tissue sections. In this chapter, it is also presented a review on both standard and recently developed image processing methods, including pre-processing techniques, segmentation methods and registration algorithms, implemented on stained histological images.

Chapter 3 – Methodology: This chapter describes the implemented methodology in this project, approaching first the pre-processing techniques tested, followed by image registration frameworks and culminating in the final workflow. The histological image dataset used to test the developed computational framework is also described in this chapter.

Chapter 4 – Results and Discussion: In this chapter, all the results obtained either from pre-processing methods, segmentation or registration methodologies are presented and systematically discussed.

Chapter 5 – Conclusion: This last chapter, comprehends the final conclusions about the results, obtained through the performed study, in addition to future development perspectives.

1.4 - Principal Contributions

The principal contributions provided by the present work can be subdivided into two domains: the literature review and the developed computational framework.

The literature review presented represents an introduction to researchers or developers interested and unfamiliar with histological tissue image processing methods, to fundamental histology concepts as well as computational techniques, ranging from image pre-processing to image registration algorithms, suited for histological tissue samples. Furthermore, it also presents current state of the art methodologies for image registration, implemented in histological image datasets, which obtained successful slice alignment results.

The pre-processing preliminary evaluation on color space transformation methods, best suited to enhance color contrast in stained tissue images, is complete and the resultant image examples presented in this document provide a great insight on these simple algorithms to increase RGB color contrast, not only applicable to histological slices. The CLAHE-red technique was conceived for the present work, and it was proven to be the best pre-processing method to enhance stain contrast in H & E histological images, originating accurate tissue segmentation results, with simple clustering methods (kmeans).

The stain deconvolution algorithm, despite being based on previous works on the literature, the computational framework that enabled automatic stain discrimination was conceived and developed in this project. This was accomplished using simple techniques and the results obtained were consistent for most of the tested histology slices.

The entire computational framework proposed in this project enables the reconstruction of a three dimensional volume based on real histological tissue structures. It was achieved through the implementation of computationally cheap algorithms, and were obtained highly detailed volumetric representation, not only of differently stained tissues but also, in some cases, the accurate reconstruction of neoplasic tissues, present in the considered histological image datasets.

Chapter 2

Literature Review

This chapter presents the essential concepts required to understand the topics under study as well as all the research done so far on the subject.

Firstly, it will be presented an overview on the histological concepts concerning the current laboratory approach for acquisition of samples, as well as the relevant features of the different types of cellular tissues, since these images from the tissue samples represent the case study of this project.

A study on the most suitable computational methods to process and extract information from the histological images is reviewed and analyzed further in this chapter. This literature review culminates in the presentation and analysis of the most accurate 3D reconstruction algorithms for biological images, regarding the future reconstruction of certain relevant portions of cellular tissues in the histological samples.

2.1. Histology

Histology is the science that is devoted to study the detailed morphology of cells and tissues concerning the way in which these constitute the different organs in the body, at a microscopic level. The methods implemented by histologists require the study of living cells outside the conditions in which their development is natural, imposing a controlled environment (Junqueira and Carneiro 1987).

Histological studies provide an important help in the understanding of some complex pathophysiological processes concerning diseases at the cellular scale. Since these studies are also fundamental to evaluate the performance of new therapies and drug agents, they are considered the gold standard for assessing the natural response of a cellular tissue in face of a pathology or therapeutic intervention (Chakravarty, Bedell et al. 2008). The histological investigation, or the analysis of cell structures and tissues of different parts of the human body, is the focus of medical morphology, which is considered the most decisive method in the diagnostic of several human diseases (Nedzved, Belotserkovsky et al. 2005). Histopathologists can diagnose cancer and other pathologies through the observation under the microscope of sections of human or animal tissues (Randell, Ruddle et al. 2012). This histopathological diagnostic can be attained, for example, through the knowledge of some particular histological patterns, visible at the microscope, that are specific for a certain tumour or group of tumours, thus helping to provide and deliver the adequate treatment (Dive, Bodhade et al. 2014).

Considering that histological studies require biopsies or ex-vivo models, considering animal examinations (impossible to perform in live specimens), to assess disease and therapeutic efficiency tests results, these methods present serious disadvantages when compared to powerful imaging methods, such as high-resolution magnetic resonance imaging (MRI) and positron emission tomography (PET) scanners that are non-invasive and can be performed in in-vivo models, enabling longitudinal studies of the same specimen. Despite these advantages, the last methods require an extensive validation when compared to the gold-standard ex-vivo methods (histological observations) (Chakravarty, Bedell et al. 2008), highlighting the relevance of the histological methods nowadays.

Further in this section, the fundaments of histology are introduced and the procedure involved in the production of tissue samples for microscopic observation, as well as the different tissue types existent in the human body are explained.

2.1.1. Tissue Types

All tissues share the same basic biological components, cells and extracellular matrix (ECM). The latter is constituted by a complex and deeply organized network of biomolecules that surrounds the cells forming an intensive connection, in order to grant and supply all the necessary nutrients and molecules demanded by the organism (Junqueira and Carneiro 1987).

The human body is composed by four principal types of cellular tissues, the epithelial tissue, the connective tissue, the muscle and the nervous tissue. The functional, structural, molecular and visual characteristics of these four types of tissue are explored bellow.

Epithelial tissue is formed by tightly united sections of cells that cover all body surfaces, such as skin and intestine (except the articular cartilage), and represent the functional units of secretory glands. The epithelium presents a reduced amount of ECM and it stands over a basement membrane, a thin layer of specialized ECM that supports the epithelial structure providing mechanical bracing, attachment site and acts as a selective filtration barrier. The epithelial tissue can be classified in three main categories according to the number of cell layers that compose the tissue. Simple epithelia is formed by one layer of cells and the Stratified epithelia by two or more layers of cells. The third type is the Pseudostratified epithelia that, despite being also composed by one layer, not all the cells contact with the epithelium's surface resulting in an irregular distribution of the cell's nucleus. These categories can be subdivided, based on the shape of the cells present in the surface layer in squamous, cuboid and columnar (note: epithelia is the plural form of epithelium) (Junqueira and Carneiro 1987, Paulsson 1992, Kierszenbaum 2007). Figure 1 illustrates the different categories of epithelial tissue.

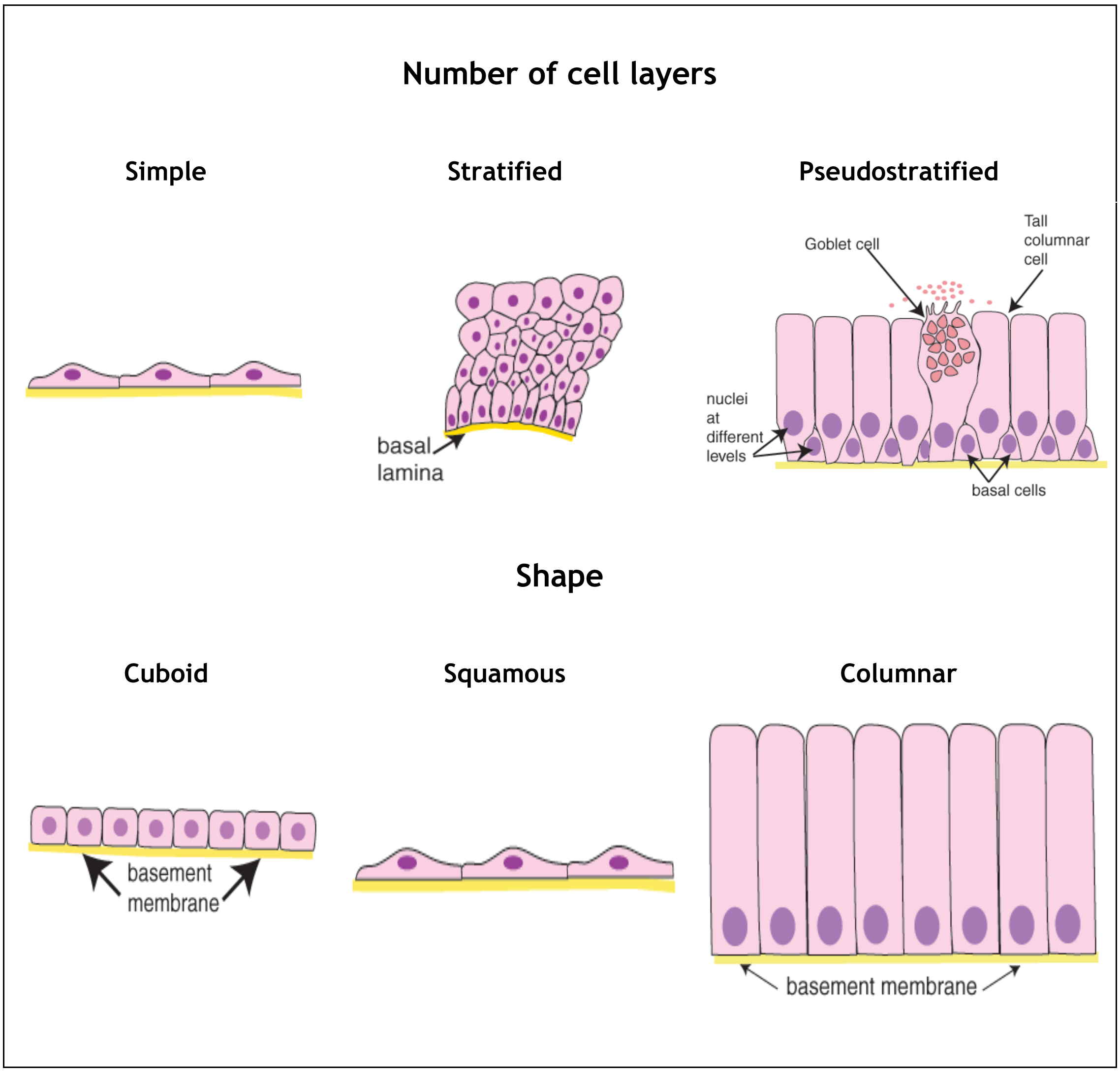

Figure 1. Epithelial tissue classification according to the number of cell layers and cellular shape. Adapted from Leeds University Histology Guide (Michelle Peckham 2003).

Connective tissue is responsible for providing a support and connection structure for all other tissues and cells of the body, contributing to its shape maintenance. The connective tissue is formed by ECM and cells but, unlike the epithelium, the intercellular distance is greater, due to the large presence of ECM components in tissue, surrounding the cells. Concerning the extracellular matrix composition, it is a combination of a large number of biomolecules, namely collagen (the most abundant), elastin (provides elastic resilience to the connective tissue), fibronectin with the role of matrix's structure organizer, glycoproteins and proteoglycans (Kierszenbaum 2007, Halper and Kjaer 2014).

The connective tissue can be classified in embryonic, adult and specialized connective tissue. The embryonic tissue is an unconstrained tissue developed during early embryonic stages, present in the umbilical cord. Adult connective tissue comprises a large diversity of structures due to the variable cell-to-ECM ratio, therefore leading to the subdivision in two types of tissue, the loose and the dense connective tissue. Loose tissue exhibits more cells than collagen fibers, and it is mainly present in the vicinity of nerves, blood vessels and muscles. On the other hand, the dense connective tissue is richer in ECM fibers, and it is present in tendons, ligaments and the dermis (skin). Specialized connective tissue includes tissues with special properties such as the adipose tissue, cartilage, bone and bone marrow tissue (Kierszenbaum 2007).

Examples of the abovementioned adult connective tissues can be visualized in Figure 2.

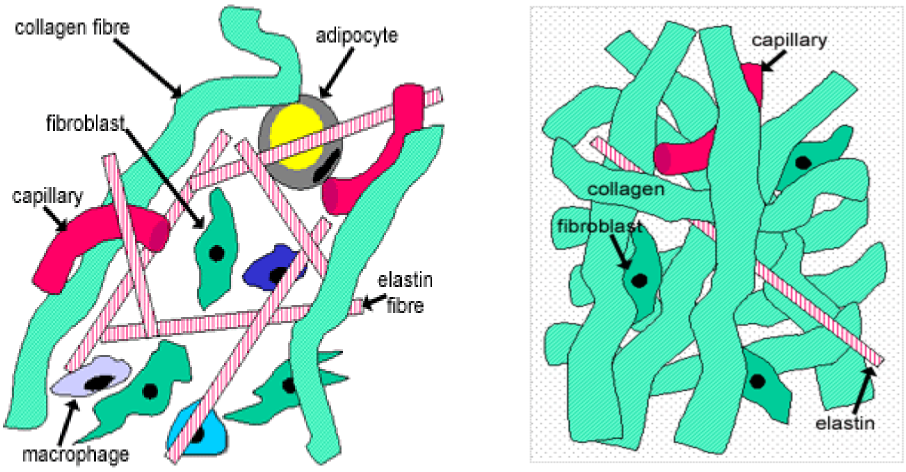

Figure 2. Representative images from adult loose connective tissue (left) and adult dense connective tissue (right). Adapted from Leeds University Histology Guide (Michelle Peckham 2003).

Muscle tissue consists of elongated cells, the myofibers, especially designed for contraction, which is promoted by the mechanical energy produced in the cells. The cellular membrane of muscle cells is the sarcolemma and the cytosol is denominated sarcoplasm.

The muscle tissue is divided in three types: skeletal, cardiac and smooth muscles. The skeletal muscle is composed of bundles of long, cylindrical and multinucleated cells exhibiting transverse striations. This muscle tissue contract voluntarily in a fast and vigorous way. In the skeletal muscle fibers, the various nucleus are located in the peripheral part, a distinguishing factor when comparing to the cardiac muscles. The cardiac muscle cells present transverse striations, one or two centered nucleus as well as an elongated and ramified shape. These cells are united by intercalated disks and exhibit involuntary, vigorous and rhythmic contraction. The cardiac fibers are surrounded by a sheath of connective tissue that assures the muscle with a wide capillary network. The smooth muscle is originated from the aggregation of long cells, thicker in the center. This muscle tissue is coated by a basement membrane and structurally supported by a set of reticular fibers, enabling the simultaneous contraction of the entire muscle (Junqueira and Carneiro 1987, Kierszenbaum 2007). Illustrative images on the several types of muscles are shown in Figure 3, 4 and 5.

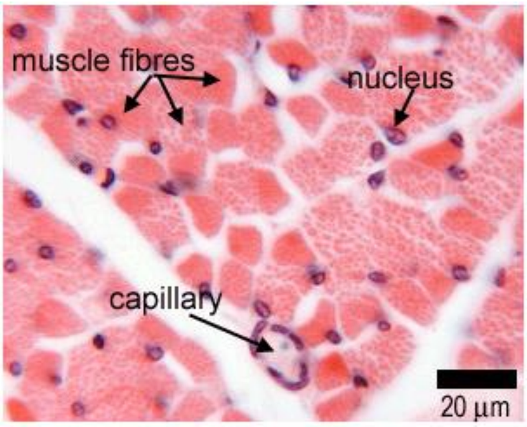

Figure 3. Histological image showing a transverse section of skeletal muscle. Adapted from Leeds University Histology Guide (Michelle Peckham 2003).

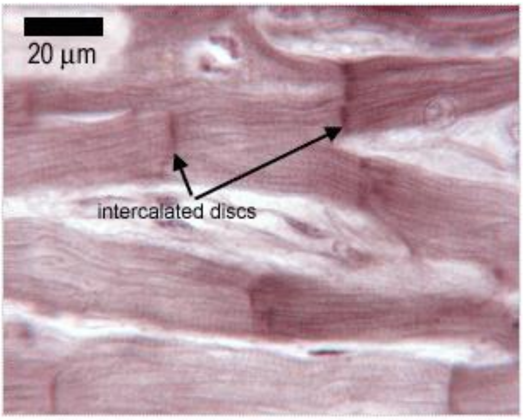

Figure 4. Histological image showing cardiac muscle. Adapted from Leeds University Histology Guide (Michelle Peckham 2003).

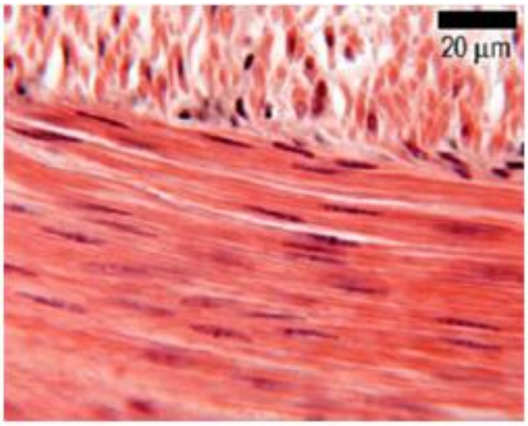

Figure 5. Histological image from a section of smooth muscle. Adapted from Leeds University Histology Guide (Michelle Peckham 2003).

Nervous tissue interconnects itself in the body to create a network, the nervous system, which is divided into two subsystems, the central nervous system (CNS) and the peripheral nervous system (PNS). The brain and spinal cord are the major components of the CNS while the PNS comprises the nerves (extensions of the neurons, nervous cells) and peripheral ganglia, establishing the connection with the CNS. The nervous system is responsible for the detection of sensorial stimuli from the exterior environment, integration of the received sensorial information, coordination of vital functions in the body and transmission of motor stimulus to the muscles (Junqueira and Carneiro 1987, Kierszenbaum 2007).

The nervous tissue in the CNS is the combination of neurons and glial cells, the latter ensuring structural support and correct conditions in the neurons' membrane for the transmission of electric signals. In the CNS there is a separation between the neurons' cellular body and their extensions, corresponding to two visually distinct sections, the gray matter and the white matter (both sections contain glial cells) (Junqueira and Carneiro 1987). A histological sample of nervous tissue illustrating both white and grey matter is shown in Figure 6.

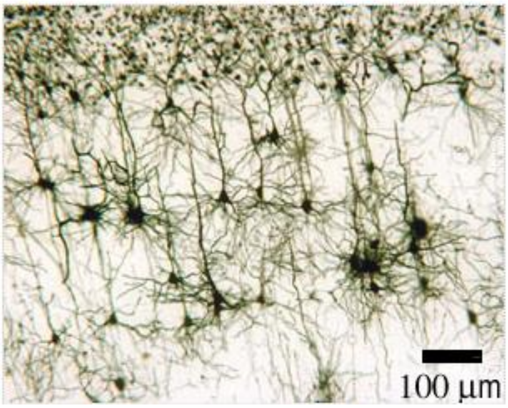

Figure 6. Histological image showing a section from cerebral cortex, stained with Golgi-Cox method (stains neurons in black). Adapted from Leeds University Histology Guide (Michelle Peckham 2003).

2.1.2. Sample Preparation

Considering that histology is the visualization of cells under the microscope, certain procedures must be performed in order to obtain thin tissue samples (slides) of the organ or biological structure under study. The process to study cellular tissues at the optical microscope (described in more detail in section 2.1.3) consists in the preparation of histological sections or slides (Junqueira and Carneiro 1987). To produce these slides, a rather complex protocol must be executed involving a substantial amount of human labor and information processing (Randell, Ruddle et al. 2012).

The specimens for analysis can range from small pieces of tissue collected from biopsies to entire organs. Most of these specimens are thick and cannot be traversed by light, thus justifying the slicing in thinner portions. The production process of glass slides consists, first, of a dissection step to, as already said, obtain tissue portions where the disease or area of interest is macroscopically located. Then, these tissue sections are chemically processed in a fixation step, followed by an inclusion procedure and after this, a new cut in the tissue block is performed using a microtome, a high precision cutting device, to obtain the final glass slice thickness (5 µm). An important staining procedure is performed finally in the tissue slides to increase the contrast of certain cellular structures (Junqueira and Carneiro 1987, Randell, Ruddle et al. 2012). A more detailed explanation on the fixation, inclusion and staining processes is presented below.

- **Fixation -** the purpose of this process is to toughen and preserve the microstructure and molecular composition of the tissue, thus avoiding the enzymatic and bacterial digestion. The fixation process involves the immersion of the tissue sample in a denaturizing and stabilizing solution, which diffuses itself and penetrates into the interior of the sample. The most widely used fixation agent for observation in optical microscopy is a solution of formaldehyde at 4% (Junqueira and Carneiro 1987).
- **Inclusion -** In order to obtain thin sections for microscope observation using the microtome, as stated, the previously fixated tissue samples must be embedded in paraffin (optical microscopy), or certain plastic resins (optical and electronic microscopy), to provide them a more rigid complexion. The inclusion step is often preceded by a dehydration and clearing steps to supplant the water present in the tissues by alcohol and then, the latter by xylene (paraffin is soluble in xylene) (Junqueira and Carneiro 1987). An alternative approach for this method that replaces both described fixation and inclusion steps is the frozen fixation, further described in this section.
- **Staining -** Considering that one or more sections sliced from the tissue block may be placed on a single slide or several slides for comparison, they can be stained with a wide variety of chemical or immunologically based procedures. The staining methods selectively highlight several components in the tissues, cells and ECM. The prevalent staining technique is the haematoxylin and eosin method (H & E), capable of

highlighting most of the significant cellular structures in the tissues. This technique stains the cell nucleus and other acidic structures in blue or violet (haematoxylin) and in pink the cytoplasm and collagen (eosin). Other techniques enable the contrast of more specific tissue structures or organisms by recurring to histochemical reactions, and also, in the case of immunohistochemical stains, to assess the presence or absence of a certain protein. These methods are performed only when the H & E staining fails to accentuate the contrast of the studied structure in the tissue (Junqueira and Carneiro 1987, Randell, Ruddle et al. 2012). Representative images of the visual appearance under the microscope of the referred staining methods applied on cellular tissues are presented in Figure 7.

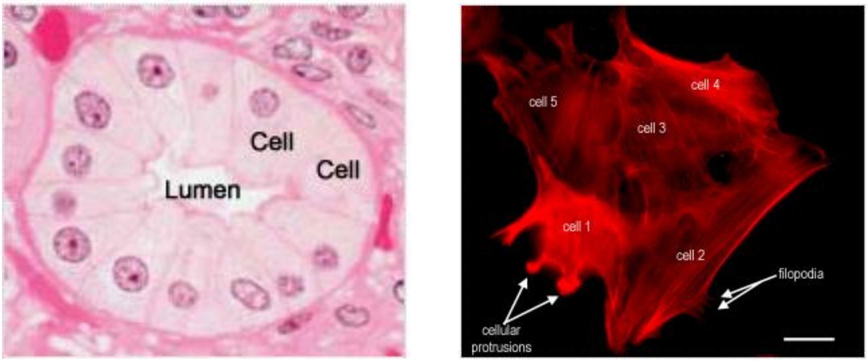

Figure 7. Histology picture of a set of cells lining a duct stained with H & E (on the left), and a histology image stained with immunohistochemical techniques to enhance, in red, the presence of the protein actin in the cells (on the right). Adapted from Leeds University Histology Guide (Michelle Peckham 2003).

In the frozen fixation, the tissues to be analysed are rapidly frozen (replacing the chemical fixation and inclusion steps in the previous protocol), and then stained with H & E technique. Despite producing lower quality slides this method acquires slices in a shorter time, ideal when is required a fast examination of the tissue (Randell, Ruddle et al. 2012).

2.1.3. Microscopy and Histological Sample Observation

After the preparation of histological samples (more details in section 2.1.2) the microscopic cellular structures present in them are observed under the microscope. In this section, the prevalent types of microscopy implemented to visualize and analyze those tissue slices as well as innovative methods to perform the observation and diagnostic of histological images are addressed. There are two major types of microscopy devices, the light or optical microscopes and the electronic microscopes. The most critical factor concerning a microscope is its resolution power or resolution limit, which is measured by the minimum distance between two particles in the image (Junqueira and Carneiro 1987, Randell, Ruddle et al. 2012). Functional and operational details concerning different microscopes of both groups are explained further.

The conventional **light** or **optical microscope** exhibits images of the stained tissues through illumination, which transverses the sample, generated by a light source. It is composed by both mechanical and optical parts and has a limit resolution of 0.2 µm. The optical part comprises three sets of lenses, namely the condenser, the objectives and ocular lenses. The first condenses the light from the source to the histological sample, the objectives collect the light that crossed the sample and projects an augmented version of the received image, ranging the magnification from 2.5x to 40x, into the ocular lens also contributing for the final magnification in a factor of 10. The final magnification is then, the product of both objective and ocular magnification. However, by convention the ocular magnification factor is not included in image descriptions. Besides the normal light microscope, optical microscopy also comprises other two major types of microscopes, the confocal and the fluorescence microscopes (Junqueira and Carneiro 1987, Randell, Ruddle et al. 2012).

Confocal microscopes allow the focusing of thinner sections in the image, avoiding the observation of overlapping planes of the tissue, fact that degrades and reduces the image's definition. In order to perform this specific focus, the light beam that crosses the histological sample is narrow and the tissue's image must transverse a small orifice. Consequently, this setup only allows the focussed plane of the original image to reach the detector, blocking all other consecutive planes. Since only a thin section is focussed at a time it is possible the three dimensional (3D) reconstruction by gathering all the planes of the analyzed tissue, through a computational algorithm (application later explored in the following sections) (Junqueira and Carneiro 1987).

In **fluorescence microscopy**, the analyzed samples are lighted by a mercury light source and, by recurring to certain filters the wave-length of the projected light can be regulated. Certain biological structures present in the tissue sample have affinity to fluorescent substances that when excited by the projected light they answer by emitting light in specific wave-length. Through the application of this technique certain biological components exhibit bright colors in the observed image, being highlighted from the surroundings (Junqueira and Carneiro 1987).

Electronic microscopy is based on the interaction between electrons and the tissues present in the sample to be analyzed. Considering that light microscopes have a limit resolution of 0.2 µm, electron microscopy represents a more accurate solution, offering a more detailed image of smaller components in the studied tissue with a limit resolution of approximately 3 nm. Nowadays, exist two types of electron microscopes, transmission and scanning electron microscopes (Junqueira and Carneiro 1987).

Transmission microscopes possess a resolving power of approximately 3 nm, thus allowing the detailed observation of isolated biomolecules or particles 400 thousand times magnified. For entire tissue samples, the magnifying power is reduced to 120 thousand times, still a high resolution when compared with the optical microscope. The operating mode of this microscope is based on the detour of electrons when in contact with magnetic fields analogous to lens' light reflection in the optical microscope. The electron beam is produced upon heating a tungsten cathode, and, due to a voltage potential between the latter and the anode, the electrons are accelerated and transverse in high speed the microscope tube. In the tube, the beam is condensed through an electromagnetic lens (coils) and interacts with the tissue sample, traversing it and being consecutively amplified by a sequence of magnifying lenses. In the end, the electrons reach a detector (fluorescence plate) and imprint a black and white image of the analyzed sample. The printed grayscale is done according to the amount of electrons that crossed the microscope's column and so, the tissue sample. Darker spots are electron-dense areas, meaning that more electrons traversed the tissue unaltered, not encountering any structure (Junqueira and Carneiro 1987).

Scanning microscopes acquire almost 3D images from the surface of tissues and cells in the analyzed sample. To perform this, the tissue is covered with a metallic coating, and a narrow electron beam is directed to the sample going through the entire surface of the tissue, without traversing it, in opposition to the transmission microscopes. The emitted electrons reflect on the surface and are collected by a detector, amplifying them and, with the intervention of other electronic components, a signal is produced in the form of a black and white image, similar to the transmission microscope.

The images produced by this electron microscopy equipment can be consulted in a monitor or stored (Junqueira and Carneiro 1987).

Examples of biological images collected from some of the previously referred types of microscopes are depicted in Figure 8.

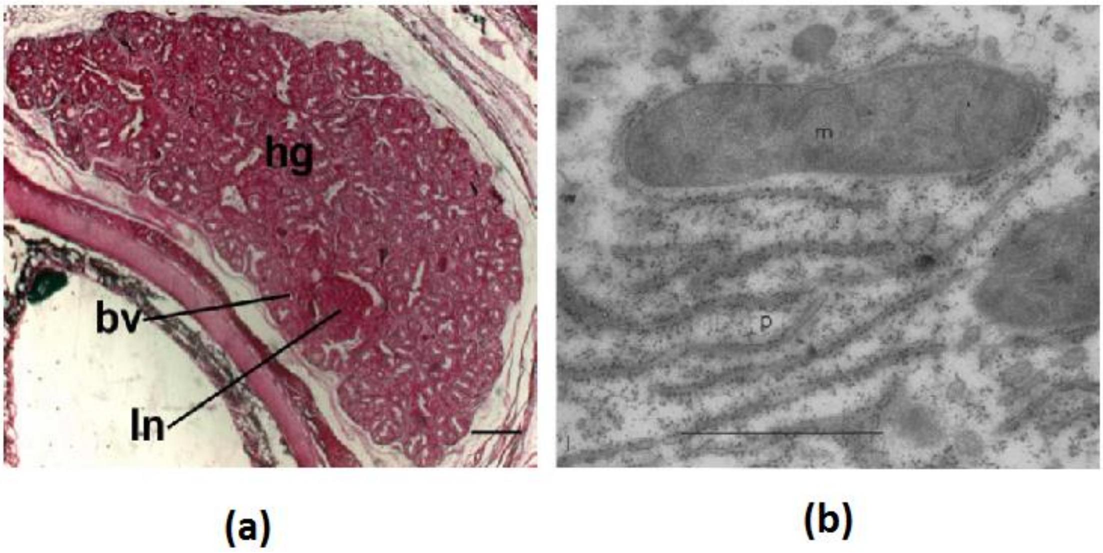

(a) (b)

Figure 8. Comparative images acquired from optical microscopy (a) and electron microscopy (b). Image (a) is a light micrograph of Harderian gland from a neonate *Alligator mississipiensis* stained with Methyl Green-Pyronin Y (bv-blood vessel; hg-Harderian gland and ln-lymphatic node). Adapted from (Rehorek and Smith 2007). Image (b) is a micrograph of a section of mouse liver stained in a saturated solution of uranyl acetate (m-mitochondria and p-highly dense RNA particles). Adapted from (Watson 1958).

Recent alternatives to the microscopic current approaches have been developed. In order to counter the extensive time dispensed in learning and accustoming to the microscope usage and considering the decrease in use of these devices in medical schools (Randell, Ruddle et al. 2013), these institutions have been using virtual slides (Histopathology slides scanned and stored as digital images), for teaching purposes. These slides allow a greater interaction between the students and the relevant morphological features present in the visualized tissue (Kumar, Velan et al. 2004).

In Leeds University, *Randell R.* and collaborators have developed a virtual reality microscope that consists of a wall-sized high-definition display (Powerwall) capable of rendering gigapixel virtual slides in real time (Figure 9). This system provides a five times greater slide area than conventional microscopes with equivalent magnification, and since it has a wall-size is better suited for group interpretation. This novel approach enables students to cooperatively interpret the displayed images, showing a more interactive apprenticeship. A complementary study, performed by *Treanor D.* and co-workers, aimed to verify this new solution for virtual slides analysis as a viable replacement for conventional microscopy in the histopathologists' investigation and diagnostic routine. In fact, the diagnostic made by consulting virtual slices takes 60% longer, mainly due to the considerable amount of time spent to navigate across the entire image in the small display size, provided by common computer monitors and inadequate user interfaces. With this in mind, the aim of this study was to assess if by increasing the display size, using the Powerwall, the diagnostic would reach similar speed when comparing to conventional microscopy. The performed test in this study involved a simple diagnosis, finding small objects in the image, a decision about a lymph node and score a tissue microarray. By using the virtual microscope, histopathologists performed clinical diagnostics and all the other assigned tasks in similar times as when using a conventional microscope (Treanor, Jordan-Owers et al. 2009, Randell, Hutchins et al. 2012, Randell, Ruddle et al. 2013).

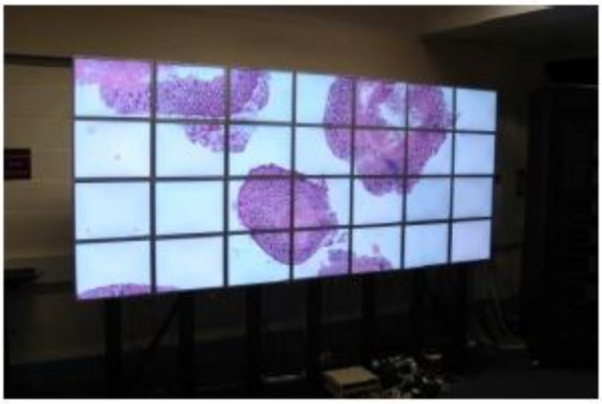

Figure 9. Leeds University wall-sized virtual microscope. Adapted from (Randell, Hutchins et al. 2012).

In the University of South Carolina School of Medicine, according to (Blake, Lavoie et al. 2003), the transition and implementation of virtual slides and virtual microscopes for teaching purposes was performed. The histological slides were scanned and viewed up to a 400x magnification recurring to the MrSID viewer (wavelet-based multiresolution seamless image database, property of LizardTech (Hovanes, Deal et al. 1999)) and the computer as a virtual microscope. The stated approach possesses useful features, including effective microscope and telescope functions providing greater versatility for tissue sample study and increased speed in localizing the structures of interest, when compared to the conventional microscope.

In light of the stated, digital pathology promises interesting advantages, both in terms of efficiency and safety considering conventional microscopy procedures (Randell, Ruddle et al. 2012). Potential advantages associated to a digital system reside in the possibility to alert histopathologists about the presence of new slides or cases to be analyzed (similar to the workflow in radiology diagnostics) and provide an easier cooperation between technicians when investigating a particular case. The latter is extremely important in the workflow of specialists, since this digital method allows a faster and safer way to share microscopic visualizations of tissue samples with other specialists, from other labs and also countries, to obtain second opinions, an extremely important procedure to ensure a flawless diagnostic. With the digital procedure, slides can be simultaneously sent to several histopathologists and, since the physical transportation of those slides is inexistent, there is a reduced risk of losing or mixing them, thus avoiding an erroneous diagnostic (Della Mea, Demichelis et al. 2006, Gilbertson, Ho et al. 2006, Nakhleh 2008). Also with the purpose of providing a fast and accurate second opinion to doctors and histopathologists, several computational methods are being developed to process and analyze digital tissue images. Some of those methods are introduced in following sections.

2.2. Image Processing

The first approach in order to acquire visual features and information from images, in the particular case of this study, from histological images, involves some computational strategies constituting the image processing procedure.

The beginnings of image processing trace back to the middle of the 20th century, when it started to be applied to improve microscope image's quality, basically through frequency filtering (signal-to-noise ratio, contrast and image restoration methods). Real developments were made since then, and the analog image processing was replaced by digital image processing with the advent of powerful computers capable of applying sophisticated algorithms to large images in an acceptable amount of time (Bonnet 2004).

Since the visual interpretation is the core of most medical diagnostic procedures and the final diagnostic decision, for cancer and other diseases, is based on tissue examination, medicine represents a large application field for image processing and analysis algorithms (Bengtsson 2003). However, visual interpretation and evaluation present several weaknesses. For pathologists, it is a time-consuming, cumbersome and tedious process to analyze a large number of tissue samples in practice, thus requiring a long time and intensive manual labor to produce viable results. Besides from this problem, visual evaluations can, in many cases, be subject to unacceptable inter and intra-reviewer discrepancies (20% discrepancy between central and institutional reviewers, as reported by *Teot L.A. et al.* in (Teot, Sposto et al. 2007)), due to the sampling bias, confirming that it represents an error-prone method (Bengtsson 2003, Kong, Sertel et al. 2009, Sertel, Kong et al. 2009).

To overcome the stated weaknesses, established in the currently used visual evaluation process, allied to the fact that digital images are growing in popularity, computational methods resorting to automated image processing and analysis algorithms are being developed (Bengtsson 2003, Kong, Sertel et al. 2009). The automatic processing and analysis of tissue images provides reliable data, accelerates data acquisition process and by allowing digital image management it can replace other evaluation methods, more expensive and impossible to execute (Cisneros, Cordero et al. 2011).

Automated systems can exclude human factor mistakes and increase the speed of diagnostic processes. These systems represent an important asset considering that the amount of experienced specialists that conduct a correct histological analysis is reduced or concentrated in big medical centers. Therefore, this leads to an accumulation of cases poorly or misdiagnosed, conducting to incorrect untimely treatments and ultimately resulting in disablement or death. Considering the abovementioned it is clear the need for automated processes concerning morphology diagnostics in medicine, to improve the diagnostic accuracy and compensate the scarce number of specialists (Nedzved, Belotserkovsky et al. 2005).

The key challenges in histological image computational analysis are automated cellular segmentation and classification in tissue images. Nevertheless, due to the complex nature and variety of histological images, it is difficult to develop automatic segmentation methods applicable to any type of those images (Nedzved, Belotserkovsky et al. 2005, Chomphuwiset, Magee et al. 2011).

The general procedure for automatic image processing and analysis can be divided in several steps, starting with the acquisition of digital histology images, which can range from diverse resolutions depending on the application and the size of the biological structure in study, on the histological sample. The following step is the image processing to identify the target tissues or biological structures in question, comprising, as a standard framework, image enhancement, image segmentation, feature extraction and implementation of machine learning algorithms (Caicedo 2009). To perform each of the previously referred stages a wide variety of computational methods can be implemented, according to different purposes (for example, automation of mass screening of histological specimens or quantitative analysis of a significant structure in the tissue) (Bengtsson 2003).

The image processing and analysis pipeline that is going to be produced in this work consists of three particular steps, the image pre-processing, image segmentation and 3D reconstruction (in section 2.3). A state of the art on methods for both these steps is presented in more detail in further sections.

2.2.1. Image Pre-Processing

Although segmentation is the most important step in image processing and analysis, it is unusual to achieve a consistent and useful segmentation using only a single procedure. In order to obtain a successful segmentation, algorithms typically apply a constructed combination of methods, including a wide variety of preprocessing steps (Beare and Lehmann 2006).

To process histological images, an initial preprocessing step must be applied to reduce the computational costs through multi-scale image decomposition (Gonzalez and Woods 2008). This initial process produces low resolution images that can be analyzed to locate interesting structures and allow the implementation of other image processing steps only on those structures' pixels. The preprocessing step is meant also to restore the images, by reducing image noise, low intensity contrast and intensity inhomogeneities present in the histological data. To perform this, methods such as image smoothing, denoise and enhancement can be applied (He, Long et al. 2010). Image smoothing is commonly performed recurring to spatial filtering methods used to remove image high frequency noise. Image denoising methods are implemented to remove image noise produced in image acquisition and compression processes (Aubert and Kornprobst 2006) and image enhancement techniques favour an increase in contrast between the regions of interest and the background, being the adaptive filters the most commonly employed methods (Gonzalez and Woods 2008).

Considering the amount of manual labor involved in tissue samples preparation (section 2.1.2), this process tends to introduce certain types of artifacts that require proper image preprocessing techniques to be countered. The majority of artifacts found in histological images are based on orientation differences found in the sections mounted in glass slides, variable luminance gradient (depending on the slide region where the tissue observed), non-tissue noise produced by dust or bubbles and staining variations (variable tissue thickness and stain concentrations originate color variations in the histological stained structures). Therefore, image pre-processing techniques are applied to deal with acquisition artifacts and defective histology sections (Mosaliganti, Pan et al. 2006).

Some techniques are specially designed to deal with histological artifacts present in the digital images, namely the defective section exclusion and principal component analysis (PCA) alignment.

In order to improve the 3D reconstruction robustness **defective sections** have to be identified and removed from the registration process. Since all images are acquired with the same magnification, tissue sizes in consecutive images should not suffer significant variations. Thus, when a large variation is verified it is probably due to broken or defective sections. To eliminate them the relevant structure areas were computed for each image and plotted against section location, using binary masks (masks containing information about the tissue pixel location. Tissue pixels identified and stored as binary masks). Spikes in this plot are potential defective sections (Mosaliganti, Pan et al. 2006).

Principal component analysis alignment is used to estimate tissue orientation, according to prior knowledge of typical structure arrangement, concerning the studied tissue. Since tissue orientations are used to initialize registration methods (section 2.3), by using this technique, the likelihood of converging to a more reliable global solution is increased (Mosaliganti, Pan et al. 2006).

The staining conditions verified in different histological slices suffer considerable variations (Figure 10). Therefore, after the being digitized, images present considerable color ranges. To normalize color distributions present across the slices, **histogram equalization** represents a viable solution (Sertel, Catalyurek et al. 2009). Histogram equalization is a well-known and widely used image enhancement technique, due to its simplicity, high performance in almost all types of images. This technique is performed by remapping of grey-levels in an image based on a probability distribution of the input grey-levels, stretching the dynamic range of the image histogram. Thus, resulting in overall image contrast enhancement. The drawbacks of this method are noticeable in images with high and low mean brightness. The result is a significant change in the image outlook, whereas the purpose was only to enhance the contrast. Histogram equalization is best suited to enhance the edges between different structures, but, in return, reduces local details within those structures, producing over enhancement and saturation artefacts (Kaur, Kaur et al. 2011). The histogram equalization procedure is based on the assumption that the processed image presents uniform image quality in all regions, and therefore, one single grayscale mapping provides similar contrast enhancement throughout all these regions. But, when distributions of grayscale intensities are variable according to different regions in the image, the previous assumption is invalid. Facing this, an adaptive histogram equalization technique, capable of determining the mapping for each pixel based on its local grayscale distribution (surrounding pixels), could significantly outperform the standard method. However, when grayscale distribution is highly localized, full histogram equalization might not be desirable to transform very low contrast images. By limiting the contrast allowed through histogram equalization, the possibility of two very close grayscales being mapped to significantly different grayscales, i.e. high slope segments present in the grayscale mapping curve, can be avoided. Combining the contrast limiting approach with the previously mentioned adaptive histogram equalization method, the result is referred to as **Contrast Limited Adaptive Histogram Equalization (CLAHE)** (Reza 2004).

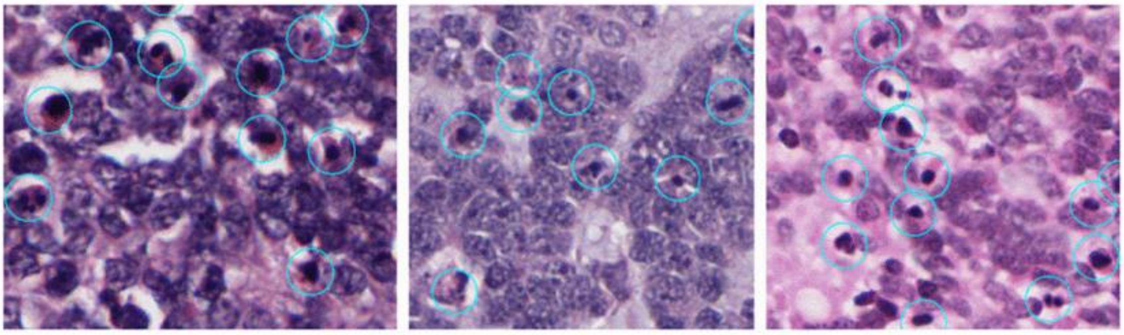

Figure 10. Sequence of histological images from MKI (Mitosis-karyorrhexis index) cells, varying in color information due to staining differences. Adapted from (Sertel, Catalyurek et al. 2009).

For medical images, **color enhancement** represents a valuable tool to aid in visualization, detection and segmentation of specific tissue structures. An effective approach to increase color contrast on an image and maintain its hue (the pure color) is to transform the RGB (R - Red, G - Green, B - Blue) color into HSV (Hue, Saturation, Value) color space, modifying only the saturation (luminance) value in the image's pixels. The transformation is given by:

$$H = cos^{-1} \times \left(\frac{\frac{1}{2}[(R-G)+(R-B)]}{\sqrt{(R-G)^2+(R-B)(G-B)}} \right) \tag{1}$$

$$S = 1 - \frac{3}{R+G+B}[\min(R, G, B)] \tag{2}$$

$$V = \frac{1}{3}(R + G + B) \tag{3}$$

The luminance manipulation, through grey-level enhancement processes, without affecting the other two components in HSV color is possible due to the lack of correlation between these components. The usual process starts by performing the color transform to convert the image in HSV color where the luminance or color saturation can be modified, disregarding the other components. Then, the reverse transform back to RGB color is applied in order to ascertain the effects of the produced modification (Bautista and Yagi 2010).

Hukkanen J. and co-.workers implemented a pre-processing method to improve the efficiency of nuclei segmentation (more information in section 2.2.2.) in histological images. The pre-processing method performs the conversion of H & E stained histological images originally in RGB color space into CIE L*a*b color space. The L component, the luminosity component, is then denoted as a grey-level image, which is further processed to obtain the segmentation. The L*a*b color space consists of a luminosity layer "L*", a chromaticity layer "a*" (indicating the color location in the red-green axis) and a chromaticity layer "b*" (indicating the color location in the blue-yellow axis)(Hukkanen, Hategan et al. 2010).

In (Tabesh, Teverovskiy et al. 2007) is presented a study concerning image features for cancer diagnosis and histological grading of prostate images. The features representing color, texture and morphological details were combined in a supervised learning framework. The first stage in this framework involved pre-processing techniques, including background removal and image histogram matching to a reference image. The background was identified and then removed from the analysis through color tissue image transformation, from RGB color space into YCbCr color space (Gonzalez and Woods 2008), and posterior thresholding (section 2.2.2.) of the luminance (Y) component with a global empirically determined threshold. After this, the binary mask containing the tissues of interest is refined via closing and opening operations to fill gaps between tissue structures and remove small artefacts from the image. A convex hull operation (Gonzalez and Woods 2008) is then, applied to ensure the integration of lumens as tissue of interest, avoiding its exclusion from the binary mask. The second pre-processing step, implemented in this study, consisted of an histogram matching between the analysed histological image and a reference image, through the transformation $F_r^{-1}[F_i(x)]$, where x is the pixel value in each of the red, blue and green channels. F_r and F_i are, the cumulative distribution function of pixel values for the input and reference images, respectively. Histogram matching is performed to mitigate color variations produced by staining and illumination conditions, which can affect segmentation efficiency.

The **Stain Deconvolution** technique is a pre-processing method, based on color deconvolution, which aims to deconvolve the applied stains on a certain RGB color image, to generate separate images, where each grayscale image shows the distribution of a single stain. This algorithm assumes that the chemical stains implemented to dye the tissue slides follows the Beer-Lambert Law of absorption, which provides a logarithmic relationship between the original RGB color channels and a stain matrix. This complex methodology is presented by both

(Ruifrok and Johnston 2001, Unpublished 2015), and the algorithm behind it is further explained in this work, on section 3.2.3.

2.2.2. Image Segmentation

After image enhancement produced by pre-processing methods, removing the noise and increasing the contrast between the structures of interest and the remainder tissue, a new step, called segmentation, can be performed.

Segmentation is the most important part in image processing and analysis, and consists of a grouping process, in which the group components share similarities concerning one or more features, ultimately identifying regions in the input image corresponding to distinct structures (Vernon 1991).

The segmentation is the first step to perform automatic analysis of histology images, apart from the image pre-processing, enabling the distinction of some particular biological tissue from the remainder components in the image. Staining techniques are performed in histology to facilitate human visual identification of the different components, for a specialist, but in order to implement other computational processes on those components the segmentation must be performed (Cisneros, Cordero et al. 2011). The application of this step is suited for a multitude of purposes, such as effective identification of tissues, image subdivision for portionwise processing or pattern modelling (Caicedo 2009).

Since a universal segmentation, valid and suitable for all the image applications, does not exist, a specialized method is required for each application(Cisneros, Cordero et al. 2011). There are two different approaches to perform image segmentation: Region based and boundary based methods (Vernon 1991).

Region based methods focus on reconstructing the various components of an image into two dimensional areas (regions), by implementing a similarity criterion from the pixels of each elemental area (Cisneros, Cordero et al. 2011). An example of these segmentation methods are Region-Growing techniques, that, starting from one or more points (seeds), initialized manually or automatically by heuristic methods, they are expanded to neighbour pixels that share a certain homogeneity criterion (Pham, Xu et al. 2000).

Boundary based segmentation concerns on the detection of boundary pixels of the structures present in the image, extracting them from the rest. The isolated boundary is then used not only to define the location but also the shape of the structure of interest. Boundary detection algorithms diverge on the amount of domain-dependent information incorporated when the connection of edges is performed. Therefore, the effectiveness of these methods is intimately dependent on the performance of edge detection algorithms (Vernon 1991). Segmentation performed with edge detection techniques implements minimum cost functions and certain filters, based on the gradient concept, to determine the borders of homogeneous sections of the image. Considering that usually these detectors do not provide closed elements, as previously mentioned, additional techniques must be applied to connect the edges. These techniques depend on thresholds to determine the existence of edges, which represents a problem considering that tissue images present highly variable contrast, brightness and detail on the structures (mainly due to type and quality of the performed stain) (Cisneros, Cordero et al. 2011). However, edge based algorithms are specially suitable for images with overlapped components (Díaz Iriberri 2007).

Since the tissue samples are stained to reveal specific structures, the majority of segmentation algorithms applied on histological images are based on color analysis and contrast, thus region based methods constitute the best approach for this task. Simple techniques based on thresholding (Chaudhuri, Rodenacker et al. 1988), which are applied on gray-scale representations of the processed image to separate pixels into two classes according to their intensity, and more complex ones such as the k-means clustering algorithm (Chaudhuri, Rodenacker et al. 1988, Sertel, Kong et al. 2009), similar to the threshold but applied to subdivide the image in more than two classes, can be implemented for this purpose (Caicedo 2009). Some other algorithms have been proposed to deal with tissue structure and color variation such as active contour and watershed based techniques (Chomphuwiset, Magee et al. 2011).

According to (Cisneros, Cordero et al. 2011) and its experience in histological image processing, thresholding techniques obtain accurate results in a reduced computing time, in contrast to other methods, including region growing and edge based techniques, that produced an incomplete and over-segmented image result, respectively. Therefore, the thresholding technique is thoroughly explained and presented below.

Gray level Thresholding is a simple region based technique used to highlight structures from the background that differ in gray-level intensity. The threshold operation will assign the value 255 (or 1 depending on the scale) to pixels with a grey-level above the threshold value and 0 (zero) to pixels with an intensity below that value, thus segmenting the image into two separate regions (structure and background).This operation consists in a test implementing the function T:

$$T(x, y, N(x, y), g(x, y)) \quad (4)$$

where $g(x, y)$ is the grey-level at the pixel (x, y) and $N(x, y)$ certain local property of the considered pixel. When $g(x, y)$ is greater than T, the pixel (x, y) is labelled as belonging to the structure, otherwise it is labelled as background (Vernon 1991). Three classes of thresholding can be distinguished based on the restrictions imposed to Equation (4), being local, global and dynamic thresholding (Weszka 1978). In the global approach the threshold test is based exclusively in the threshold value and grey-level of the considered point, neglecting its position and local context in the image. Local thresholding is dependent not only in the grey-level but also on a neighbourhood property of the point and, dynamic thresholding, is dependent on both previous properties and also on the point coordinates in the image. The choice of an adequate threshold for a given image is the major problem opposing to the acquisition of a valid and complete segmentation. To select the value that better differentiates the structure from the background several techniques can be applied, most of them based on the analysis of grey-level histograms. The use of these histograms often results in a difficult method to detect the threshold value, mainly due to image noise and inexistence of two evident modes in the intensities (bi-modal histogram) (Vernon 1991).

Considering that thresholding techniques examine the properties of each pixel in order to evaluate its color and so, the pixel's type according to certain measures. *Cisneros et al* proposed the measurement of the Mahalanobis distance (Mahalanobis 1936) (complementing the thresholding procedure) in order to distinguish and segment the type of the pixel between two components, i.e. by determining the distance between the pixel's color and the components' average color. This measure is subjective and has to be calibrated for each staining procedure. The proposed segmentation technique proved to be well-suited for analysis of histological image, particularly for tissue preparations with different dyes and structures presenting a considerable spatial separation (Cisneros, Cordero et al. 2011).

According to (Xu and Wunsch 2005) the **K-means** algorithm is the most acknowledged square error based clustering algorithm. This method performs partitional clustering, which consists in the assignment of a set of structures to be analysed into K clusters, without hierarchical structure. The K-means algorithm is a very straightforward method, easily implemented to solve many practical issues and it can perform clustering on large datasets. The first step is a random or prior knowledge based initialization of K cluster centres in image pixels (Calculation of a cluster prototype matrix). Then, each structure contained in the dataset is assigned to the nearest cluster and the prototype matrix is recalculated for the new partition, concerning the cluster's centroid. The previous steps are repeated until the cluster's centre stabilize in a constant position. There are some drawbacks for the implementation of this method concerning the lack of a universal, effective and automatic process to calculate the initial partitions, and the number of clusters present in a given image.

To perform tissue segmentation, or separation from the image background, clustering based algorithms (k-means) demonstrate better performance in face of luminance gradient presence, background noise and staining variability when compared to global thresholding methods, even when histogram equalization is implemented as pre-processing (section 2.2.1) (Mosaliganti, Pan et al. 2006). Figure 11 illustrates the parallel implementation of both methods to histological tissues.

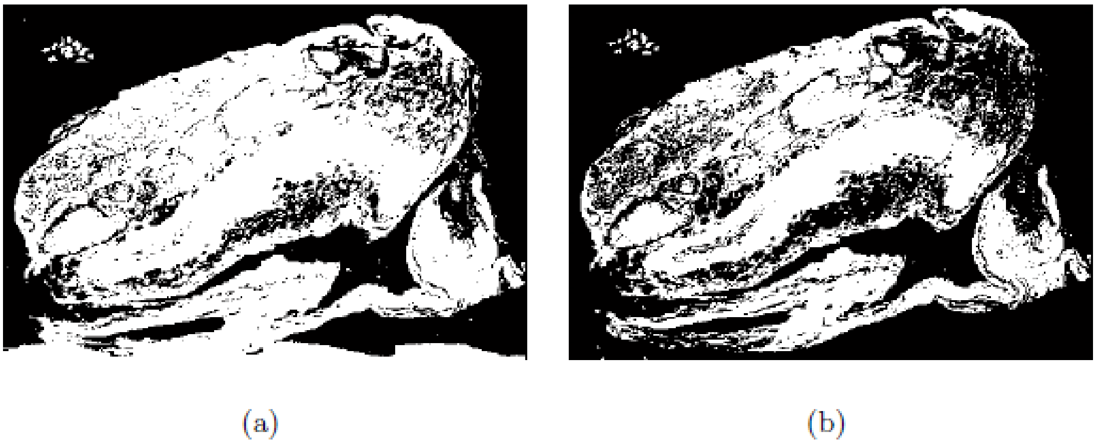
(a) (b)

Figure 11: Relevant tissue structure segmented using (a) the global thresholding approach and (b) k-means algorithm. Adapted from (Mosaliganti, Pan et al. 2006).

2.3. Image Registration and 3D Reconstruction

Since the microscope's invention there has been a huge development in the field of histology, alongside with the capability to acquire information from thin, two-dimensional cellular tissue sections and reconstruct the overall three-dimensional structure of studied tissue. The visualization of the spatial slice's relations in the three-dimensional form is an invaluable skill that is cultivated through a considerable amount of experience and observation (Koshi, Holla et al. 1997).

Hence, three-dimensional reconstruction of tissue samples at a microscopic resolution reveals significant potential to improve the study of disease processes when structural or spatial modifications are involved, and important to obtain the pathology diagnostic. Although the use of 3D imagery in histology seems unwarranted, since the latter is a 2D science (D. 1978), applications based on this process have been developed to investigate the anatomy and microarchitecture of healthy tissues (Kaufman, Brune et al. 1997), tumour proliferation and also to study gene expression, for example in developing mouse embryos (Han, van Hemert et al. 2011). The 3D reconstruction applications are used to study tissue slices both at a microscopic and macroscopic scale, allowing a more accurate definition of histological parameters (tumoral angiogenesis in oncology and cellular distortions in prion diseases) (at microscopic level), and the analysis of structures too small to be precisely dissected and too large to be studied in a 2D slice basis (at macroscopic level) (Ourselin, Roche et al. 2001). The combination of 3D image reconstruction methodologies with immunohistochemistry or in situ hybridisation techniques provides a better understanding on phenotypic and functional information concerning the cellular structures (Roberts, Magee et al. 2012).

Most of the existent 3D imagery techniques involve deconstruction (into 2D slices), alignment and posterior reconstruction of those images into a 3D model (D. 1978). The techniques employed to perform the reconstruction framework suffered a great evolution, since the deconstruction of the tissue in 2D slices through histological procedures, and the acquisition and alignment of histological sections, originally examined and prepared through observation and hand-drawn interpretations (Rehorek and Smith 2007). Since then, several less destructive and time consuming techniques have been employed to observe and analyze the tissues, such as the confocal microscopy (Kaczmarek and Strzelczyk 2005), magnetic resonance imaging (Perry, Cartamil et al. 2007) and computer tomography (Kley 2006). The preparation of micrographs and digitized images have improved the accuracy of measurements and extraction of numerous features in 3D reconstruction of cellular images, substituting the biological artist and hand-drawn representations (Shea 1979, Rehorek and Smith 2007).

All the previously referred non-destructing imaging methodologies (MRI and CT) enable the analysis of cellular tissues in three dimensions. Despite consisting of mature technologies, currently accepted and used in clinical and research practice, through the implementation of computational reconstructions for conventional histopathology, it is allowed the use of well-known and gold standard histological staining and interpretation techniques (Roberts, Magee et al. 2012).

The reconstruction of 3D tissue volume from 2D histological slices requires a precise acquisition of serial histological data combined with robust automated techniques of image processing and analysis to be applied on digitized versions of those tissue slides. A usual histological reconstruction requires first, a slice-to-blockface (photograph of the volume prior of the histological slice's acquisition, serving as reference. An example is illustrated in Figure 12) registration for the purpose of minimizing the structural inhomogeneities found in the slices, followed by a slice-to slice registration to reduce the inhomogeneities between slices. A third step, consisting of a warping of reconstructed volume to a global reference can be performed, when the purpose is to study histological features combined with other 3D imaging techniques (for example, MRI) (Chakravarty, Bedell et al. 2008).

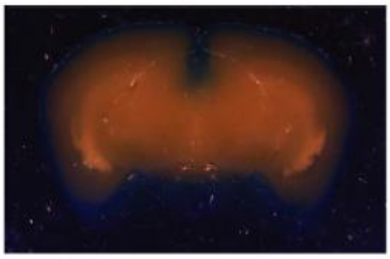

Figure 12. Image from an example of blockface used for 3D reconstruction. Adapted from (Chakravarty, Bedell et al. 2008).

Image registration is considered an optimization process that aligns two or more images aiming to find the image transform that is responsible for the best alignment or closest similarity of structures of interest between consecutive images or, in the case of this study, between consecutive histological tissue slices (Mosaliganti, Pan et al. 2006, Oliveira and Tavares 2014).

Registration algorithms are implemented to define correspondences between sets of images based on various image characteristics, ranging from specific landmark locations (Bookstein 1980), to contours or surfaces (Pelizzari, Chen et al. 1989, Davatzikos, Prince et al. 1996), and volumetric functions (Thirion 1998) applied to voxel intensities (Johnson and Christensen 2002).

Most medical image registration algorithms assume a ‘rigid body’ transformation, in which six degrees of freedom are comprise in the transformation, three translations and three rotations, being all the distances preserved (characteristic of a rigid transformation). Other registration methods consider an increased number of degrees of freedom, allowing in some cases anisotropic scaling (nine degrees) and skews (twelve degrees of freedom). When a transformation includes scaling, skews and also rigid body parameters is referred to as affine transformation. The implementation of an affine transformation rather than a rigid transform does not greatly increase the applicability of image registration, since the number of organs that only stretch or shear is limited (Hill, Batchelor et al. 2001). There are two major types of transformations in image registration methods: Linear transformations (described above) and elastic or non-rigid transformations. These non-rigid transformations are capable of locally warping the moving image to be aligned with the fixed, or reference image, through large deformation models, radial basis functions and continuum models (Goshtasby 2005).

The majority of Feature-based techniques consist on four steps: Feature detection is the manual or automatic detection of distinctive objects, such as closed-boundary regions, edges or contours, and their representation with control points. In the feature matching step, the correspondence between detected features in the fixed (static image) and moving image are established, recurring to diverse similarity measures. Transform model estimation consists in the alignment of both fixed and moving image, according to mapping functions estimation (transformation types). In image resampling and transformation, the last step, the moving image is transformed through the mapping function (Zitova and Flusser 2003).

A review on the currently implemented techniques to perform histological sample analysis and 3D image reconstruction is presented below.

In a study performed by (Braumann, Kuska et al. 2005) the three-dimensional structure of tumor invasion fronts of uterine cervix carcinoma was analyzed to better understand its intricate architectural-functional relation. The intention of the produced investigation was to obtain an objective quantification of the tumorous invasion based on 3D reconstructed tumoral tissue data, since the morphological information can be assessed through histological observation. The image computational algorithm presented comprised three registration steps, first a rigid one followed by a polynomial nonlinear method and finally a nonlinear curvature based one, and it was capable of reconstructing selected tumor invasion fronts from a considerable extend of histological serial sections (90-500 slices). Through this technique it was achieved an extremely detailed 3D reconstruction of invasion of solid tumors, as visualized in Figure 13.

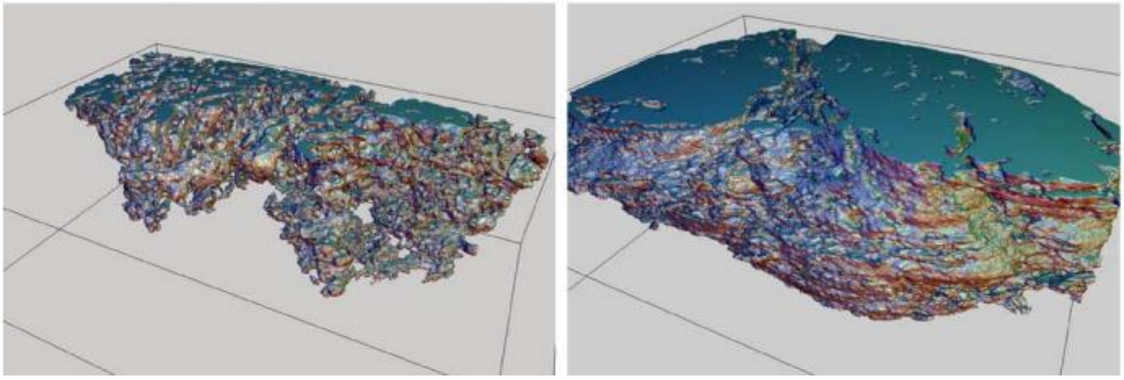

Figure 13. Two views of 3D reconstruction of uterine cervix carcinoma tumor invasion fronts, from different histological specimens. Adapted from (Braumann, Kuska et al. 2005).

An extension of the previous study was carried out by *Ryk J.* and co-workers, where the Large Image Microscope Array (LIMA), a vibratome capable of sectioning tissues to 40 mm thickness slices, is used to section entire organs, particularly lungs, into slice images in order to establish direct correlation between lung pathology and Computer Tomography (CT) images. A camera and a stereomicroscope mounted on the vibratome scan the entire surface area of the tissue, controlled by a custom software, responsible for the entire process automation. The alignment is accomplished through the combination of a custom code and the Insight Segmentation and Registration Toolkit (ITK), resulting in the registration of high magnification and resolution pathology images with the corresponding CT images (de Ryk, Namati et al. 2004).

Another technique developed by (Rehorek and Smith 2007) aims for the generation of 3D images from specific microanatomical structures contained in tissue sections. The presented 3D reconstruction technique not only allows the concurrent visualization of multiple structures or tissues but also enables the analysis of spatial topography from the histological sections. This technique involves, foremost, the visual identification and manual delimitation of the region of interest's position in a 2D section digital image. All the marked digital images were then aligned to previous slices based on fiducial landmarks (reference structures in the image), accomplished by rendering the second of two adjacent tissue sections through manual rotation of the image on top of the other slice.

A semiautomatic method was developed by (Kurien, Boyce et al. 2005) to produce three-dimensional reconstructions of invasive breast carcinoma, recurring to common laboratory equipment to evaluate the spatial arrangement of parenchymal cells. The tumour studied in this work was stained immunohistochemically to reconstruct two 3D images, one for normal parenchymal cells and the other for malignant. The digital histological sections were acquired using a microscope, a scanner and a camera connected to a computer, and the alignment was performed using a semiautomatic method, allowing manual interaction through a graphical interface. The referred method uses cross correlation coefficient as an integrity slice fit measure and an automatic process based on the Fibonacci search algorithm (Ramaprabha, Balaji et al. 2012) to achieve an automatic alignment. Finally, the resultant reconstructed volume was obtained using maximum, minimum point projection and back to front opacity blending. The results obtained through this method were distinct and accurate 3D reconstructed models, contributing to a more comprehensive and explicit visualization (high resolution) of spatial arrangement of normal and malignant parenchymal tissues and their relation to the surrounding tissues (Figure 14). This approach provided an insight on invasive breast carcinoma proliferation, unobtainable through conventional visualization of 2D histological sections.

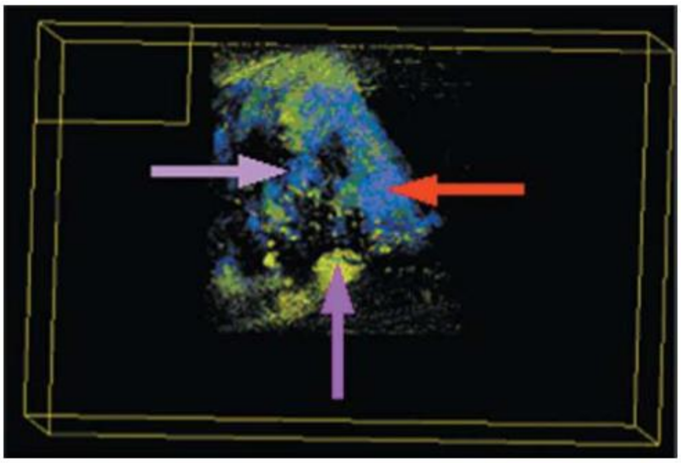

Figure 14. 3D reconstruction of invasive breast carcinoma immunohistochemically stained, illustrating the spatial arrangement of the different parenchymal tissues. Adapted from (Kurien, Boyce et al. 2005).

In (Ourselin, Roche et al. 2001) it is emphasized the need of a robust method to perform the alignment of histological sections for 3D reconstruction. In this work, it is proposed an intensity-based method to register the image slices, first by using a block matching strategy (Jain 1981), allowing the computation of local displacements between image slices, and then, a rigid transformation, estimated by those local measures. The entire process is fully automated and integrated into a multi-scale framework in order to improve accuracy and computation times. The results obtained experimentally highlight the capacity of the proposed algorithm to reach sub-pixel accuracy while being able to compensate large displacements between slices.

Conventional 3D histopathology is limited by low resolution, time and difficulty with acquiring a large number of images with a microscope, the absence of a fully integrated system for 3D reconstruction (Namati, De Ryk et al. 2007) and, in the case of manually guided 3D reconstruction, the time required for the whole process (Petrie, Flynn et al. 2002). Concerning those limitations, *Roberts N.* and collaborators developed a 3D histopathology software using automated virtual slide scanners to produce high-resolution digital images and 3D reconstructions of the cellular tissue. The software is applicable to any type of tissue, requires minimal manual intervention, once the slides are prepared, and reveals reasonably robustness over a wide variety of data or type of application. The system digitises automatically the virtual slides, which subsequently communicates with the image serving software to align the image and produce the visualization. To perform the alignment it uses a high-resolution registration followed by a multi-level registration method, whereby the user is able to manually select, zoom and re-register the area of interest (Roberts, Magee et al. 2012). The registration algorithm proposed by the author starts by performing a sequential slice-to-slice image based registration, a multi-stage method based on extension of phase correlation (De Castro and Morandi 1987), which consists of a first rigid alignment ignoring scale that serves as input to a non-rigid registration method that divides the input image into equally spaced square patches, individually aligned through the phase correlation. A non-rigid B-spline based transform is estimated through a least squares error minimising method and applied to the whole image to approximate a set of points from each patch. The B-spline is applied at multiple increasing resolutions and B-spline grid sizes. This registration method uses as reference a representative central virtual slide (generally the slice containing the largest portion of the tissue to be studied). The subsequent images are aligned to their neighbours and then concatenated to form a 3D volumetric dataset for the user to visualize, after the completion of rigid and non-rigid transforms. As previously referred in this study, it was also developed a user-interface to promote the interaction and user selection of sub-areas of interest in the image to re-register at higher resolution. This was performed using the explained non-rigid multiple-level resolution method, providing this way sub-cellular accuracy reconstructions. After the 3D volume reconstruction the developed software enables interactive segmentation of the volumetric structures by implementing several techniques, including a manual method called “color example thresholding” in which the user defines a threshold and selects a certain color in the image and the software annotates all the pixels sharing RGB color with the selected one and the considered threshold. Another approach implements region growing algorithms (Efford 2000) to segment spatially connected similar pixels (more information on section 2.2.2), using the user selected points as seeds and the threshold as color similarity criteria. In the end, it was implemented an iso-surfacing using marching cubes (Lorensen and Cline 1987) and mesh decimation (code from VTK (Schroeder, Martin et al. 2003)) to render the segmented volume and allow the visualization of distinct parts of the volume separately (Magee, Treanor et al. 2008, Roberts, Magee et al. 2012).

In (Chakravarty, Bedell et al. 2008) is described a method for 3D reconstruction of two dimensional histological sections from mouse brain to create volumetric data, a fundamental step in the analysis of ex-vivo data to validate in-vivo imaging techniques. To achieve the latter, the reconstructed volume is directly mapped into in-vivo anatomical MRI volumes, thus enabling accurate validation of recent imaging technologies, as well as the integration of histological cellular or molecular data in in-vivo structural and functional data. The procedure described in this work is an extension of a previous study by *Chakravarty et al.* (Chakravarty, Bertrand et al. 2006) performed for the reconstruction of human basal ganglia and thalamus, where the histological sections suffered first manual alignment and color adjustment, and then non-linear correction techniques to enhance the image alignment. In (Chakravarty, Bedell et al. 2008) it was used a digital blockface to perform image registration and a volume derived from the average of ten MRI volumes of mice (Lau, Lerch et al. 2008) to serve as volumetric reference. The method stated by the author starts with the alignment of histological sections to the corresponding blockface image. First, a slice-to-slice alignment of the blockface data was executed and a transformation mapping each slice to the next, converging this process to the center slice (reference), was estimated. Then, for the histological dataset it was applied and estimated a linear transformation to map all the slices into the corresponding slice in the blockface reconstructed volume. Both two dimensional transformations were adapted from the linear registration technique proposed in (Collins, Neelin et al. 1994). Posteriorly a nonlinear morphological correction was implemented, consisting of a slice-to-slice warping to correct morphological inconsistencies between slices. To perform the estimation of these transformations the ANIMAL algorithm (an iterative algorithm that estimates a 3D deformation field on a lattice of nodes when a source volume is matched to a target volume) was used (Collins and Evans 1997). Then, in order to counter intensity inhomogeneities between registered slices, possibly produced by staining densities and slice thickness irregularities that can challenge the correct visualization of the images, a nonlinear intensity correction was performed. This procedure first applies the nonlinear transformations estimated in the morphological correction to consecutive series of four slices, to grant that all of them present morphological consistency. After this, each slice was portioned into equally sized square patches, assuming that sufficiently small areas would enable the estimation of a first order polynomial scaling factor to match the joint histograms of each square by using a least-trimmed squares polynomial estimation (Prima, Ayache et al. 2001). Once performed this process for each square patch, a grid containing the scaling factors previously estimated was interpolated to match the resolution of the histological image, and then, the produced interpolation field was multiplied by all the slices to enhance the grey-level consistency. Finally, the histological reconstructed volume was directly warped to the stated MRI template volume reference. The results obtained through this routine demonstrate an effective alignment of the histological volume with the MRI template. These results enhance the fact that the combination of tissue preparation techniques and automated image processing allows for a more comprehensive, multi-modal evaluation of pathology or therapeutic intervention effectiveness in rodent models of CNS disease. The results obtained through the stated technique are presented in Figure 15 (Chakravarty, Bedell et al. 2008).

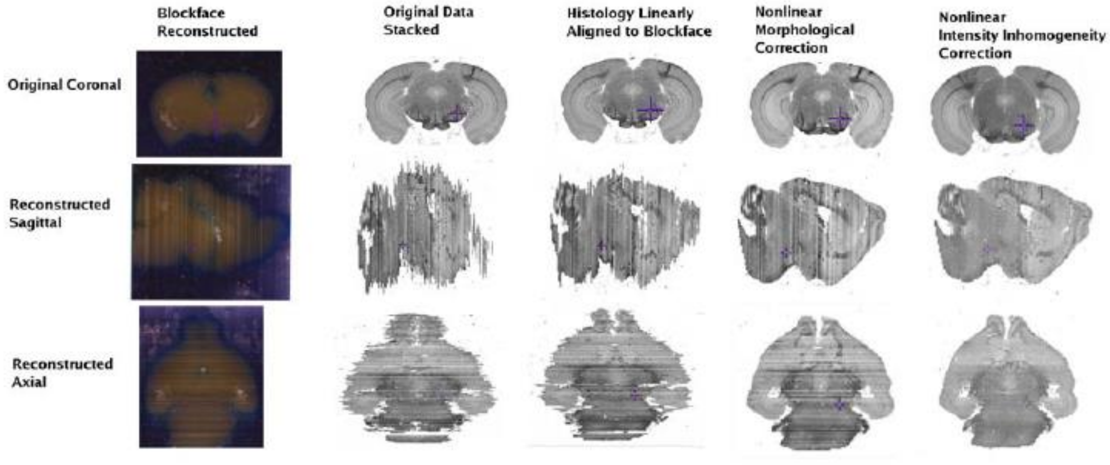

Figure 15. Volumetric results from the reconstruction of serial histological slices acquired by *Chakravarty M.* and collaborators. From left to the right: Blockface reconstructed, original data stacked without any correction, reconstruction model after slice-to-blockface linear alignment, resulting reconstruction from nonlinear morphological correction and reconstruction after nonlinear intensity correction. Adapted from (Chakravarty, Bedell et al. 2008).

Johnson J. and co-workers presented a hybrid landmark/intensity-based deformable registration algorithm. This algorithm applies an iterative process by producing accurate correspondences between image structures near landmark locations and elements separate from them by matching corresponding landmarks and image intensities, respectively. First are registered landmarks disregarding intensity and then intensity differences between slices are minimized (Johnson and Christensen 2002). Despite the accurate results, this technique was not applied to reconstruct 3D images from 2D slices and also revealed that when applied to unclassified data based on landmarks does not lead to reliable registrations.

Another method for automatic registration of histology sections was presented by *Arganda C.* and collaborators, consisting in a technique for non-deformable registration recurring to Sobel transforms and segmented contours. The goal of this project was to accurately align tissue sections in volumetric data and also to detect and render relevant structures in 3D. The algorithm proposed accomplished this by finding the best suited rigid body transformation (translation and rotation) of the images being registered (applied globally), through maximization of a matching function based on image correlation (applied locally on specific locations revealed by segmentation methods). A multiresolution pyramidal approach was then implemented, reaching the best registration transformation in increasing resolution stages (Arganda-Carreras, Fernandez-Gonzalez et al. 2004).

In (Mosaliganti, Pan et al. 2006) was presented a mutual information based registration approach, having as basis the maximization of mutual information (MI) (Maes, Collignon et al. 1997), an effective similarity measure to register multi-modal images when the image intensities are not linearly correlated. The proposed technique includes four stages, including the transform, metric, optimizer and interpolator phase, in order to register a consecutive slice into a stationary image. The transform stage is modelled, as previously referred approaches, to a rigid 2D transform, which allows rotation and translation. To perform the optimizer and interpolation stage were incorporated a regular step gradient optimizer (Maes, Vandermeulen et al. 1999) and a bi-linear interpolation (Maes, Collignon et al. 1997), respectively. The registration was acquired through MI optimization multiresolution strategies, as proved in previous studies that can provide similar robustness to direct registration combined with an increased computational speed when compared to other multiresolution techniques (Studholme, Hill et al. 1996, Maes, Vandermeulen et al. 1999). This approach was performed applying 3-level image pyramids (Figure 16), with image magnifications of 10x, 20x and 50x. Starting with the transform obtained for the lower magnification images are scaled and employed to initialize the next higher magnification, repeating this process until the highest resolution (the improvement in accuracy for resolutions above 50x do not compensate the computational costs). After this, a two-level optimization (Figure 17) was executed to achieve a higher MI in the reconstructed model. This process introduces a restricted translation and rotation around the PCA initialization (described in 2.2.1), altering the converged solutions. This step is repeated until no improvement is verified in the mutual information model. The presented study developed a multi-resolution MI based registration algorithm combined with a novel optimization strategy that allows not only a reduction of manual intervention in the registration process but also a higher chance of obtaining a converged global solution (Mosaliganti, Pan et al. 2006).

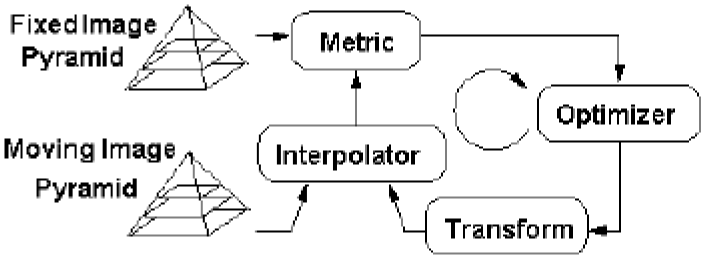

Figure 16. Schematic representation of the ITK-based registration framework. The transforms pass from a lower to a higher resolution based on the 3-level image pyramids shown. Adapted from (Mosaliganti, Pan et al. 2006).

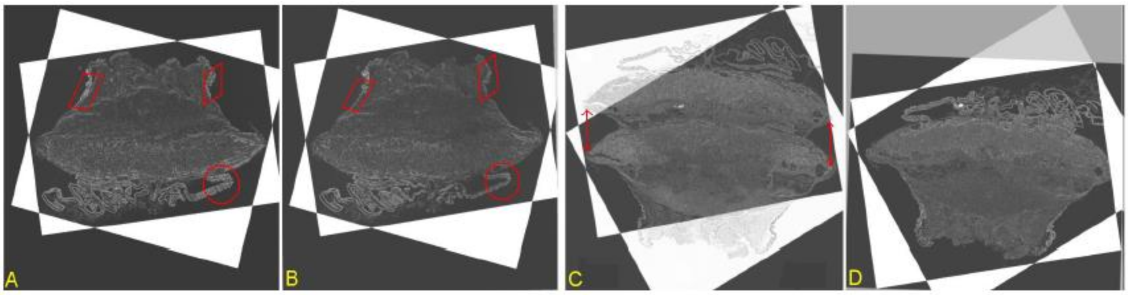

Figure 17. Representation of the regular step gradient descent (A,C) and the two-level optimizer (B,D) on 2 slides from placenta image dataset (PCA was applied initially as pre-processing), used in (Mosaliganti, Pan et al. 2006).

2.4. Key Issues

The present section summarizes the contents addressed in the literature review, highlighting the fundamental concepts to be retained.

- Histological techniques are considered the gold standard for assessing the natural response of a cellular tissue in face of a pathology or therapeutic intervention.

- The existent fundamental types of tissue are epithelial (covers body surfaces), connective (provides support and connection to all other tissues in the body), muscular (designed for contraction) and nervous (ensures the communication between sensorial cells, CNS and muscles).

- In order to visualize histological samples and their tissue structures under the microscope, a previous preparation of the tissue comprising fixation, inclusion and staining techniques must be performed.

- Digital histological slices provide numerous advantages when compared to conventional microscopy, namely in the possibility to alert histopathologists about the presence of new slides for analysis and provide easier cooperation between technicians when investigating a particular case (i.e. a second opinion).

- Automated computational systems, comprising segmentation and 3D reconstruction algorithms can providing a fast and accurate second opinion to doctors and histopathologists.

- Computational systems can also reduce the workload of histopathologists, who perform a rather time consuming and laborious task, subjected to high inter and intra-reader variability.

- Image pre-processing methods are applied to the histological images to reduce the visual noise and enhance the contrast between the interest structures and the remainder tissue.

- Segmentation is the most relevant process in image processing and analysis systems, enabling the distinction and identification of some particular biological tissue from the remainder components in the input image.

- Three-dimensional reconstruction of tissue samples at a microscopic resolution reveals significant potential to improve the study of disease processes when structural or spatial modifications are involved.

- Image registration is considered an optimization process that aligns two or more images, aiming to find the image transform responsible for the best alignment or closest similarity of structures of interest between consecutive images.

Chapter 3

Methodology

In this chapter, the methodology developed and all the algorithms constituting it will be thoroughly explored, as well as all the image datasets containing animal cell tissue, tested to provide the necessary validation for the proposed framework.

Firstly, the experimental database analyzed in this study, cordially supplied by the Pathology Laboratory of the Institute of Biomedical Sciences Abel Salazar, is going to be addressed, including the description of all three different tissue datasets, the properties of the digital image acquisition device and the relevant tissue regions to be processed and highlighted by the proposed methodology.

The second section of the methodology presents an exhaustive description and explanation of all the computational methods developed and employed to perform image processing and registration on the dataset, culminating with the final framework implemented integrating the most suited pre-processing, segmentation, registration and 3D reconstruction of the cell tissues. The presented computational framework was implemented in Matlab R2014a® (Inc., Natick, Massachusetts, United States).

3.1. Dataset

The three image datasets studied in this project were acquired and prepared, using the standard method detailed in section 2.1.2., in the Pathology laboratory in Institute of Biomedical Sciences Abel Salazar. In order to obtain the digital images an Olympus scanner program was used, creating an image for each slice in the three studied cases, described further in this section. Some features found in images from the datasets that can undermine the image processing and analysis proposed by the algorithm develop in this work, are also addressed in the present section.

3.1.1. Tissue Sample Preparation and Digital Image Acquisition

After selected the tissue to be studied, the histological sample preparation for observation and posterior digitalization was performed according to the methodology described in section 2.1.2. Three samples were prepared and stained for H & E to produce three different datasets. The initial case was marked with four dots around the tissue to improve image registration, an additional process not performed in the other two tissue samples, both produced following a normal protocol. Prior to scanning, a final cleaning process was conducted to remove agent residues from staining and superficial dust from single slides as well as corrections in coverslip displacements over the tissue surface. These precautions were taken into account due to the scanner high sensitivity in image acquisition and subsequent digital image overall quality.

Olympus VS110 - Digital virtual microscopy system (Olympus America Inc.) was the scanner used to obtain the digital images. This system is based on an upright motorized Olympus microscope with four optical lens (2x, 10x, 20x and 40x) that enables automatic tissue detection. The embedded software provides a full control to the user over the scanning process and is capable of scanning large specimens in multiple z-planes with high resolution [ref do scanner]. All the images included in the analyzed datasets were scanned at a 0.32µ/pixel resolution, or at 20x magnification (standard scanning magnification).

3.1.2. Tissue Analysis and Image Datasets

All the three cases analyzed in this study were obtained from domestic dog, *Canis lupus familiaris*, histological sections. The tissue sections composing the scanned image datasets were diagnosed by a histopathologist from Institute of Biomedical Sciences Abel Salazar, in order to establish the most relevant structures to be highlighted in the image processing framework. A brief description of the three studied cases is presented in Table I.

Table I. Characterization of the three image datasets studied in this work.

	Nº of Images	**Description**
Case 1	124	Testicular neoplasic tissue **Animal:** Dog
Case 2	100	Lymph node with possible metastasis **Animal:** Dog
Case 3	100	Lymph node with neoplasia **Animal:** Dog

Case 1 corresponds to a testicular tissue section, constituted by 124 images, in which it can be observed a neoplasic region in contact with representative structures of this reproductive organ. The presence of Leydig and Sertoli abnormal cells was detected through microscopic observation, supporting the existence of a collision tumor (two different cell lines), identified in Figure 18.

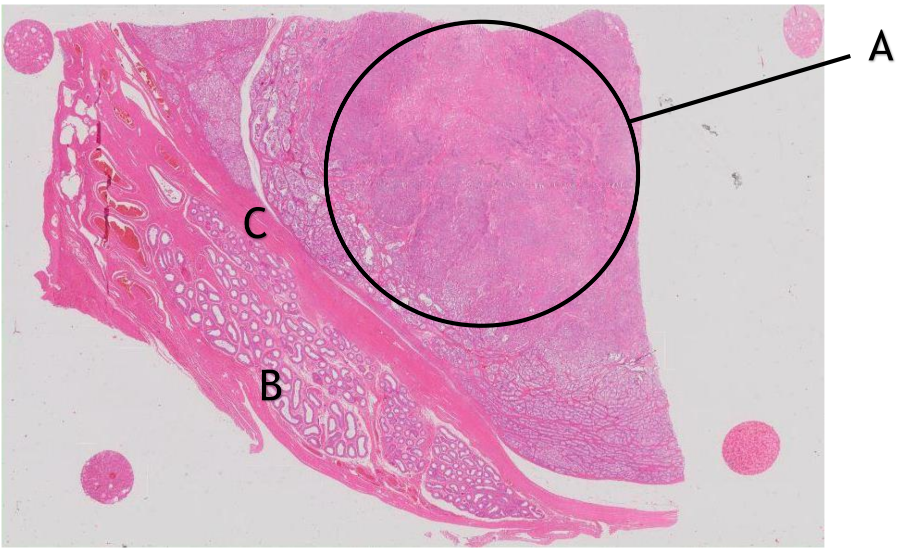

Figure 18. Image from Case 1 (Slice nº 51) – Testicular tissue section with a collision tumor (A). Epididymis is (B) and Connective tissue (C).

In case 2, the prepared tissue is a lymph gland or node, small oval structures dispersed through the body and intersected by lymphatic vessels. These organs play a fundamental role in the proper functioning of the immune system, since they filter the lymph that passes through them on its way to the blood (Gray and Carter 2008). The dataset for the second case contains 100 slices, and the lymph node depicted in it contains a possible metastasis, neoplastic cells that migrated from other regions of the body in the bloodstream or lymph system (in this case), traversing the vessel's walls (Klein 2008), highlighted in Figure 19.

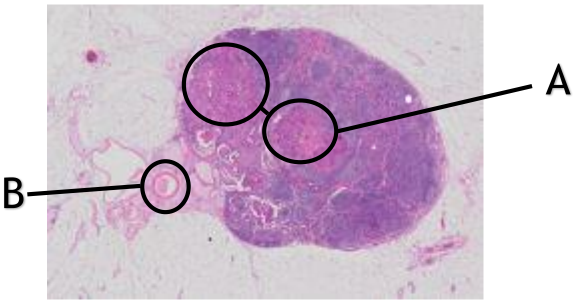

Figure 19. Image from Case 2 (Slice nº 5) – Lymph node tissue section with a possible neoplasic region (A). A blood vessel is marked by (B).

The last case studied, case 3, also represents a lymph node with metastasis and comprises a dataset with 100 images. The relevant tissues to be further analyzed in this study are exposed in Figure 20.

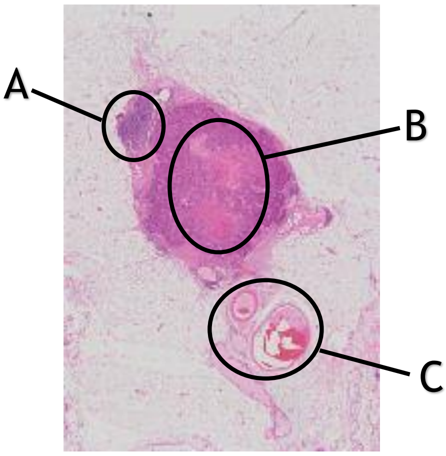

Figure 20. Image from Case 3 (Slice nº 33) – Lymph node tissue section with neoplasic regions (A) and (B). Blood vessels are marked by (C).

After observing all the images contained in each dataset it was clear that the manual method employed to prepare the histological samples introduced some artifacts, that corrupted the final digital image, and so, the tissues to be computationally processed. During the cutting and mounting stages some tissue sections were torn and folded resulting in the emergence of line artifacts, as shown in Figure 21. Also, the positioning of the section in different orientations and or locations in the glass slides, resultant of the manual nature of the process, can produce images with different luminance gradient. The presence of dust and air bubbles in the prepared slices also contributes to a poor image processing performance. In addition to these artifacts, differences in staining concentration between slides, and therefore in the final stain color in cell tissues can lead to inaccurate results, when processed by the algorithm (Mosaliganti, Pan et al. 2006). With this in mind, all the three cases were reviewed, and the severely damaged images with these types of artifacts were removed from the datasets. In case 2, six slices were removed leaving the dataset with 94 images in total. On the other two cases no images have been discarded.

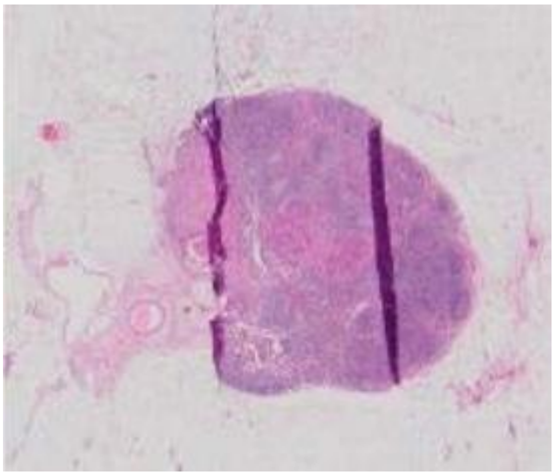

Figure 21. Image removed from case 2, due to presence of folds on the tissue section, produced in the mounting process.

3.2. Workflow implementation

Three different approaches were developed in this study to obtain the final 3D volume of the relevant cellular structures. The first methodology was developed just to ascertain the most suited pre-processing technique to obtain a high contrast between different stained tissues, thus providing the most accurate segmentation using kmeans, a simple, well-known and fast algorithm (Section 2.2.2.). After this, a more complete workflow was created, taking advantage of the previously determined pre-processing model and adapting it to a registration framework. The combination Pre-processing and registration method was analyzed, to obtain the best slice alignment. The final methodology was then established according to the previously referred studies to obtain the 3D volume and to ensure a more relevant segmentation of the stained structures.

3.2.1. First Approach – Based on pre-processing and Segmentation

Considering the first approach, several pre-processing methods were tested, on the previously referred datasets (section 3.1), to enhance the contrast in image intensities between different types of cell tissue. These processes include color space conversion and manipulation, histogram equalization methods and image intensity normalization.

The first process implemented was an **image normalization** technique, whose framework was designed for this study in order to distinguish the relevant structures, contained in the datasets, from the background. This method consists, first, of a color channel separation in red, green and blue images (grayscale images) from the original RGB image, followed by an average and standard deviation measurement of pixel intensities on each color image. The normalized image for each color channel is calculated through equation (5):

$$Norm = {(I - \mu I)}/{\sigma I} \qquad (5)$$

where $Norm$ is the resultant normalized image, I is the initial image, μI the average pixel intensity and σI the standard deviation value (both measured previously for each image). The final step of this method is the concatenation of the three normalized color channels to produce the RGB normalized final image. This is a standard score image normalization, to obtain high-contrast images, highlighting the entire relevant structure over the background, i.e. the colored sections of the image are highlighted.

The **color space transformations** were focussed during the development of the pre-processing step, and several of those spaces were tested, including CIE L*a*b (or L*a*b), HSV and YCbCr color space (Section 2.2.1.). All these conversions allow the enhancement and manipulation of several properties in the RGB image, like the color saturation, impossible to access in the original Red, Green and Blue channels.

In the first color space transformation, **CIE L*a*b**, the Red, Green and Blue channels composing the RGB image are converted into Luminosity (L), component a (red-green axis) and component b (blue – yellow axis), using (MathWorks) and (MathWorks). To perform the enhancement or diminution in the influence of these channels independently, a technique was conceived to convert RGB images to L*a*b color space. In this color space, the luminance channel and all the color component grayscale images (from the two last channels – a and b) are multiplied with a constant factor separately, and then, subjected to a histogram equalization (more precisely CLAHE – contrast limited adaptive histogram equalization, described with detail in section 2.2.1.). In the end, the image is converted back to the original color space (RGB color space), also with (MathWorks) and (MathWorks). The luminosity image (L) manipulation in the L*a*b color space by multiplying a constant factor, can increase or diminish the overall pixel intensity on the RGB image (visible when converted back). On the other hand, the implementation of a CLAHE on the image components can enhance the contrast between the colors on the different stains, thus increasing the discriminative power of a posterior segmentation algorithm.

The **HSV color space** transformation was also implemented, applying (MathWorks), in a similar framework as the previous one, therefore enabling the manipulation of each channel independently, the Hue (H), the Saturation (S) and Value (V) channels. To perform an accurate conversion this method requires a normalized RGB image (image pixel intensities ranging from zero to one, i.e. a different type of normalization than the previously described in this section – Feature scaling normalization), and the Saturation and Value channels are determined from the original RGB channels according to equations (6, 7):

$$S = \frac{(max - min)}{max} \qquad (6)$$

$$V = max \qquad (7)$$

where max and min are the maximum and minimum intensity value among the RGB triplet of the pixel. The previous conversion equations and the Hue matrix determination were performed according to (Ford and Roberts 1998). The saturation was the most interesting channel to study since its enhancement originates images with more vivid colors, thus leading to a better differentiation between different tissues. To acquire this enhancement the Saturation channel was multiplied by a constant factor, as opposed to the first method (CIE L*a*b conversion). After this, the HSV image is reconverted to the RGB color space, using (MathWorks), where the impact of the referred operation can be verified.

The last color space transformation technique is characterized by the improvement of color contrast in RGB images through image processing operations in the **YCbCr color space.** The transition to this color space is characterized by the transformation of Red, Green and Blue channels into luminance (Y) and chrominance (Cb – blue; Cr – red) information, performed with (MathWorks), and the conversion equations behind it are described below (8, 9 and 10):

$$Y = 16 + (65.481R + 128.553G + 24.966B) \qquad (8)$$

$$Cb = 128 + (-37.797R - 74.203G + 112.0B) \qquad (9)$$

$$Cr = 128 + (112.0R - 93.786G - 18.214B) \qquad (10)$$

where Y is the luminance value, Cb and Cr the chrominance values blue and red, respectively, and R, G and B the RGB triplet for the considered image pixel (Ford and Roberts 1998). The YCbCr image enhancement is performed through multiplication of a factor, as in previously described color space transformation methods, in the luminance channel and the blue chrominance component (Cb), independently. Then, the YCbCr image is converted back with the reverse operation, through (MathWorks), to the RGB color space, where the changes applied are verified.

The last pre-processing methodology developed to enhance the color contrast in H&E stained tissues is based on **contrast limited histogram equalization (CLAHE)**, a method already stated in this section, based on (MathWorks), and applied directly to each color channel separately. After this, the channels are concatenated to form an RGB image. A similar method, but with histogram equalization (CLAHE) only being applied to the red grayscale image channel was also developed, termed in this work as CLAHE-red, leaving unaltered the green and blue channels, before the channel concatenation.

Aiming to eliminate the background, thus increasing the influence of the relevant image structures in the segmentation process, a masking process was developed, combining some of the techniques already described in this section with morphological operators. The framework behind it includes, first, a HSV color space transformation enhancing the saturation channel, followed by an YCbCr conversion, with blue chrominance (Cb) histogram equalization. The image threshold (section 2.2.2.) for the Cb grayscale image is determined using the Otsu algorithm (Otsu 1975), and then applied to the image to obtain a binary mask of the relevant structure in the image (the background intensity becomes 0). The final mask is obtained after small adjustments with morphological operators, namely image closing and opening (inthis order).

The effectiveness of all the presented image pre-processing methods was tested with a kmeans algorithm (section 2.2.2.), based on (Mathworks), upgraded to perform colored image segmentation. This clustering algorithm was implemented in this stage due to its simplicity and low computational cost, enabling the image segmentation in multiple classes, or, in this case, cell tissues, to determine the top-performing pre-processing method in stain color discrimination. The color upgrade was achieved by reshaping the incoming RGB image matrix to a row × column × 3 matrix, thus gathering on each column the pixel intensity information of each color channel image. These pixel intensity triplets were used in the segmentation procedure to discriminate classes. The kmeans was applied for 3 and then for 4 classes, in order to separate the image background from two or three different cell tissues.

The general scheme of the first workflow implemented is presented in Figure 22.

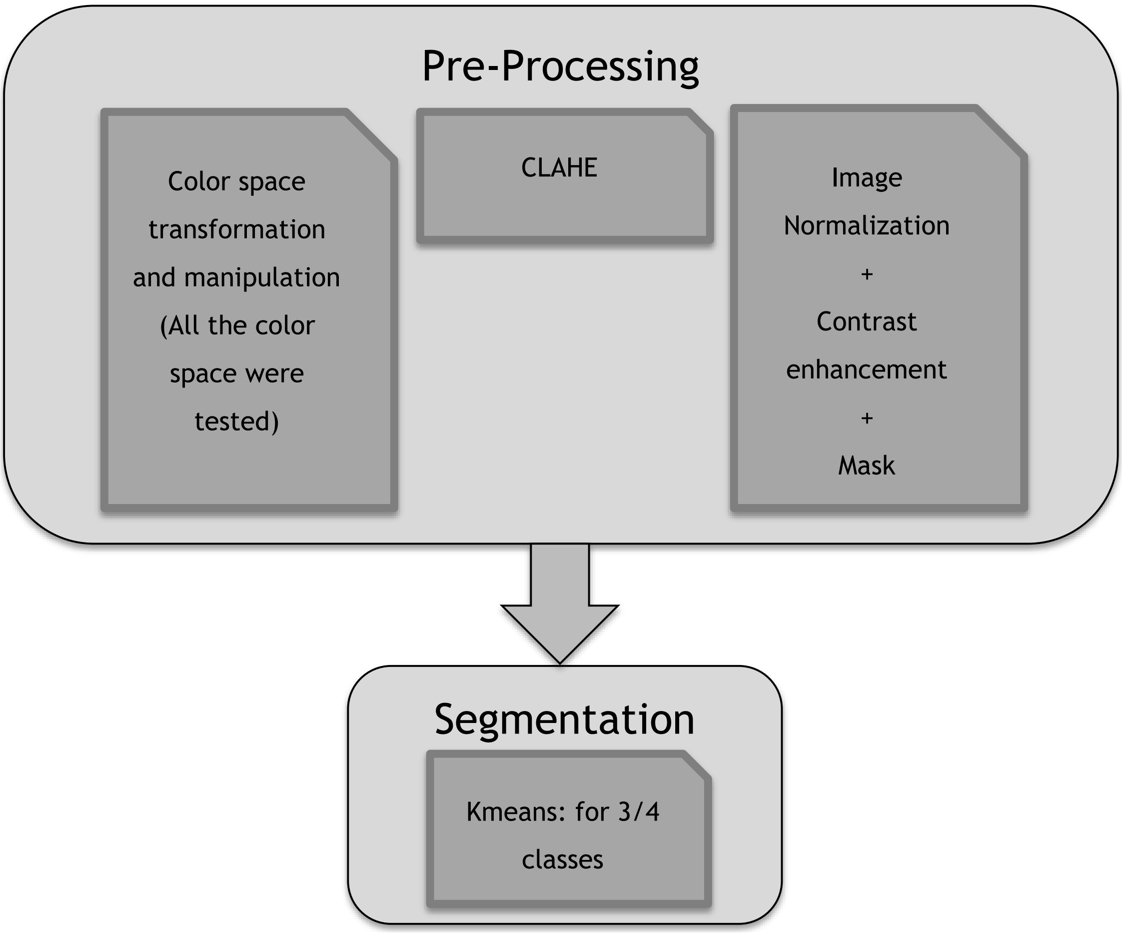

Figure 22. Schematic model representing the first workflow implemented in the study. Several contrast enhancement pre-processing techniques were applied to the dataset, and their efficiency was tested with the kmeans algorithm, for 3 and 4 classes.

3.2.2. Second Approach – Based on Image Registration

The knowledge acquired from the pre-processing study, concerning the best methods to provide an accurate segmentation, led to the registration test, where several registration techniques were approached. To determine the most appropriate, two criteria were taken into account: the DICE score (Sørensen 1948, Cheung 2012) and the computational cost.

Four registration algorithms were tested in two different registration models, pairwise and reference slice (more details in section 2.3.).

The first algorithm implemented is a feature-based registration method and the second an intensity-based algorithm. The feature registration method only enables rotation and translation to the moving images, since the only type of transformation implemented is similarity. On the other hand, the intensity–based model allows other two types of transformation, the rigid and the affine (section 2.3.). The other two algorithms tested, the Demon algorithm and the B-spline algorithm, which are both capable of performing non-rigid registration. All these methods are explained further in this section.

The **automatic feature-based registration** starts by detecting image features in both images, moving and fixed, mainly through the implementation of the Speed-Up Robust Features (SURF) algorithm (Bay, Ess et al. 2008), an algorithm that searches blob features, regions of the image where several properties (for example, brightness and intensity) remain constant. The detected features are then extracted including their location in the image, through the pixels surrounding the interest point or feature blob (Bay, Ess et al. 2008). The detected and extracted feature regions in the moving and fixed images are matched using parallel hierarchical clustering trees (Muja and Lowe 2012), resulting in a pair of indexes from the matched features. The locations of those matching points are also retrieved and the transformation is performed based on the matched points of both fixed and moving image, resorting to M-estimator Sample Consensus (MSAC) algorithm (Torr and Zisserman 2000) to exclude outliers. The inliers of both sets of matching points are mapped and originate a 2D geometric transform object (Hartley and Zisserman 2003). In the last step, the geometric transformation object generated is applied to the moving image, creating this way the registered image. The scale and angle applied (considering that it is a similarity transform) with the transform object to create the final image are recovered to serve as quality control of the whole procedure, allowing this way the removal of completely distorted images, possible outcomes of the registration process. The stated framework was performed based on (MathWorks).

Concerning the **intensity-based registration** three key components have to be previously defined in order to configure the whole registration process, the optimizer, the metric and the transformation type (section 2.3.). The metric is, in fact, the image similarity metric responsible for evaluating the registration's accuracy and the optimizer (Regular Step Gradient Optimizer, whose algorithm is described in (Pennec, Cachier et al. 1999)) defines the procedure for minimization or maximization of this similarity metric (Mean Squares metric implementation in (MathWorks)). This registration method is an iterative process that can be performed in three different transformation types (rigid, similarity and affine) and always requires two images, a fixed and a moving image. The whole registration process starts with an internally determined transformation matrix combined with the transformation type specified, determining the image transformation that is going to be applied to the moving image with bilinear interpolation (MathWorks). After the interpolation the metric compares both transformed moving image and fixed image, computing the metric value and then the optimizer checks for ending conditions to stop the registration process. These conditions can be the maximum number of iterations (defined by the optimizer) or a certain metric value threshold. If the stop condition does not verify the optimizer adjusts the transformation matrix to initiate a new registration cycle. The maximum number of iterations and the optimizer step size the registration can be altered to improve the registration, but always with a greater computational cost (MathWorks). The explained workflow is presented in Figure 23Figure 23.

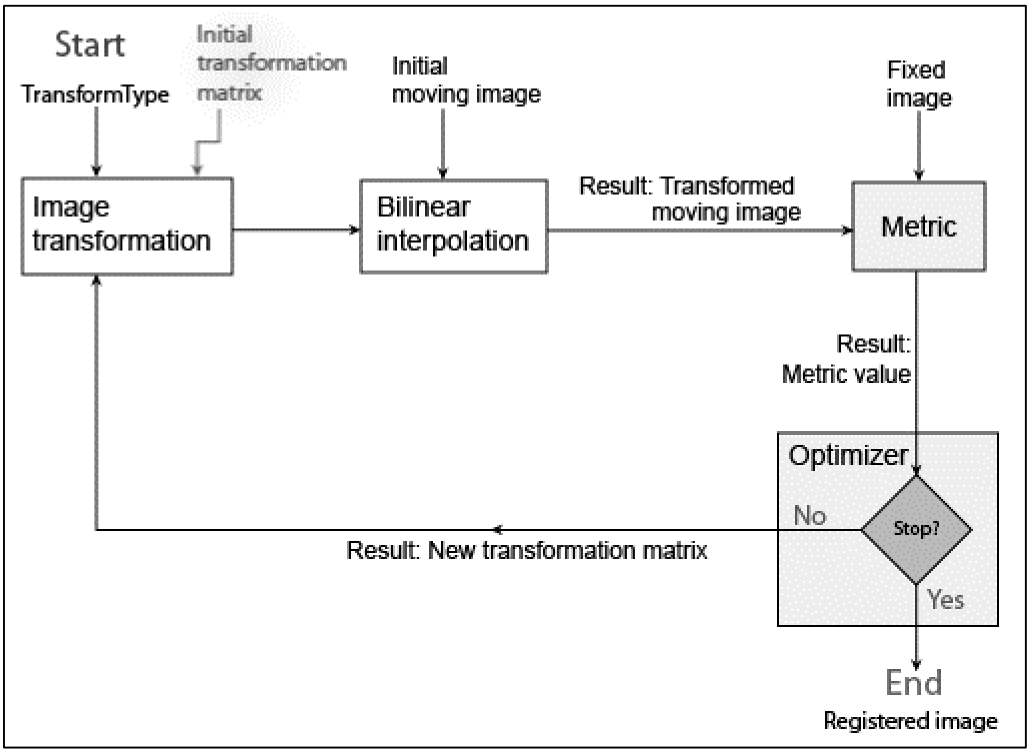

Figure 23. Representation of the intensity-based registration framework implemented. Adapted from (MathWorks).

The first non-rigid registration methodology tested was the **B-Spline Grid, Image and Point Registration** developed by (Kroon 2008), based on the algorithm developed in (Rueckert, Sonoda et al. 1999). This is an intensity based registration technique whose algorithm implements a grid of B-spline control points (section 2.3.) that control the transformation of the moving image over the fixed one. It measures the registration error, through squared pixel distance (Vercauteren, Pennec et al. 2009), a similarity criterion based on the information theory and calculates the amount of information existent in the registered moving image about the fixed one (considering a registration procedure). The B-Spline method applies the Fast Limited Memory Optimizer (Kroon 2009), a Quasi-Newton optimizer, to move the control points, in order to achieve the optimal registration between both images with minimal similarity error. The implemented B-Spline method can also performed rigid and affine transformations (section 2.3.).

The **Demon algorithm** is a non-rigid registration technique faster and rather simpler than the B-Spline. This algorithm was first described by (Thirion 1998) and followed by (Wang, Dong et al. 2005), and the methodology followed in the present study was developed by (Kroon 2008). For each pixel a velocity, or movement, is defined by this method, using the intensity differences and gradient information. The velocity matrix is smoothed by a Gaussian filter and iteratively applied to transform the moving image and register it onto the fixed image. The transformation is optimized by a limit memory BFGS optimizer (Liu and Nocedal 1989) in an iterative and multi-resolution way. The Demon algorithm also performs affine registration (section 2.3.).

In the second approach were also tested combinations of the previously described algorithms, starting with a rigid registration technique followed by a more accurate and computational demanding non-rigid registration algorithm, as performed in previous studies (Roberts, Magee et al. 2012).

In order to align all the images from the datasets available, two different registration models, the reference slice model and the pairwise model, were implemented for all the abovementioned registration methods, starting from the middle slice (in the datasets) since, generally, it is the section with most tissue (Roberts, Magee et al. 2012). Through the reference model the registration procedure is performed considering only as fixed image the middle slice from the image dataset, thus, being all the slices registered to reference section. The pairwise model is performed in a cascade process starting from the center slice and performing registration in pairs of slices (moving image becomes fixed image in the next alignment) in two directions - until the top slice in the first run and the first slice in the second run.

The workflow of the registration approach combined with the best suited pre-processing method is presented in Figure 24.

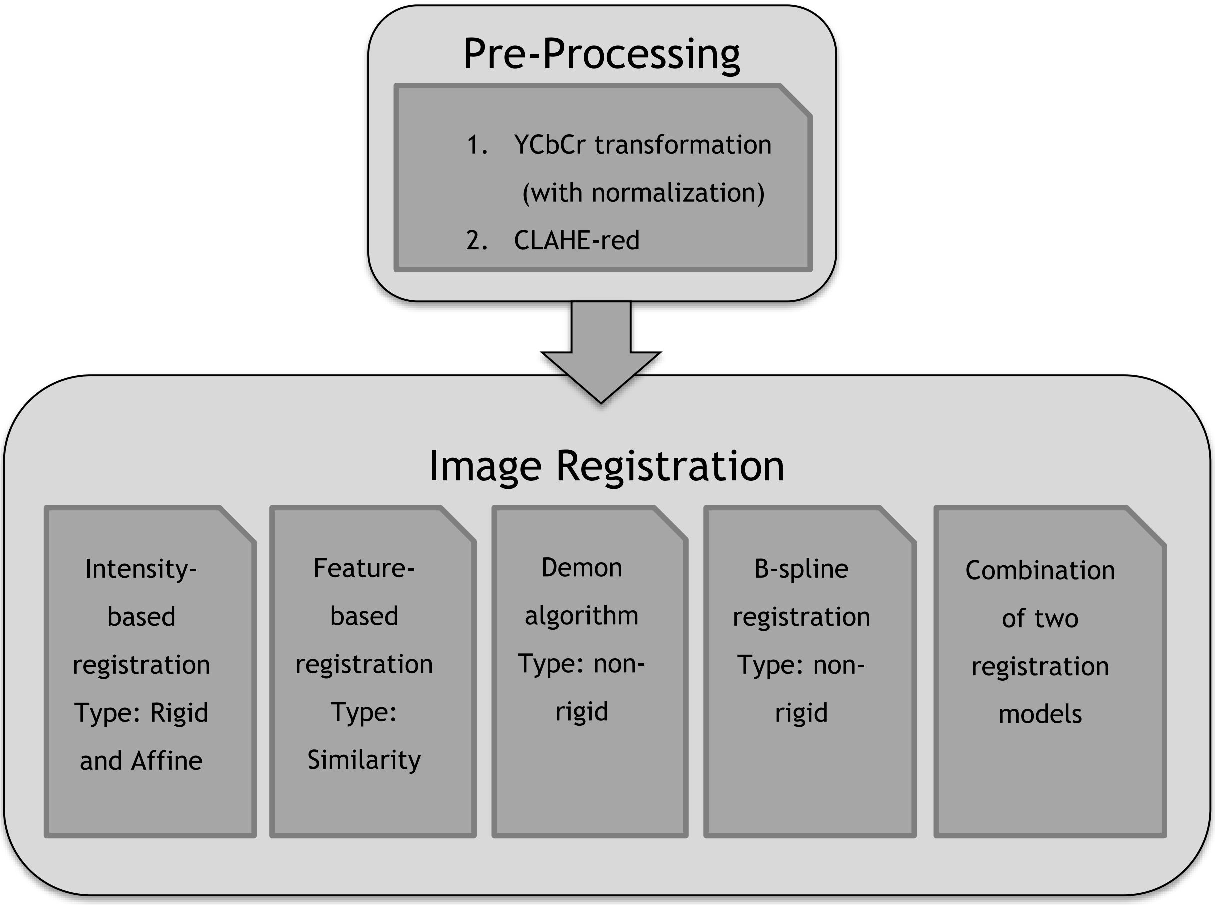

Figure 24. Schematic model representing the second workflow implemented in the study. In the first step, the most successful pre-processing method was applied to the image dataset, followed by the image registration step, with several methods being tested.

3.2.3. Final Approach – Based on the complete workflow with the 3D reconstruction

In the third and final approach, the most successful pre-processing and registration method, or combined methods, for the tested image datasets were connected and the 3D reconstruction final step was added to the workflow.

In the pre-processing stage the previously tested methods were subjected to an efficiency test, but to a different segmentation technique, the stain deconvolution method, explained in more detail further in this section. The method implemented for this first step was the CLAHE but with a difference in the algorithm presented in the section 3.2.1., since only the red channel was subjected to the histogram equalization. This was performed due to the high influence of the red channel in both Hematoxylin and Eosin stain, proving, through the segmentation, to be the best stain discriminant method. The image was also subjected to a FIR filter (filters with finite impulse response) convolution to remove line artifacts or deformations on the analyzed slice (section 3.1.).

The **stain deconvolution** technique developed for this study was based on the work carried out by (Ruifrok and Johnston 2001, Chan 2013) and also from (Unpublished 2015). The stain deconvolution is a segmentation method that is capable of deconvolve a stained image (for example with H&E) and generate separate images, each one with the distribution of a single stain (Hematoxylin, Eosin and Background, in the case of the tested datasets). This method assumes that the chemicals employed to stain the tissues slides follow the Beer-Lambert Law of absorption (11):

$$I = I_o e^{-SD} \qquad (11)$$

where I is the RGB image, I_o is the intensity of the source, D the stain density map and S the stain absorption matrix. This equation grants a logarithmic relation between the original RGB color channels and the stain intensities. The implemented algorithm starts by converting the RGB image I into the optical density place (OD) - I_{OD} - through the previous equation in the form (12):

$$I_{OD} = -\log\left(\frac{I}{I_o}\right) \qquad (12)$$

After the OD conversion, the image pixels are projected into the Maxwellian chromaticity plane. In the Maxwellian plane the distance between two points is proportional to their chromatic dissemblance (Maxwell and Zaidi 1993), or within this study, the pixels that belong to the same stain are projected closer than the pixels belonging to different stains. To calculate the pair of corresponding Maxwellian coordinates $(m1, m2)$ for each pixel p, the following equation (13) was implemented:

$$\begin{bmatrix} m1 \\ m2 \end{bmatrix} = \begin{bmatrix} 0.7071 & -0.7071 & 0 \\ -0.4082 & -0.4082 & 0.8165 \end{bmatrix} \frac{p}{\|p\|_1} \qquad (13)$$

The described Maxwellian plane property and the pair of Maxwellian coordinates allows the implementation of an unsupervised classifier, for example kmeans, to assign a label for each pixel according to its stain. With the classification performed, the following step is the Stain Matrix estimation. For this study, it is considered the existence of three stains or classes, the Hematoxylin (class 1), Eosin (class 2) and the Background (class 3). The Maxwellian coordinates of the mean value in each of these classes - $\mu_c = (\mu_{m1c}, \mu_{m2c})$, obtained through the kmeans classification, is converted back to the OD space through the equations (14) exposed below:

$$\begin{aligned} S_{c,r} &= 0.7071\mu_{m1c} - 0.4082\mu_{m2c} + 0.33 \\ S_{c,g} &= -0.7071\mu_{m1c} - 0.4082\mu_{m2c} + 0.33 \\ S_{c,b} &= 1 - S_{c,r} - S_{c,g} \end{aligned} \qquad (14)$$

where $S_{c,r}$ is the red channel value for the stain vector of the class c, $S_{c,g}$ the green channel value and $S_{c,b}$ the blue channel counterpart. The stain vector is generated for each class c by $S_c = \left[S_{c,r}, S_{c,g}, S_{c,b}\right]^T$, and, in turn, the stain matrix by $S = [S_1, S_2, S_3]$, being $c = 1{,}2{,}3$ the H, E and B stains, respectively. The stain density map D is obtained through the inverse of the stain matrix as demonstrated in equation (15):

$$D = S^{-1} I_{OD} \qquad (15)$$

The created stain matrix is then applied to the OD image to each pixel to obtain a final three channel image, composed by images from the three different stains, Hematoxylin, Eosin and Background. The stain images are separated and the first two, the relevant stains, suffer a contrast enhancement process. The contrast enhancement method embedded in the stain deconvolution framework performs a mapping of intensity values in grayscale images, so that the output data (image) presents a saturation of 1 % in high and low intensities, thus an increased contrast in intensities (MathWorks).

The registration method implemented was the **automatic intensity-based registration algorithm** (section 3.2.2.) with transform type rigid and performed taking as constant fixed image the reference slice of the image dataset (the central slice), and as moving images all the slices successively, from the first to the last in the dataset, aligning them to the reference and stacking them to form volumetric data.

To execute the 3D reconstruction and display were implemented using two different frameworks. The algorithms tested were the Marching Cubes algorithm (Lorensen and Cline 1987) implemented by (Hammer 2011) and the Isosurface framework from (MathWorks), adapted for the image datasets tested in this study.

The **Marching Cubes algorithm** creates polygonal surface representations of isosurfaces (Lorensen and Cline 1987) of 3D scalar fields, such as the slice stack formed after the registration complete process over all the dataset images. The implemented method consists in a vectorized version of the algorithm, which computes a triangulated mesh of the isosurface within a given 3D matrix of scalar values, according to the isosurface value (the constant value or level set from the 3D image represented in the isosurface), and specified in terms of a face and vertex list. The orientation of the triangles generated is selected according to the normal point from higher to lower values (Hammer 2011). This method enables the visualization of the generated 3D surface, with customizable colors and view.

The **Isosurface framework** from (MathWorks) also performs the extraction of the isosurface data from volumetric according to an isosurface value, although with a different process. This method performs first a volumetric interpolation using linear interpolation with (MathWorks), and then connects the points with equal isosurface value, forming a three dimensional surface. This method is combined with a 3D data smoothing technique (MathWorks) to smooth the edges of the reconstructed surface and a 2D polygon filling method (MathWorks) to enable its coloring and visualization.

The final workflow schematic representation is shown in Figure 25.

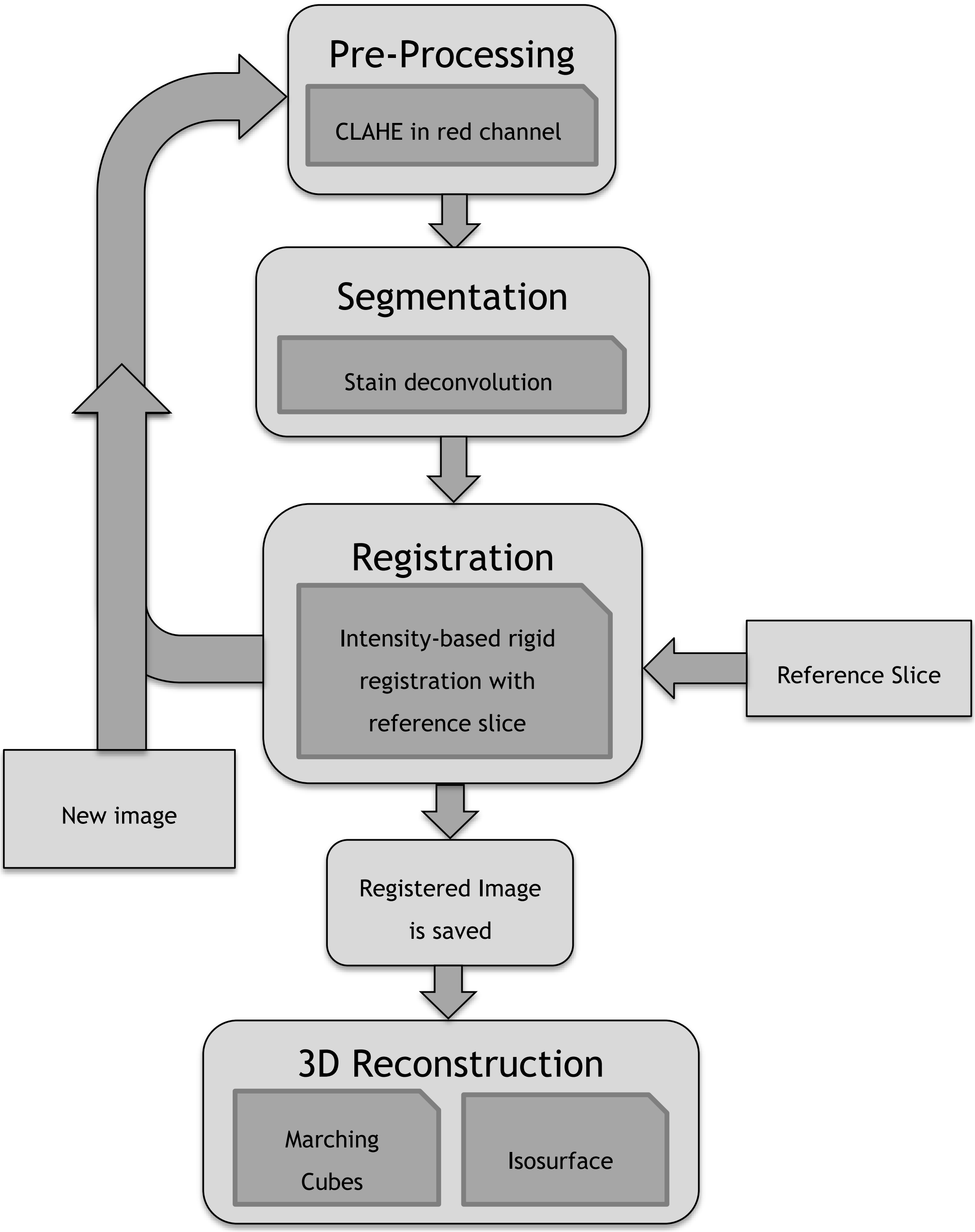

Figure 25. Schematic model representing the third and final workflow implemented in the study. The approach starts by computing a loop for each slice in the dataset (minus the reference middle slice) in which the image suffers pre-processing, segmentation through stain deconvolution and registration with the reference slice as fixed image. All the registered images are stored and stacked to form the 3D data dataset, which will, posteriorly, serve as input of both 3D reconstruction frameworks.

Chapter 4

Results and Discussion

In this chapter, all the experimental results obtained with the three approaches described in the methodology (Chapter 3) and their respective discussion are presented. The pre-processing results will be the first to be analyzed, based on color contrast enhancement and segmentation results, followed by registration frameworks comparison and evaluation (second approach). Finally, the final workflow will be discussed, finishing with the 3D reconstruction results. All the selected parameters and decisions performed are properly indicated and justified, throughout the entire chapter. The workflows in this study were tested on a Windows 64bit Intel Core i7-4700HQ CPU at 2.40 GHz, with 8 GB of RAM computer system.

4.1. Pre-processing stage

In this section, results from the application of pre-processing methods, addressed in the first approach (section 3.2.1.) will be presented and discussed further in this section. In the end, the best methods or workflows will be determined based on visual interpretation and a segmentation test, performed with kmeans algorithm.

Observing all the lesions and their description, in section 3.1.2., found in images from the three datasets, it can be concluded that they present very distinct natures and occur stained by both hematoxylin and eosin stains, in a wide range of color intensities. In light of the previous, the pre-processing techniques were developed focusing the color contrast enhancement and ultimately the distinction between tissues stained with each one of these stains.

The resultant images after implementation of the pre-processing techniques, presented throughout this section, applied to a single slice from the second dataset, serving as an illustrative example. The original image from the selected slice (nº 35) is presented in Figure 26.

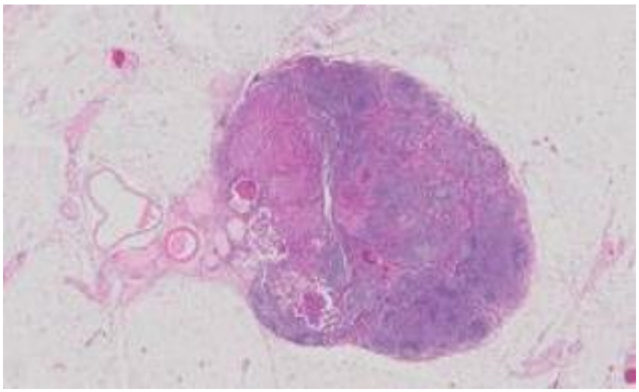

Figure 26. Original image (slice n°35) from the second dataset.

Considering the analysis performed in tissue sections from case 2 by a histopathologist, described in section 3.1.2., the effectiveness of each pre-processing method applied will be discussed, concerning the color contrast between different tissues.

The first procedure implemented was a **color channel decomposition** from the original RGB image, to ascertain the color channel most suited for color discrimination, mainly between lesion and healthy tissues. The resultant images are presented in Figure 27.

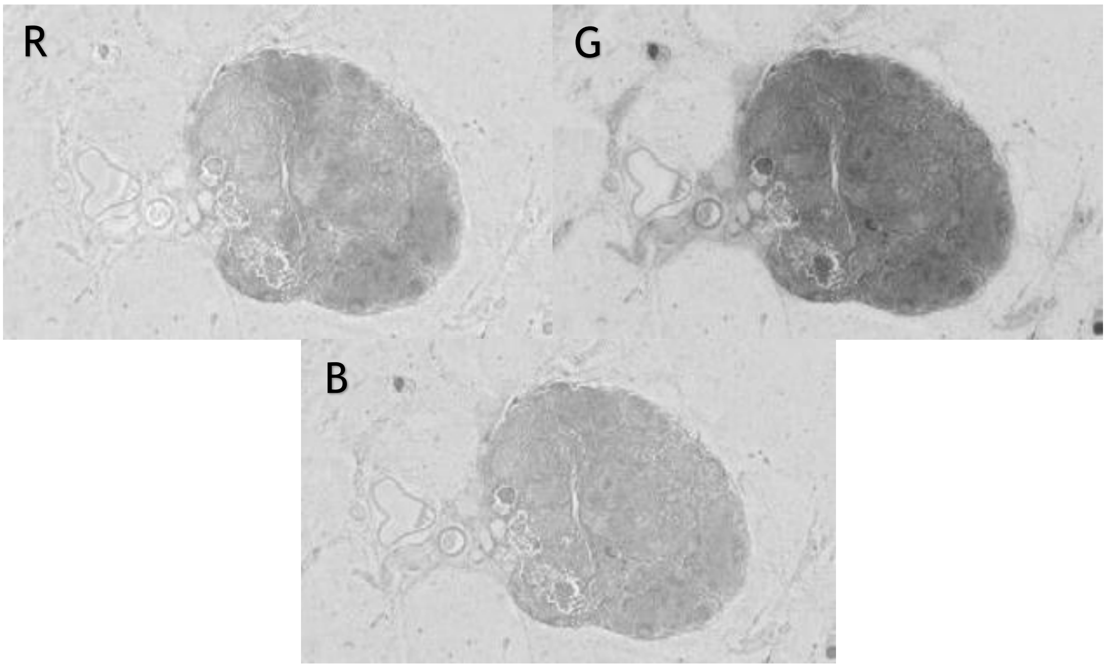

Figure 27. Resultant images of color channel extraction from the original image. Red channel grayscale image – R, Green channel image – G and Blue channel image – B.

Through image comparison it is possible to conclude that the color channel that better differentiates the relevant tissues from the healthy tissues in the lymph node is the red channel (Figure 27, image R), where the lowest pixel intensity corresponds to healthy tissues. Despite being the best channel to process in order to highlight the lesion tissues, the green image is also relevant, since it is the one that presents the greater contrast between lymph node and background. With these results in mind, several pre-processing methods, focusing color contrast enhancement, were tested and their results explored further in this section.

A **CLAHE** method was applied to each color channel independently to increase the contrast between pixel intensities of different tissues, in each color image. The resulting images are shown in Figure 28. These images were concatenated to create an RGB image with a clearer distinction (RGB equalized image), visible in Figure 29.a. This image demonstrates the efficiency of this technique, applied to grayscale images to obtain RGB with higher color contrast, fundamental to provide a better differentiation between the tissues. The CLAHE window of operation (adaptive method) was the same for each image, a 4x4 window, as well as the Clip Limit, of 0.01 (clip limit is the normalized value, between 0 and 1; Higher clip limit values will cut fewer values and, consequently, they will be spread out more, hence increasing the contrast). These parameters were determined by trial and error, to obtain the better contrast in the RGB final image. Since the red channel presents more color contrast information between hematoxylin and eosin stained tissues, another CLAHE approach was developed (CLAHE-red), in which only the red channel grayscale image was subjected to the histogram equalization, leaving both green and blue images unaltered. The resultant image is presented on Figure 29.b to be compared with the previous CLAHE method.

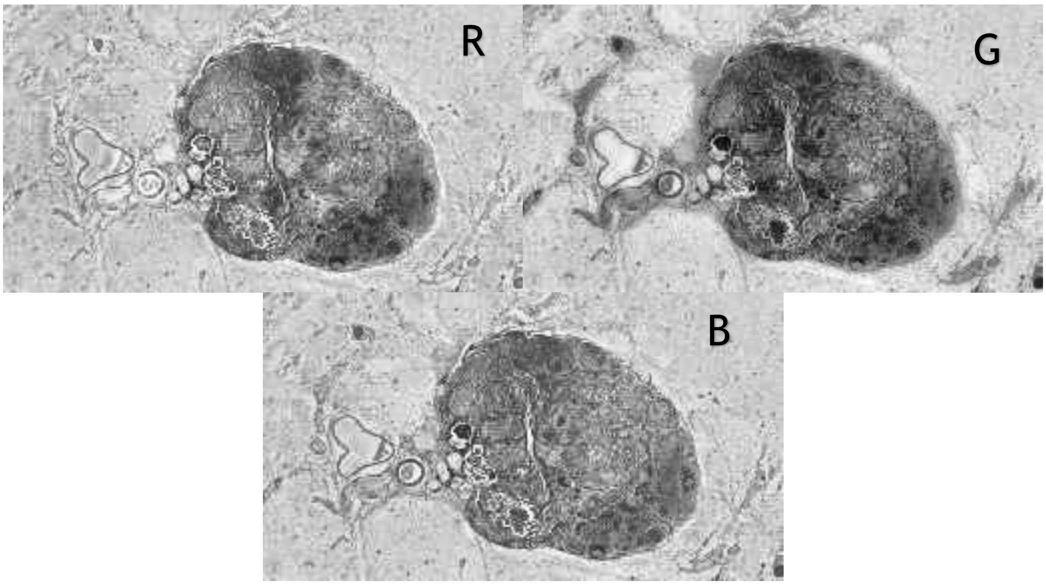

Figure 28. Images obtained through CLAHE implementation on the original RGB image channels. Image resultant from red image histogram equalization (R), Green image (G) and Blue counterpart (B).

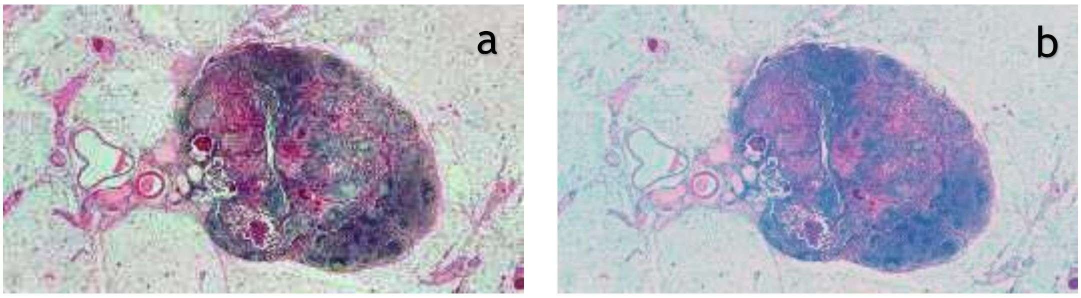

Figure 29. RGB image obtained after CLAHE operation in each color channel image from the original image and posterior concatenation of the channels (a). RGB image obtained after CLAHE-red operation in the red channel and posterior concatenation with unaltered green and blue channels (b).

Visualizing the histogram equalized images of the color channels, in Figure 28, it is evident an overall contrast enhancement in grayscale pixel intensities and image sharpening, when compared to the original color channels (Figure 27). Also, the previous statement indicating the red channel image as the most valuable for tissue discrimination is corroborated by these CLAHE-red results, where it can be seen a more pronounced distinction between different tissues in the lymph node. By using a 4x4 window it was small enough to perform a local contrast enhancement, but not too reduced to be affected by small image artifacts with high or low intensities. Analyzing the RGB image formed by the equalized images, in Figure 29, it stands out the color contrast between tissues stained with Hematoxylin (nucleus) in blue, and Eosin in magenta, clearly enhancing the stain differentiation, when compared to the original image (Figure 26). This pre-processing method is also better than the all-channel CLAHE (Figure 29.a) because not only the colors exhibited by the tissues are more resembling to the hematoxylin and eosin stains but also the image color sharpness is reduced, contributing to the segmentation process.

The **image normalization** technique, presented in section 3.2.1., was also tested for all the datasets and the result of this operation in slice 35 of case 2 can be observed in Figure 30. This procedure was implemented to produce images suitable to create masks, aiming to remove the background. The removal of this element can reduce the computational cost and improve the efficiency of segmentation procedures in the image. The normalization was applied to each color channel image, from the original RGB slice, separately and then concatenated to originate a final RGB normalized image. The normalized channels can be observed in Figure 31.

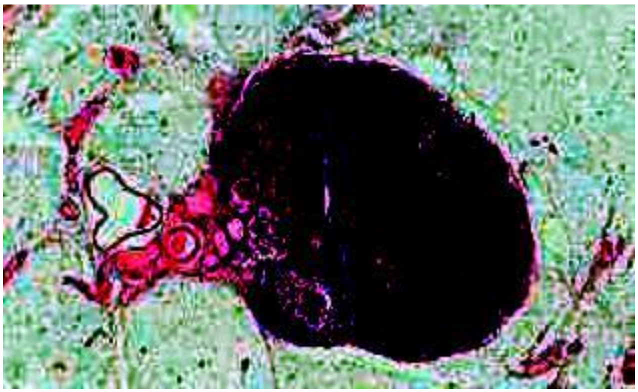

Figure 30. Normalized RGB image resultant from the Normalization technique described in section 3.2.1.

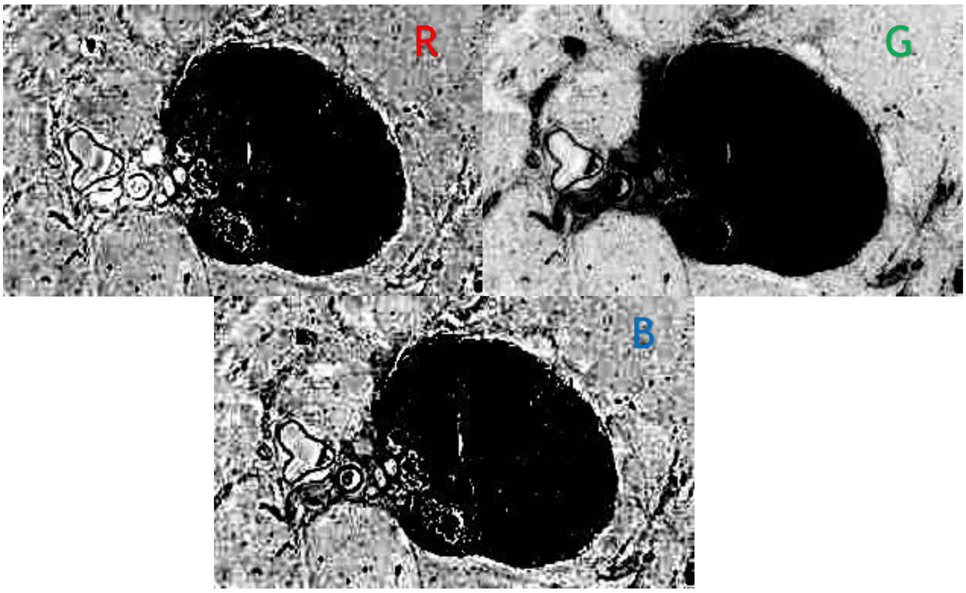

Figure 31. Images resultant of the normalization procedure to each color channel (Red – R, Green – G and Blue – B).

On Figure 31, it is possible to observe the outcomes of image normalization in each color channel from the original RGB image. Comparing the three images it is clear that the most suited one to produce masks, to remove the background, is the green channel image, due to the higher contrast between foreground (lymph node) and background. The red image is also interesting to mask not only the background but also the blood vessels (see Figure 19, form section 3.1.2.), that appear with intensities closer to the background pixels, unlike in the other two images. Since these structures (blood vessels) present closer colors to the lesion tissue pixels they can be misclassified as lesion in the segmentation procedure, hence the importance of removing blood vessels from the image. The final RGB normalized image (Figure 30), obtained through concatenation of the three normalized channels, although not presenting any detail or structure inside the lymph node it presents a higher contrast against the background than each separate channel. This allied to fact that the blood vessel area presents an intermediate color between foreground and background, proves the relevance of this technique to create masks for color images, in particular for tissue sections stained with H&E.

Concerning the color space transformations, the first one tested was the **HSV conversion**. The original RGB image was converted to this color space, also composed by three channels (section 3.2.1.), where its color saturation (second channel) was enhanced by a multiplying factor. The images are then, converted back to the RGB color space to assess the effect of the produced modifications on the image's colors. The factor was modified to find the most appropriate value to enhance the image color saturation, therefore to better distinguish the lesion from healthy tissues. Images resultant from the application of various factor values are presented in Figure 32, from 2x to 4x saturation increase.

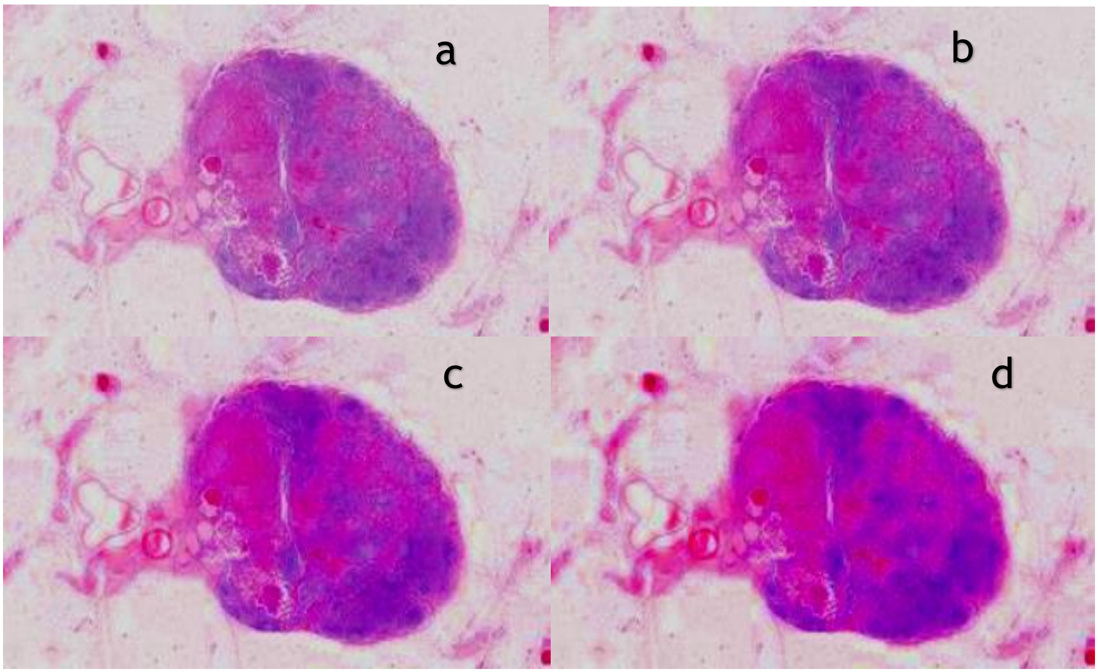

Figure 32. Images obtained with HSV color transformation with four different saturation enhancement factors, from the original image. Image (a) is 2x, image (b) is 2.5x, image (c) is 3x and (d) is 4x.

Analyzing the resultant images from this method, in Figure 32, considering four different saturation factors (2x, 2.5x, 3x and 4x), it can be concluded that by increasing the multiplying factor the tissue stain colors become more vivid, thus the differences between them become more evident. This occurs until a certain point, visible in image (c) where due to the increased saturation and subsequent high intensity colors, the dimensions and shape of the different tissue regions become sparse, therefore, corrupting the image, being even more noticeable in image (d). In face of the previous facts and by observation, it is concluded that the saturation enhancement factor responsible for the better color contrast is 2.5x, as it can be seen in Figure 32.b where the purple tissues – Hematoxylin and pink tissues – Eosin are clearly defined.

A conversion to the **CIE L*a*b color space** was also applied to the original image. After the conversion, the luminance channel and both color components channels (a and b) were multiplied by a factor separately, in similar process to the HSV saturation enhancement. This operation was followed by a CLAHE to increase the contrast of pixel intensities in all the channels, applied with an 8x8 window and a Clip Limit of 0.09. These values and the best suited factors for the channels (L factor = 0.8, a Factor = 0.7, b factor = 1/200) were determined through experimentation. The image resultant from the application of this method with the previously referred values can be observed in Figure 33.

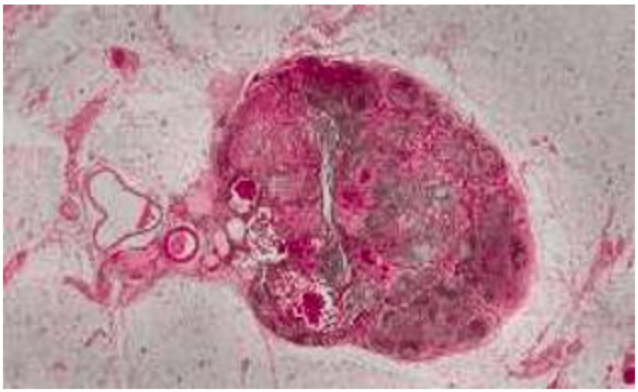

Figure 33. Image obtained through CIE L*a*b color space transformation, from the original image with all color channels enhanced separately by factors (Luminance – 0.8; a component – 0.7; b component – 1/200).

Observing Figure 33 it is possible to verify a color contrast enhancement between tissues stained with Eosin in shades of pink and the Hematoxylin stained tissues in a grayish brown. Although this method did not provide the best discrimination in terms of tissue types, it points out the color of the blood vessels from the overall eosin stained tissue, in a clearer manner when compared to previously implemented methods.

The last pre-processing method tested to increase the color contrast between the lesion and the other tissues corresponds to another color space transformation. The **YCbCr color space conversion** was applied to the original RGB image and, similarly to previous methods, some channels were enhanced. In the implemented transformation, both the Luminance (Y channel) and the blue chrominance (Cb channel) were multiplied by a diminution factor targeting the highlighting of lesion tissues over the other structures. This operation was optimized by trial and error and the most appropriate parameters were determined, and are presented below. Only after converting back to RGB color space the enhancement the outcome of the referred operations can be visualized. The output images resultant from this method and the influence of three different luminance factors (1/20, 1/40 and 1/80) were explored, using a constant blue chrominance factor – 1/16. The images obtained with this method and parameters presented an unnoticeable lymph node, with reduced sharpness and almost inconspicuous in terms of shape and/or appearance.

Therefore, and since this method is most suited to work on RGB normalized images (section 3.2.1), the same test was repeated, but this time applying the color space transformation to the resultant image from the normalization process (Figure 30). The results are presented in Figure 34, also for luminance factors 1/20, 1/40 and 1/80.

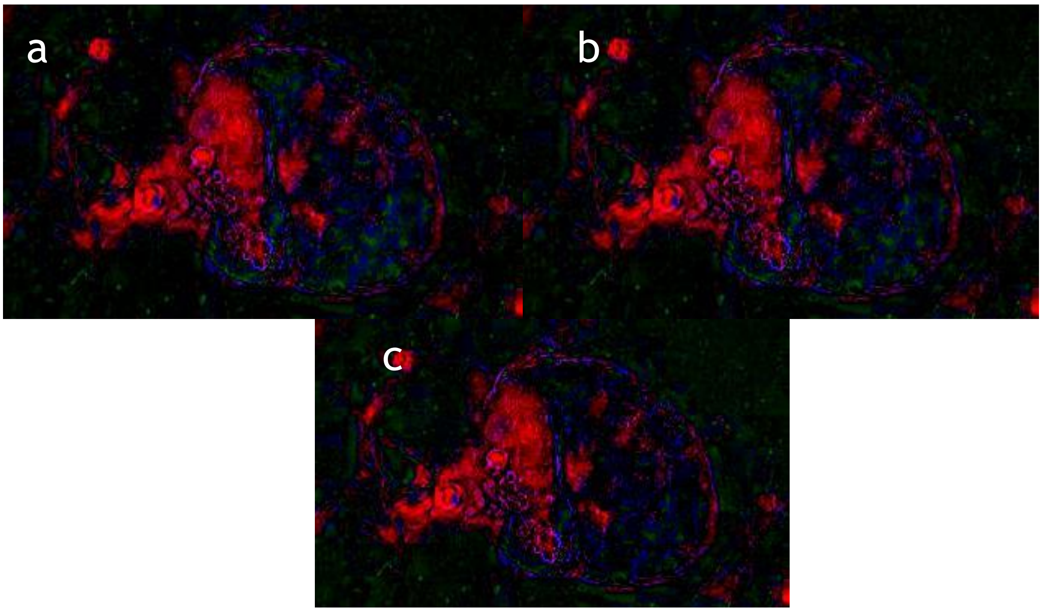

Figure 34. Resultant images from YCbCr color space transformation applied to the normalized RGB image (Figure 30), with constant Cb factor (1/16) and decreasing luminance multiplying factors - 1/20 (a), 1/40 (b) and 1/80 (c).

Analyzing the Figure 34, showing the result obtained when the YCbCr color space transformation is applied to the normalized image, outcome of the normalization method (Figure 30), it is evident the improvement in terms of image quality and sharpness. A general comparison between the three images shows that they are similar in terms of tissue colors among relevant structures, and thereby the diminution factors smaller than 1/20 do not increase the color contrast. The only difference between these images is the green color noise noticed among pixels from the background, which is higher for lower values. Considering this, the best suited diminution value for these images is 1/20x, since it provides a clearer discrimination between different stained tissues. This value, as well as the blue chrominance factor (1/16) were determined through experimentation, i.e. color contrast enhancement optimization. As noticeable in **Figure 34** the diminution of both factors results in an overall image darkening (luminance diminution), particularly in tissues stained with hematoxylin, due to higher blue color influence (blue chrominance diminution). The YCbCr color space transformation preceded by an image normalization was the most accomplished method, of the presented in this section, in increasing the color contrast between Hematoxylin stained, in deep blue shades, and Eosin stained tissues, in magenta.

The **masking method** developed for this study (section 3.2.1.) involved a combination of two color space transformation techniques, HSV and YCbCr, with the predetermined parameters (enhancement factors, 2x for HSV and 1/20x for YCbCr). An automatic threshold operation is followed, in order to create a binary image with the lymph node detached from the background. The final steps for this masking method includes two morphological operations, starting with an image closing, with a 4 pixel radius disk shaped structural element, followed by an image opening performed with the same element, but with 6 pixel radius. These steps were conducted to achieve a unique final mask structure, as the one presented in Figure 35, for the original image (Figure 26). The masking process is important to increase the influence of each different tissue to be segmented in the segmentation procedure.

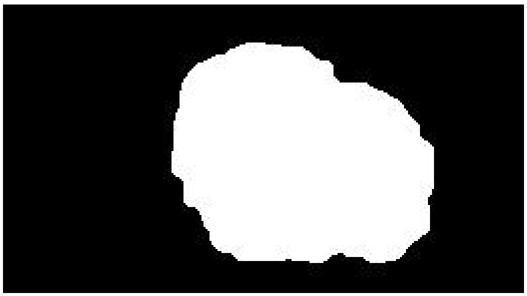

Figure 35. Mask structure, created from the original image to remove the background (a).

To corroborate the visual interpretation and selection of the most adequate pre-processing method to enhance color contrast based on the resultant images, in the datasets prepared for this study, a simple segmentation procedure was performed, using kmeans (section 2.2.2.) for each method and considering three different classes (hematoxylin stained tissues, eosin stained tissues and background), with 15 repetitions and using square Euclidean distance to assign the clusters. The segmentation results are shown in Figure 36 as well as the processed images used to acquire them, respectively, masked with the structure on Figure 35. Comparing the masked images originated from the different pre-processing methods and the respective three class segmentation result, represented in Figure 36, it is clearly noticeable that CLAHE and YCbCr transformation were the best performing methods in distinguishing the eosin and hematoxylin stained tissues. Although CLAHE was the top method to distinguish both stains in the segmentation (Figure 36.b), the YCbCr technique proved to be the best method to enhance the contrast between the lesion (neoplasic tissue) and healthy tissues, visible in the respective segmentation result (Figure 36.g). The three class segmentation result correspondent to the HSV enhancement presents mostly over segmented tissues, not being able to accurately find neither eosin nor hematoxylin stained tissues. On the contrary, the L*a*b transformation result presents under segmentation of both stains and an inconsistent pixel label throughout the entire lymph node.

Facing the previous results, and in an attempt to improve the segmentation accuracy another test was conducted but considering four classes, dealing this way with tissues presenting lower concentration on eosin stain color, and possibly segment additional tissues, such as the blood vessels. The segmentation results are presented on Figure 37.

Through comparison between the results for the four class segmentation and the 3 class counterpart in each image, it can be concluded that was an overall improvement in the tissue discrimination, more evident in the two methods with the worst outcome in the previous test (HSV and L*a*b color space transformation).

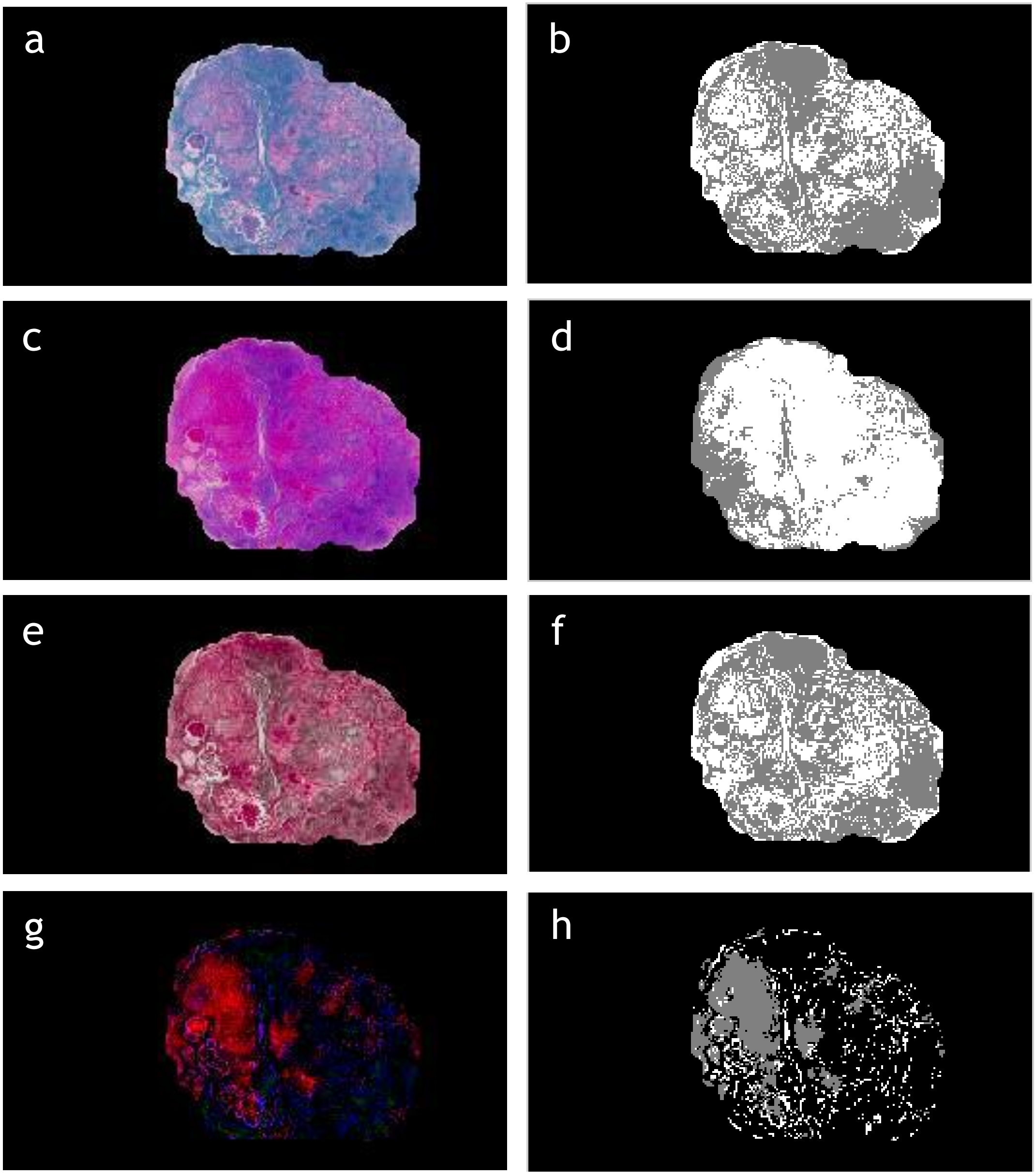

Figure 36. Masked images, resultant from the contrast enhancement techniques applied to the original image (left column) – CLAHE-red (a), HSV transformation (c), L*a*b transformation (e) and YCbCr transformation (g). Kmeans results of the respective left image (right column) considering 3 classes – CLAHE-red (b), HSV transformation (d), L*a*b transformation (f) and YCbCr transformation (h).

The CLAHE-red segmented image presents a higher differentiation in the tissue surrounding blood vessels, maintaining almost unaltered the other pixel's assigned labels, in relation to Figure 36.b. A similar comparison can be made for both YCbCr segmentation results, were the fourth label was assigned to pixels surrounding the blood vessels (Figure 37.d), although less evident than the CLAHE pixel labelling. Despite a considerable improvement in HSV transformed image segmentation, it does not present a satisfactory outcome, being a large amount of eosin stained tissue still with miss assigned labels. The CIE L*a*b results were clearly better than the previous segmentation, but also inconsistent, with a considerable amount of pixels belonging to hematoxylin and eosin stains being assigned to a third label.

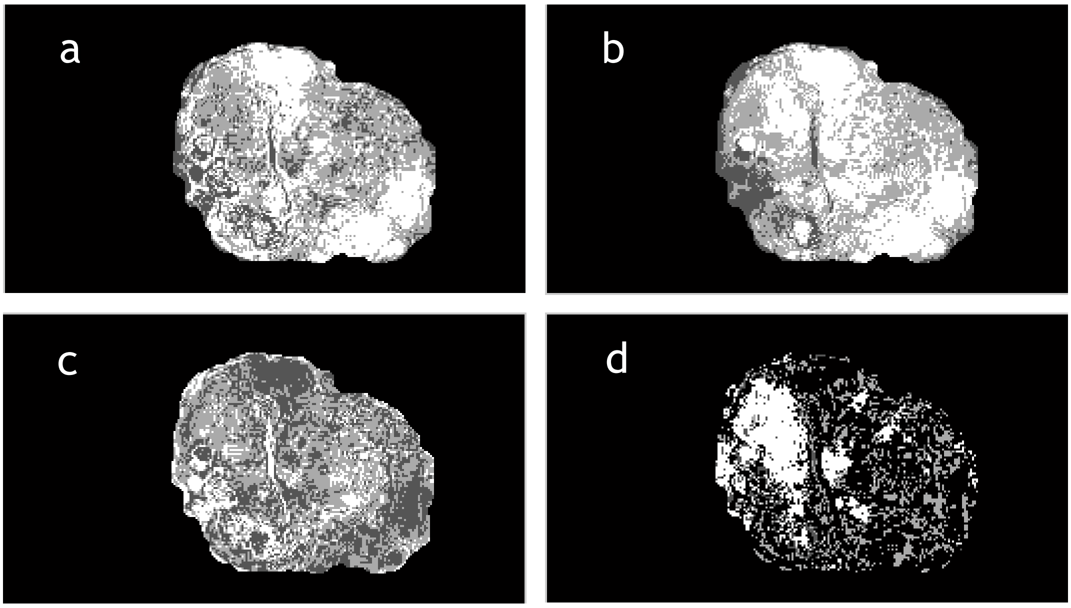

Figure 37. Segmentation results considering four classes, for CLAHE image (a), HSV enhanced image (b), L*a*b transformed image (c) and YCbCr image (d).

All things considered, and to assess the efficiency of top-performing pre-processing workflows, for stained tissues contrast enhancement, when applied to the other two datasets, the implementation was made and the resultant images are presented in Figure 40, regarding case 1, and Figure 39 for case 3. The selected slices, to serve as example (slice n°35), from case 1 and case 3 are shown in Figure 38.

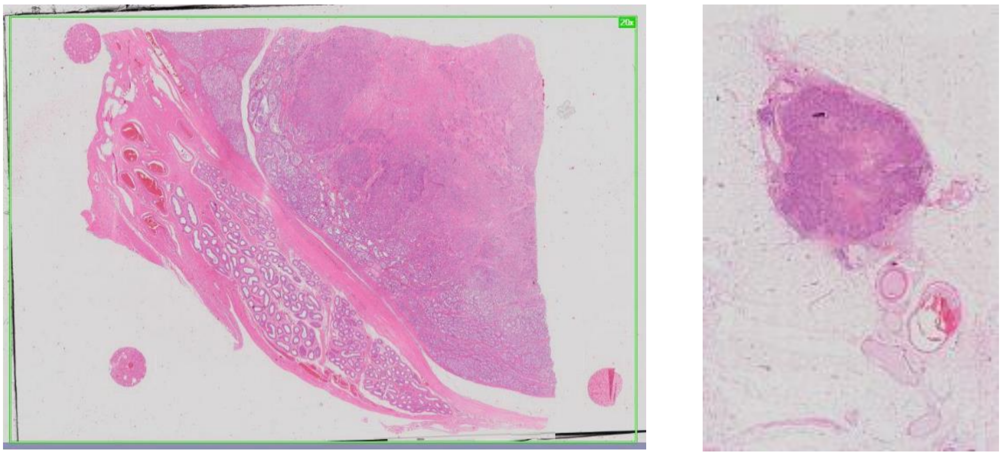

Figure 38. Original image (slice n° 35) from case 1 (on the left). Original image (slice n°35) from the third dataset (on the right).

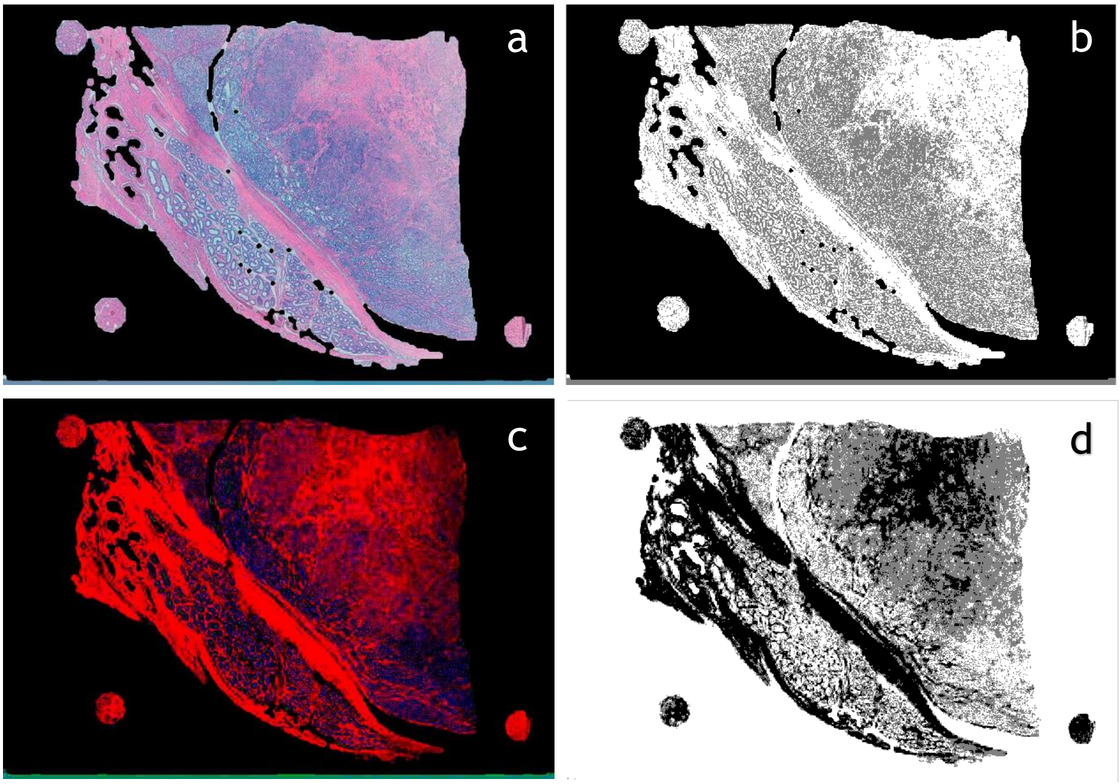

Figure 39. Masked images, resultant from the contrast enhancement techniques applied to the original image from case 1 – CLAHE-red (a), YCbCr (c). Results from kmeans segmentation performed in the respective left image (b, d).

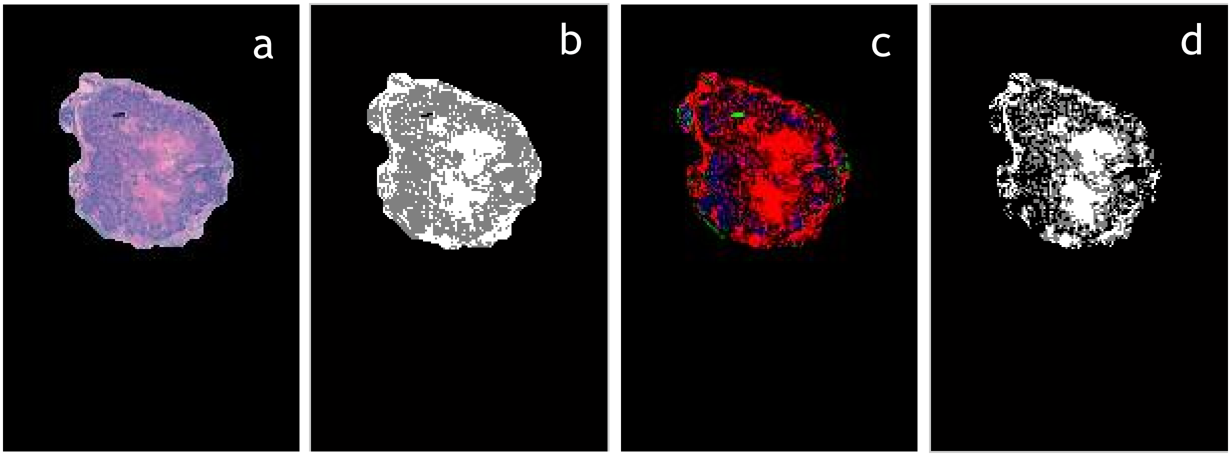

Figure 40. Masked images, resultant from the contrast enhancement techniques applied to the original image from case 3 – CLAHE-red (a) and YCbCr (c). Results from kmeans segmentation performed in the respective pre-processed image, for CLAHE-red is image (b) and for YCbCr is (d).

Analyzing the outcomes from the segmentation process for both slices, from case 1 (Figure 39Figure 40.b and Figure 39Figure 40.d) and case 3 (Figure 40.b and Figure 40.d), it can be concluded that both pre-processing workflows produced a satisfactory segmentation, thus achieving an accurate discrimination of both different stains, hematoxylin and eosin, in the tissues. The fact that both automatic pre-processing techniques demonstrated consistency in datasets with large morphological and color differences (case 1, case 2 and 3), reinforces their quality, and thus their automatic color contrast enhancing capability. Comparing both methods, it is noticeable a higher differentiation between distinct stains (Hematoxylin and Eosin) with the CLAHE-red approach, being the correspondent tissues accurately separated, even in the collision tumor where both cell lines were clearly identified. On the other hand, the YCbCr workflow produced a tissue differentiation in the collision tumor in case 1 and divided different tissues near the inner neoplasic tissue in the case 3 image.

During the pre-processing technique's development and testing, they presented several intra an inter-case inconsistencies in terms of contrast enhancement efficiency (visible when comparing Figure 36, Figure 40 and Figure 39) and, therefore, in the final segmentation accuracy. These errors are mainly due to staining incongruities in slices from different datasets and even from slices of the same case study, a fact already mentioned in section 3.1.2., presenting, in the last scenario, identical structures with slightly different colors. Since these pre-processing techniques rely on pixel intensity and color properties and have to be automatic, the aforementioned fact is the most probable cause for some errors in the segmentation.

Despite some techniques, and respective results, being explored and described to mask blood vessels from the images, namely, CIE L*a*b and normalization techniques, after several trials, intense testing and combination of techniques, the development of an automatic method capable of performing accurate distinction of blood vessels, in all images contained in the three datasets was proven impossible. In some cases, only the exterior blood vessels were removed, in other cases occurred a partial removal on the same. Facing this fact, the regions containing blood vessels in the images were not removed with the developed mask technique, implemented in the final pre-processing workflow.

CLAHE-red histogram equalization with background removal (masking process) and the YCbCr color space, also with background removal, preceded by a normalization step, both top performing methods in the segmentation process, were implemented to all slices from the three image datasets, in order to improve image registration, a process exhaustively explored in the next section.

4.2. Registration stage

In the present section, the registration methods, or combination of methods, are going to be explored and their efficiency in slice alignment will be compared, based on the DICE score and the computational cost required to compute the entire dataset image registration. The computational cost was measured as the time required to complete the registration of all the slices. The dataset selected to test the registration methods was case 3, containing 100 slices, since it is the complete dataset with the lowest number of images. All the experiments, using different registration algorithms were conducted for reference slice and pairwise registration models (section 3.2.2.). All the images submitted to a registration method suffered a previous grayscale conversion followed by a contrast adjustment with (MathWorks).

The first method explored was the **automatic - intensity based** technique, due to its simplicity and its three types of transformation (rigid, similarity and affine). The best suited pre-processed image to perform registration, among the resultant from the pre-processing methods, described in the previous section, was determined for this first test and used for the other intensity-based methods (Demon and B-spline algorithms). The mean DICE score, average DICE score from the 100 registered slices, measured to assess the registration quality, and the time elapsed during the registration of the entire dataset are presented in Table II, for all the experiments conducted.

Table II. Table containing the mean DICE scores and the elapsed times for the intensity-based registration implementation, with different types of transformation (rigid, similarity and affine) and models (reference slice, pairwise), on images from both top-performing pre-processing methods (YCbCr color transformation and CLAHE-red).

Pre-processing method	**Transformation**	**Intensity- based registration**	
		Reference Slice	Pairwise
YCbCr color space transformation	With Mask Rigid	DICE: 0.6632±0.1739 Time: 54.808968 s	DICE: 0.6425±0.2612 Time: 53.710495 s
	Without Mask Rigid	DICE: 0.9114±0.0288 Time: 66.556130 s	DICE: 0.8897±0.0411 Time: 66.166884 s
	Similarity	DICE: 0.9033±0.0642 Time: 81.728404 s	DICE: 0.8906±0.0422 Time: 72.233815 s
	Affine	DICE: 0.9054±0.0626 Time: 74.174649 s	DICE: 0.8897±0.0432 Time: 67.782040 s
CLAHE-red	Without Mask Rigid	DICE: 0.9683±0.0283 Time: 55.990489 s	DICE: 0.9419±0.0385 Time: 47.265646 s

Firstly, the images resulting from the YCbCr color space transformation (the method was applied to all slices in the dataset) masked and unmasked were tested with rigid transformation, to assess if the background removal would improve the registration process, as it did with the segmentation (section 4.1.). Comparing the DICE scores it is clear that without masking process the registration is considerably more accurate (Masked DICE = 0.6632±0.1739; Without mask DICE = 0.9114±0.0288; for reference slice model), although with a higher computational cost. These results prove not only that the masking method implemented is irregular in terms of removed structures, but also that a masked image possesses far lesser information, for an intensity-based registration method, than the same image with background. Considering the discrepancy between the obtained DICE scores, the following experiments were all conducted without masked images, to comprehend which one of the registration types performs the best registration considering the available datasets. Comparing the higher rigid score with both similarity and affine DICE scores it is possible to deduce that when the reference model is performed the rigid transformation slightly outperforms the other two types when the model is the reference slice (rigid DICE = 0.9114±0.0288; similarity DICE = 0.9033±0.0642; affine DICE = 0.9054±0.0626), and, when implementing the pairwise framework the three scores are similar (rigid DICE = 0.8897±0.0411; similarity DICE = 0.8906±0.0422; affine DICE = 0.8897±0.0432), with slightly higher DICE result for the similarity type. After this test, the set of YCbCr images was substituted by the resulting images from the CLAHE-red method to verify which pre-processing technique produces the best images for intensity-based registration. This test was conducted without background removal and to the top scoring registration type – rigid registration. The comparison between the DICE scores indicates that the best pre-processing method, for the considered dataset intensity-based image registration is the CLAHE-red (for reference slice model CLAHE rigid DICE = 0.9683±0.0283, YCbCr rigid DICE = 0.9114±0.0288; for pairwise model CLAHE rigid DICE = 0.9419±0.0385, YCbCr rigid DICE = 0.8897±0.0411). All the tests performed with reference slice model consistently present a higher DICE score when confronted with their pairwise model counterparts, suggesting that, for this case 3 the best model to perform intensity-based registration, and therefore, the entire image dataset alignment is the registration of each image to the reference slice. In the present work the defined reference slice is the middle one (slice nº50 in the considered dataset – case 3), because it is the most representative in terms of tissues, according to (Chakravarty, Bedell et al. 2008)).

Analyzing the computing time of all the different registration types the results (Table II), it can be observed that the rigid transformation is the less computationally expensive, followed by the affine and then the similarity transform, with the highest time. These results go according to expected, because the rigid transform consists only in translation and rotation, being simpler than the other two (similarity – translation, rotation and scale; affine – translation, rotation, scale and sheer). Comparing, on the other hand, the times obtained by both registration models, it is visible a consistent increased computational cost in the registration methods performed using reference slice.

Alignment images and pair of fixed and moving image for the most relevant registration experiments are shown in Figure 42, Figure 42 and Figure 43. The chosen moving image is slice nº35, the same as in the pre-processing section (4.1.).

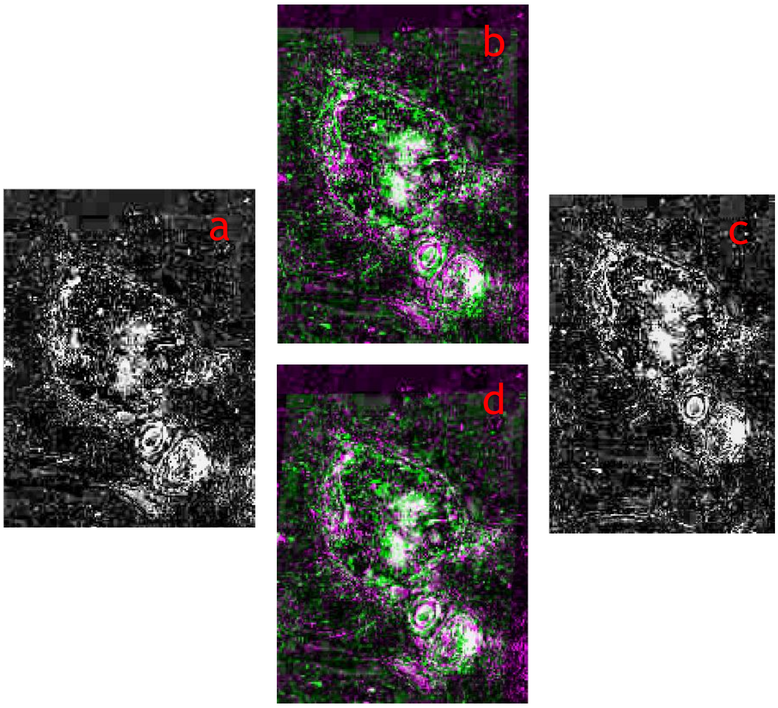

Figure 41. Images representing intensity-based image registration performed with reference slice model and two types of transformation, from YCbCr pre-processing. Image (a) represents the fixed image (slice nº50) and (c) the moving image (slice nº35) for both rigid (b) and affine (d) registration type overlapping image (Fixed and registered images).

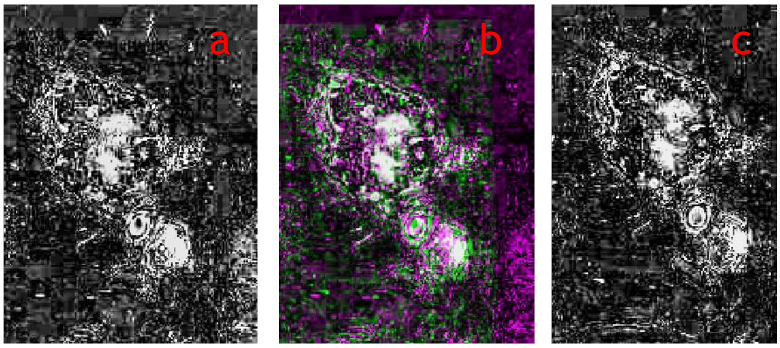

Figure 42. Images representing intensity-based image registration pairwise model and rigid transformation type, from YCbCr pre-processing. Image (a) represents the fixed image (slice nº36), (c) the moving image (slice nº35) and (b) the rigid registration overlapping image (Fixed and registered images).

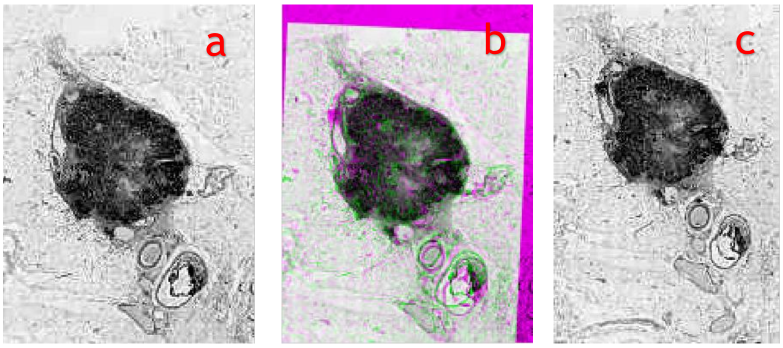

Figure 43. Images representing intensity-based image registration performed with reference slice model and rigid transformation type, from CLAHE-red pre-processing. Image (a) represents the fixed image (slice n°50), (c) the moving image (slice n°35) and (b) the rigid registration overlapping image (Fixed and registered images).

After experimenting the automatic intensity-based registration algorithm, explained in section 3.2.2., an automatic **feature-based similarity registration** approach was implemented through an algorithm also referred in this section. Based on the top-scoring results obtained with the first method, the feature-based technique was applied to the CLAHE-red processed images, but without any viable results. This was due to the lack of matching points verified in the registration process of most of the slices contained in the dataset, either recurring to reference slice or pairwise model. Taking this into account and that feature-based methods perform image alignment based on features correspondence (between moving and fixed images), such as points, lines and contours, another pre-processing technique was applied to the dataset images, the image normalization (section3.2.1.). This method was implemented due to its capability to detach the lymph node (in this case) from the background, promoting its contour extraction. Aiming also to improve the contour extraction for the feature registration method a gaussian smoothing filter, with kernel dimensions 4x4, was applied to the normalized image. The registration results, DICE mean score and computational time, for smoothed and non-smoothed images are presented in Table III. The reference slice registration model was tested for this set of images, but it was incapable of providing a full dataset registration, and thus, the DICE score was not measured.

Table III. Table containing the mean DICE scores and the elapsed times for the feature-based registration implementation with pairwise model on images with both smoothed and non-smoothed image normalization pre-processing.

Pre-processing method		Feature-based similarity registration (Pairwise model)
Image Normalization	With smoothing	DICE score: 0.9218±0.0481 Time: 30.537524 s
	Without smoothing	DICE score: 0.8412± 0.0999 Time: 27.915660 s

Observing the mean DICE scores obtained for smoothed images registration as opposed to non-smoothed (Table III), the superiority in terms of accuracy is substantial for the smoothed version, as expected. Only the pairwise model was successful in the similarity feature-based registration. Regarding the computational cost, both methods present similar times, around 30 seconds, considerably shorter than those obtained through intensity-based registration. An example of smoothed slices alignment, including the correspondent fixed and moving pair (Moving - slice nº 35; Fixed – slice nº36) is shown in Figure 44.

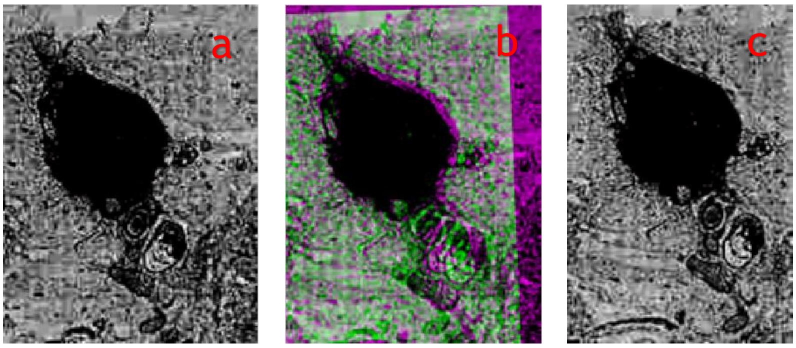

Figure 44. Images representing intensity-based image registration performed with pairwise model and similarity transformation type, from smoothed image normalization pre-processing. Image (a) represents the fixed image (slice nº36), (c) the moving image (slice nº35) and (b) the rigid registration overlapping image (Fixed and registered images).

Analyzing Table II and Table III top performing pre-processing and registration frameworks it is possible to infer that the intensity-based method performs the best image alignment (Intensity - CLAHE-red rigid DICE: 0.9683±0.0283; Smooth Normalization Similarity DICE: 0.9218±0.0481). Considering, in turn, the time elapsed during the registration procedure the intensity method almost doubles the computational cost (Intensity: 55.990489 s; Feature: 30.537524 s). Considering also that only a specific registration model and pre-processing method accomplished a satisfactory result, it is clear that the intensity-based registration is more adequate to perform slice alignment for the tested dataset. This result is expected due to fact that the images contained in the case 3, and H & E histological images in general, contain more information in image intensities, due to the color stains, than image features, identifiable by feature-based registration techniques.

With the intensity-based registration, using rigid transformation, being proved the best approach for these type of datasets, another experiment was conducted through the implementation of two distinct non-rigid registration techniques, the Demon and the B-spline algorithms (complex methods described with detail in section 3.2.2.).

Table IV. Table containing the mean DICE scores and the elapsed times for the intensity-based non-rigid registration implementation, with two different algorithms (B-spline and Demon) and models (reference slice, pairwise), on images obtained from CLAHE-red pre-processing method.

Quality parameters	B-Spline		Demon Algorithm	
	Reference	Pairwise	Reference	Pairwise
DICE mean Score	0.9932±0.0013	0.9916±0.0056	0.9279±0.0352	0.9297±0.0438
Time	53 min (approx.)	54 min* (approx.)	40 min* (approx.)	28 min* (approx.)

*The entire dataset registration (100 images) was not accomplished by this algorithm/model.

An example of registration using B-spline and another using the Demon algorithm are presented in Figure 45. The results obtained for Demon algorithm with reference slice registration model and with pairwise model were similar, with the same mean DICE scores and a small difference in the standard deviation. The lower standard deviation for the first model suggests that the reference model originated a slightly more consistent registration for the entire image dataset. Through elapsed time comparison the pairwise registration model is the most efficient mode, when using the Demon algorithm on this dataset. Despite this apparent advantage, since it was not capable of performing the registration on the 100 slices of case 3, and only in 82, the best registration model is undoubtedly the reference slice model, even without registering the final slice. Analyzing the B-spline results it is easily concluded that this method obtained the highest DICE scores of all the tested methods before, in both registration models. Although the best performing method, the computational costs required to perform the complete dataset registration (100 images) with this algorithm, are untenably extensive, reaching almost an hour and even more, considering that, with the pairwise model only 82 slices were registered. Consulting some of the produced alignments, with the B-spline method, it is possible to observe several moving images completely distorted to fit the fixed image. This is one of the main reasons that justifies the outstanding DICE score verified by the B-spline method, an error that erases fundamental morphological tissue information present in the slices. Therefore, when compared to the Demon algorithm, this method is more limited, not only due to the longer computation times but also the greater distortion applied to the images. An illustrative image of the referred distortion error is visible in Figure 46, an alignment resultant from the B-spline non-rigid method.

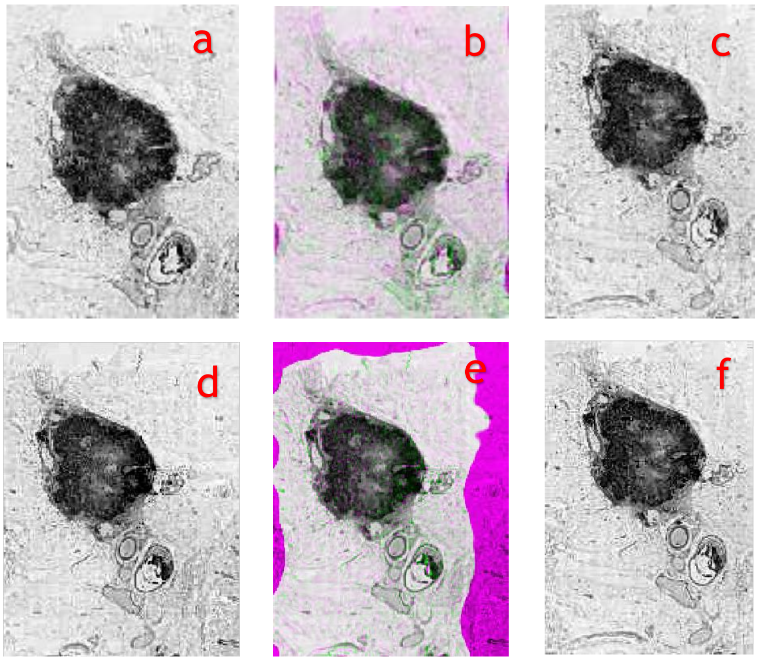

Figure 45. Images representing the intensity-based non-rigid registration. On the first set of three images was performed the B-spline algorithm with reference model, fixed image (a) is slice n°50, moving image (c) is slice n°35 and (b) the non-rigid registration overlapping image (Fixed and registered image). Concerning the other three images, (d) is the fixed image (n°36) and (f) the moving image (n°35) and (e) the overlapping image obtained with Demon algorithm in pairwise model.

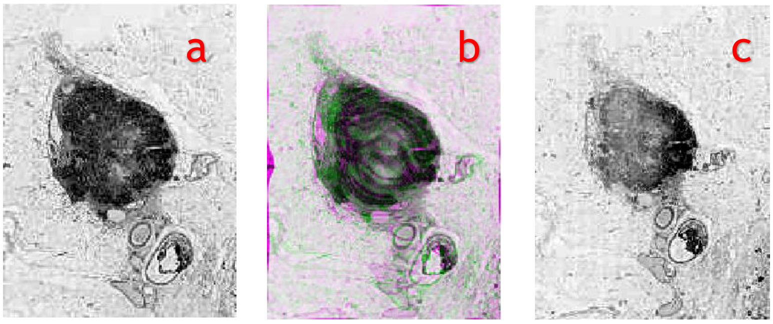

Figure 46. Illustrative images presenting a distortion error in the registration. Image (a) is the fixed slice (n°50), image (c) is the moving slice (n°40) and (b) is the overlapped image obtained with B-spline algorithm, in reference slice model.

After exploring the non-rigid registration algorithms and following a previously developed methodology, performed by (Roberts, Magee et al. 2012), both the top-performing intensity-based rigid and non-rigid registration techniques were combined, with the purpose of obtaining a more consistent framework to align histological sections with no distortions, and also to verify if by using previous rigidly registered images as input of a non-rigid method it increases the computational speed of the last process. The results obtained by the implementation of this method are - DICE: 0.9573±0.0340; Time: 40 min (approx.) –when applying the Demon algorithm after the rigid intensity-based registration, both in reference slice model, and – DICE: 0.9655± 0.0417; Time: 25 min (approx.) – using the same framework but with both methods in pairwise registration model. Comparing both scores, the pairwise model presented a faster and more reliable approach than its reference slice counterpart. Although the consistent results from both frameworks, when compared to the rigid intensity-based registration performed using middle reference slice model (Table II), it is easily concluded that the rigid method presents itself the most efficient registration approach, with higher DICE scores and requiring far less time to compute all the transformations in the dataset. Therefore, it can be deduced that the combination of this method with a posterior non-rigid algorithm did not increase the accuracy in the registration, and, facing this, the best method is the automatic intensity-based rigid registration, the first method tested.

In order to validate the intensity rigid registration method, combined with CLAHE-red image pre-processing as a general framework to apply image alignment in large datasets of histological slices stained with H & E, it was applied in both case 1 and 2, and the results can be found in Table V.

Table V. Table containing the mean DICE scores and the elapsed times for the intensity-based rigid registration method implementation, on two different image datasets (Case 1 and 2), previously pre-processed by CLAHE-red algorithm.

	Case 1	**Case 2**
Intensity rigid registration	DICE: 0.9267±0.0337 Time: 21 min (approx.)	DICE: 0.9367±0.0356 Time: 47.242910 s

An example of the registration of one moving slice (n°35) to the reference fixed (middle slice), for both cases 1 and 2, is presented in Figure 47. The DICE scores obtained for both datasets, despite being lower than the obtained for case 3 (DICE: 0.9683±0.0283), are satisfactory results, revealing a consistent alignment of the entire dataset above 0.9 score (in both cases). Comparing, in turn, the time elapsed in the registration of each case, the case 1 is the most demanding in terms of computational cost, taking 21 minutes to completion. In contrast, case 2 took the least amount of time to perform the entire registration of the dataset, with approximately 47 seconds, followed by case 3 with 56 seconds (approx.). This time discrepancy, verified between case 1 and the other two, is due to the fact that besides being composed by more images (case 1 – 124; case 2 – 94; case 3 – 100), this dataset is composed by larger images, and consequently more pixels to be analyzed in the registration process.

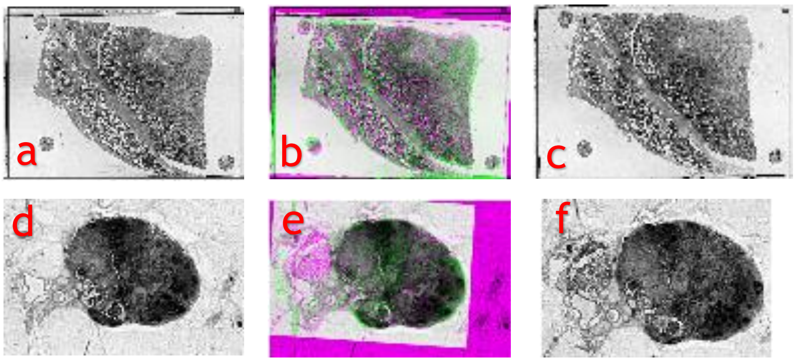

Figure 47. Images representing intensity-based image registration performed with reference slice model and rigid transformation type, from CLAHE-red pre-processing. Image (a) represents the fixed image (slice nº50), (c) the moving image (slice nº35) and (b) the rigid registration overlapping image for case 1 dataset. Image (d), (f) and (e) represent equivalent images but concerning case 2.

4.3. Final Results

In this section, the results from the final workflow developed, aiming the 3D final reconstruction, including previous pre-processing, segmentation and registration are thoroughly described. All the figures resultant from the different steps are presented for slice nº 35, as in previous sections, to exemplify a possible outcome.

The first step is the pre-processing implementation, and, as consistently proved throughout sections 4.1. and 4.2. the most successful method to discriminate hematoxylin and eosin stained tissues in H & E histological images is the CLAHE-red algorithm. Since the processed images were going to be subjected to image segmentation, in the following step, and considering that masking the background increases the segmentation accuracy, as concluded in section 4.1., but reduces the registration capability, in the registration step (after segmentation), as inferred in the previous section, a different background removal method was implemented. This method involves the YCbCr color space transformation (section 3.2.2.), but instead reducing the luminance in images, as performed in section 4.1., this channel was enhanced in 1.2x (multiplication factor determined by trial and error to optimize the stain deconvolution's accuracy), increasing pixel intensities, which eliminates most of the background details. Then, the CLAHE-red is applied to the RGB image enhanced in the YCbCr color space, and an example result, for all the available datasets, can be observed in Figure 48. A comparison with Figure 29 reveals that, the added luminance enhancement step does not reduces the color contrast between different stains, achieved implementing only CLAHE-red.

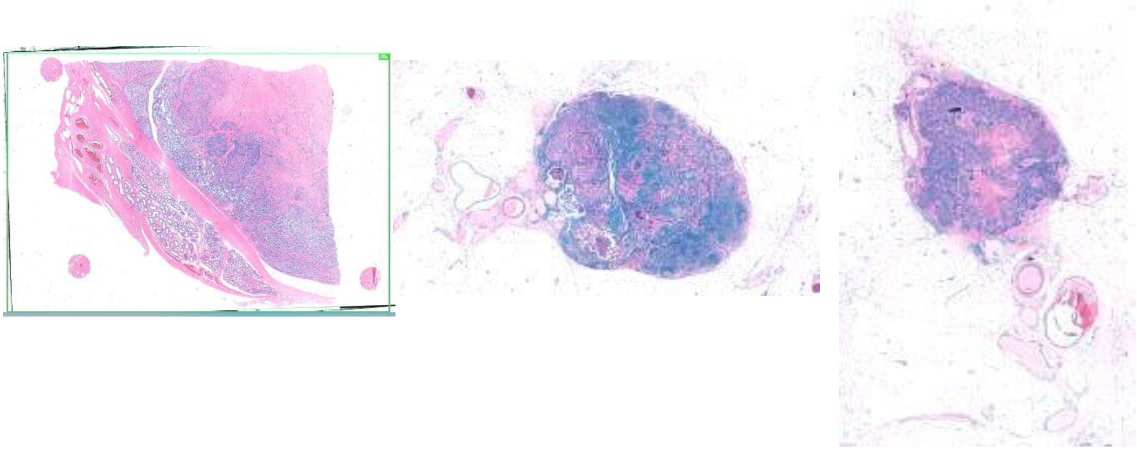

Figure 48. Images obtained from the combined pre-processing framework YCbCr luminance enhancement and CLAHE-red applied to the original images. Image (a) belongs to case 1, image (b) to case 2 and (c) to the third dataset.

After the pre-processing stage, all the slices were submitted to a segmentation process, performed with the stain deconvolution algorithm (described with detail in section 3.2.3.), developed for this study. The stain deconvolution was performed for 3 class, in order to discriminate hematoxylin stained tissues, eosin stained tissues and the background. The segmentation result, as well as the Eosin and Hematoxylin extracted images are presented in Figure 49. Comparing the eosin and hematoxylin stain images obtained with this algorithm with CLAHE-red pre-processed images, it can be concluded that both grayscale stain images produced present an accurate representation of the correspondent stained tissue in the CLAHE-red image, as regions with higher intensity.

By performing this technique two grayscale images are generated, the hematoxylin and eosin tissue images, that are used in the following process as image to be registered (only one of them is used to find the transformation), avoiding this way the implementation of grayscale conversion on RGB images to pursue the slice alignment. The pre-processing and segmentation framework, described so far, is also applied to the reference slice (nº50).

The registration was performed following the top performing method, the intensity-based rigid registration technique applied using hematoxylin or eosin grayscale images, obtained with the stain deconvolution algorithm from each slice in the dataset. The DICE score and computational cost were measured for the registration process applied to both hematoxylin and eosin images and the obtained values for each dataset are presented in Table VI. An example of the registration process for slice nº35 of case 3, with hematoxylin image can be observed in Figure 50.

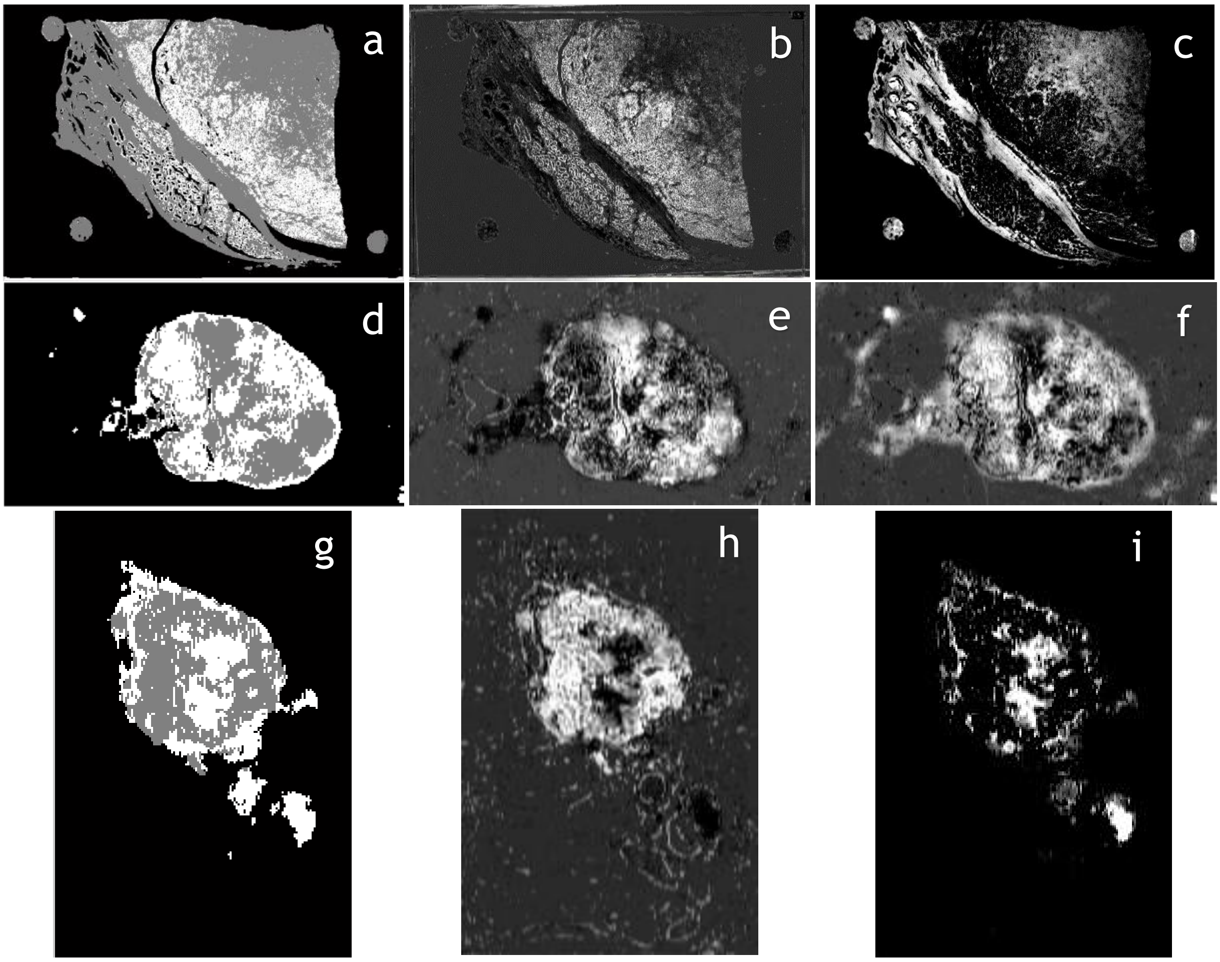

Figure 49. Segmentation results obtained with the stain deconvolution algorithm (first column): case 1-(a), 2-(d) and 3 (g). Hematoxylin image extracted with this algorithm (second column): case 1-(b), 2-(e) and 3-(h). Eosin image extracted (third column): case 1-(c), 2-(f) and 3-(i).

Analyzing Table VI it was possible to conclude which of the stain deconvolution outcome images is the most suited to perform image registration. The highest mean DICE scores verified belong to registrations performed with hematoxylin images, in all three datasets, justified by its greater representativeness in terms of high intensity structures, as it can be visualized in Figure 49. In case 2 both images, hematoxylin and eosin, share similar structures, with high pixel intensity, a fact, corroborated by the closest proximity in the DICE scores measured. In terms of computational time, the less demanding are the dataset registrations performed with the eosin images, because of the same reason explained for the DICE score, less amount of pixels to be correlated in the procedure. It is also noticeable that, for case 1 the registration was not only computationally expensive but also inaccurate and inconsistent (high standard deviation values), with mean DICE scores below those verified in for CLAHE-red (Table V), suggesting that the stain deconvolution proved itself incapable to distinguish both tissue stains in a substantial portion of slices, from this dataset.

Table VI. Table containing the mean DICE scores and the elapsed times for the intensity-based rigid registration method implementation, on all the image datasets (Case 1, 2 and 3), considering two different grayscale images (hematoxylin and eosin images), obtained through pre-processing (CLAHE-red and YCbCr transformation) and segmentation (stain deconvolution algorithm).

Case study	**Registration**	
	Hematoxylin image	Eosin image
1	DICE: 0.8387±0.2785 Time: 71 min (approx.)	DICE: 9.4781e-04±0.0102 Time: 70 min (approx.)
2	DICE: 0.9345±0.0368 Time: 204.695529 s	DICE: 0.9179±0.0610 Time: 155.079913 s
3	DICE: 0.9676±0.0296 Time: 183.110440 s	DICE: 0.6152±0.0894 Time: 158.491751 s

Considering the previous results the selected set of grayscale images chosen to find the registration transformation were the hematoxylin stain images. The transformation found on each slice registration with the reference was applied to the correspondent eosin image, being aligned with the same translation and rotation than the hematoxylin image. Hereupon, both grayscale image datasets (hematoxylin and eosin) were equally aligned, and this framework was performed for each case study.

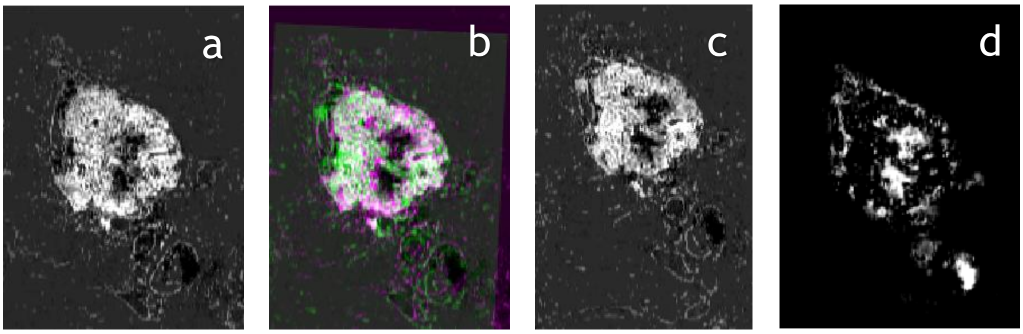

Figure 50. Images representing intensity-based image registration performed with reference slice model and rigid transformation type, from hematoxylin images obtained through stain deconvolution (Case 3). Image (a) represents the fixed image (slice n°50), (c) the moving image (slice n°35), (b) the registration overlapping image and (d) the transformed eosin stained slice (n°35), with the registration transformation determined for the hematoxylin images.

After registering the complete image dataset to the reference slice, all images were stacked creating volume data, in which the z coordinate represents the slice number. All the image datasets (case 1, 2 and 3) were stacked in two rectangular prisms each, one for the hematoxylin and the other for eosin registered images, with length and width defined by the length and width of the reference slice (because the registered image acquires the size of the fixed image), and with height equal to the number of slices contained in the dataset. These final volumes were smoothed with a box filter (a spatial domain low-pass filter in which each point in the output is the average of the surrounding points in the input structure), with 5x5 kernel, and served as input for both 3D surface reconstruction methods, the Marching Cubes algorithm and the isosurface framework from (MathWorks) described in section 3.2.3. Using the marching cubes algorithm it was only possible the reconstruction of one stained surface at the time, being represented in Figure 51 the hematoxylin and eosin reconstructions from case 3 image dataset, with isovalue equal to 0.5 for hematoxylin stack and 0.65 for eosin. Both isovalues were determined through experimentation, aiming to reconstruct a complete 3D surface for the considered tissue (stained with hematoxylin or eosin) and at the same time reduce the noise produced by background artifacts with intensities similar to the reconstructed structure, thus, reducing its intelligibility to the observer.

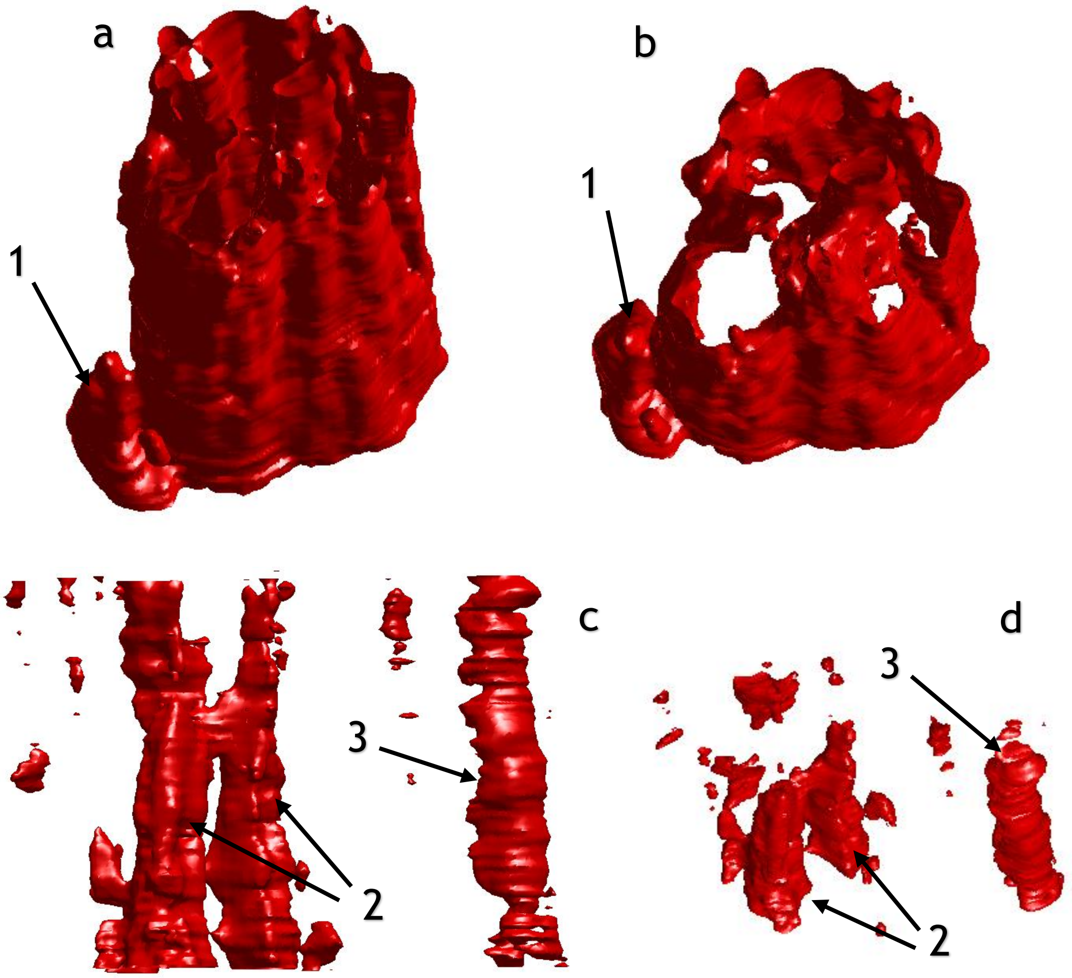

Figure 51. 3D surface reconstruction from case 3 registered image dataset, using Marching cubes algorithm. Images (a) and (b) are from hematoxylin image dataset surface reconstruction with different views. Images (c) and (d) are eosin stacked images' surface reconstruction. Structure (1) represents the neoplasic tissue found in Figure 20 – A; structure (2) represents the neoplasic tissue marked in Figure 20 – B and structure (3) is the blood vessel in Figure 20 – C.

Implementing the isosurface framework it was possible to combine both tissue stains stacks' surface reconstruction in one image, using the patch function (MathWorks), and the result obtained for case 2 and 3 can be consulted in Figure 52. To each tissue stain reconstruction was assigned a color, based on the real color presented in the original image dataset. This was accomplished using an auxiliary algorithm, which, first, separates both stains from the CLAHE-red image based on stain deconvolution segmentation, performs an average pixel intensity measurement in the three color channels of both stain images from the slice and then, after the dataset complete analysis, performs another average calculation for all the slices, obtaining two final RGB triplets to be applied to the respective stained tissue 3D reconstruction. For this method were applied two different isovalues, 0.5 and 0.65 (same as in the previous method) for hematoxylin and eosin stacks, respectively.

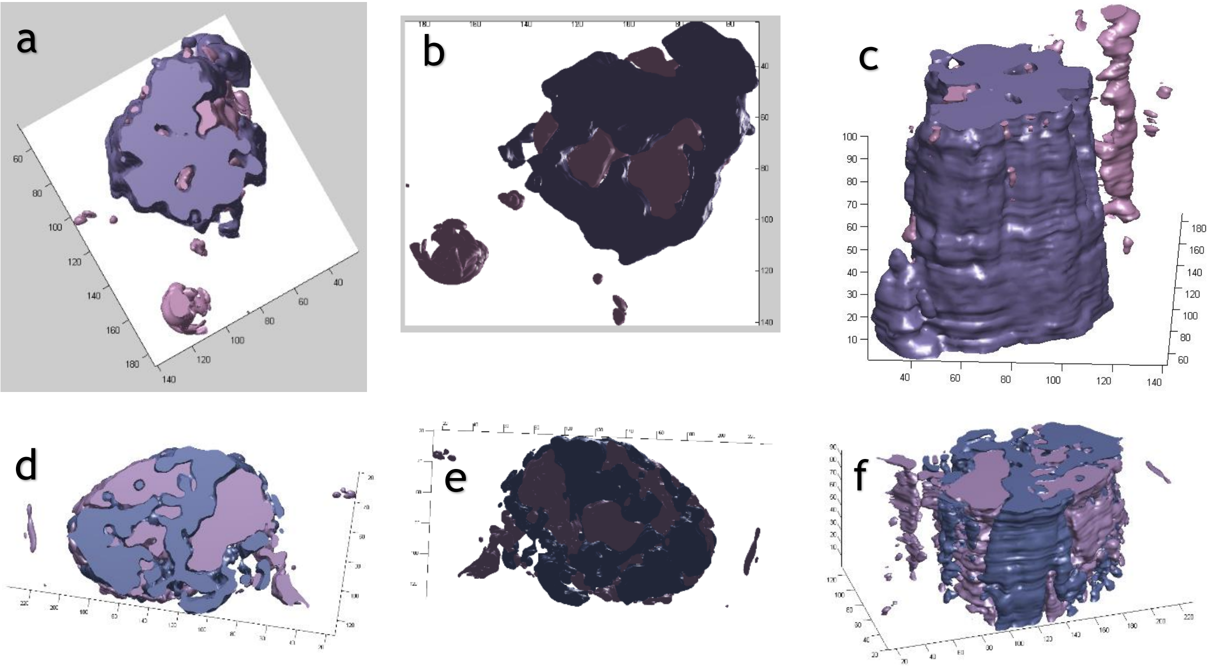

Figure 52. 3D surface reconstruction from case 2 (second line) and 3 (first line) registered image dataset, using isosurfaces framework. Image (a)-top view, (b)-bottom view and (c)-side view, represent the case 3 volumetric data combining both hematoxylin and eosin isosurfaces in three different views. Image (d)-top view, (e)-bottom view and (f)-side view, represent the case 2 volumetric data combining both hematoxylin and eosin isosurfaces in three different views.

Observing Figure 51 and Figure 52, it is possible to conclude that both cases 2 and 3 present a consistent slice alignment, visible in the surface uniformity along the Z-axis. This is more evident in the marching cubes algorithm results, suggesting that the 3D interpolation performed by this method provides more accurate results. The success of the entire framework is proven not only by this feature, but also by the similarity, in terms of morphology between what is seen in the original 2D image slices, from both datasets, and the result of the 3D surface reconstruction. Focusing on Figure 51 and in case 3 tissue analysis (section 3.1.2.) the resemblances are obvious, therefore, enabling the correlation between some relevant structures identified in Figure 20. The most evident structures reconstructed are the neoplasic tissue stained with hematoxylin (Figure 51.a – 1) and the other two stained with eosin (Figure 51.d – 2), and also the blood vessel (Figure 51.c – 3 and Figure 20 – c). These 3D surface reconstructions are consistent and are able to provide important volumetric information about histological slices contained in the datasets, converting a planar observation in a 3D visualization of the tissues stained with hematoxylin and eosin in an either separate or merged version. Analyzing the surface reconstruction performed for case 2 (Figure 52– d,e,f), it is verified a reduced eosin tissue definition, maybe due to the sparse nature of the tissue on the original dataset that decreases the intelligibility of the volumetric data. The colors expressed in the final surface reconstructions present high affinity with the stain colors verified in the CLAHE-red images in Figure 29, pointing the efficiency of the previously described color algorithm in combination with the isosurface framework.

The 3D surface reconstruction framework applied to case 1 presented some computational issues, which compromised the result demonstration. The processing power used to test all the frameworks in this study (Intel Core i7-4700HQ CPU at 2.40 GHz, with 8 GB of RAM on a Windows 64bit system) was not sufficient to load and visualize the volumetric data, mainly due to the bad performance of the stain deconvolution method in discriminating tissue stains in most slices contained in the dataset and the large image dimensions.

Taking into account all the previous 3D surface reconstructions, resulting from the final framework developed for this study, it can be concluded that the three-dimensional representation of the datasets was accomplished for the majority of the available datasets, and with interesting and reliable results. Especially for case 3, the reconstruction was able to provide accurate 3D volumetric features from neoplasic tissues in addition to overall morphological characteristics of the lymph node. The most relevant are the three dimensional progression on the Z-axis of the lesion over other tissues (Figure 51), difficult to visually estimate from a set of 2D slices.

4.4. Summary

In summary, the top performing pre-processing workflows for hematoxylin and eosin stain contrast enhancement were the CLAHE-red histogram equalization followed by a background removal (masking process) and the YCbCr color space, also with background removal, preceded by a normalization step.

After testing several methods, it was concluded that the most efficient framework to perform registration in the considered histological image datasets is the automatic intensity-based registration with rigid transformation type and reference slice model on CLAHE-red pre-processed slices. This was deduced based on both DICE score results and computational cost, being the method with lower times of execution and the second highest DICE scores. The highest score was obtained with B-spline non-rigid algorithm, but, since this method originated distortion artifacts to provide accurate registrations, corrupting valuable tissue information, and the times required to compute entire datasets could reach approximately one hour, the rigid method was considered the most suited for the task.

Combining the best methods from both pre-processing and registration sections, the final workflow was completed with the 3D surface reconstruction of both hematoxylin and eosin stained tissues registered stack. The eosin and hematoxylin separate images were acquired from an intermediate segmentation step, the stain deconvolution algorithm, a specially developed method for stained tissues differentiation from histological images. Through the combined implementation of these four main steps an accurate and interesting volumetric representation of both hematoxylin and eosin stained tissues was determined. Both 3D surfaces can be shown together or in separate images.

Chapter 5

Conclusion

Automated techniques for image processing and analysis applied to histological studies constitute an important asset in the comprehension and assessment of relevant aspects, volumetric data and models from numerous diseases, unobtainable through 2D tissue slice analysis. Impelled by the relevance of this studies and the urge to assist the histopathologists in performing medical diagnostic, more accurate and reliable algorithms have been developed, providing a fast and trustworthy second opinion.

The present study explores histological concepts, including tissue types and sample preparation as well as successful techniques of image processing and analysis, highlighting current reliable approaches in the field of 3D histological tissue reconstruction.

With the previous research in mind and considering the need to produce a 3D reconstruction approach for cellular tissue analysis, in this work it was developed an automated computational framework combining the best algorithms and techniques implemented by the reviewed approaches, focused not only on reconstructing the relevant tissues, but also on their spatial relation with the surrounding structures.

After conducting the present study, it is possible to conclude that several artifacts present in histological tissue sections, such as differences in stain colors between slices and/or image datasets, can reduce the consistency of both image processing and registration methods when applied to them. On the other hand, through the implementation of accurate registration techniques on the image datasets, the presence of tissue orientation dissimilarities, due to the manual nature inherent to the sample preparation process, was almost mitigated.

The color contrast enhancing pre-processing methods developed and applied to the original digital images effectively provided an improvement in discriminating different stained tissues. This can be inferred either from visual analysis of resulting images or from the stain deconvolution segmentation result's accuracy, and, consequently high performance in the registration process, with DICE scores of 0.9345 ± 0.0368 for case 2 and 0.9676 ± 0.0296 for case

3. Case 1 achieved poorer results in general, with a final DICE score of 0.8387±0.2785 in the registration process, justified by an inconsistent stain deconvolution procedure, revealing itself insufficient to accurately separate both stains, in a great portion of images from this dataset.

A consistent neoplasic tissue discrimination was not obtained through the implemented algorithm, but, by observing the 3D surface reconstruction of both eosin and hematoxylin (section 4.3.) the presence of this tissue is evident. Despite being specified the lesions in section 3.1.2. as tissues to be targeted by the algorithm, aiming to promote an isolated 3D reconstruction of these neoplasic tissues, the stained tissue separation and posterior 3D reconstruction reveals the interaction between the neoplasia and the surrounding healthy tissues. Therefore, the consistent reconstruction of both stained tissues including the lesion, with accurate volumetric shape, constitutes relevant information for diagnostic purpose.

Considering all this, it is concluded that the algorithm developed in this study provides a fast and accurate 3D surface volume, comprising both distinct stains represented independently and showing the three dimensional relation between lesions and the surrounding tissue. The proposed framework obtained a satisfactory performance for two of the three available datasets.

5.1. Future Work Perspectives

One future work improvement is the preparation and testing of more histological image datasets to further validate the developed algorithm, and also to assess the algorithm’s accuracy when analyzing tissues without H & E stain. This would also instigate a refinement in the computational techniques, adapting the automatic framework to more sets of images and develop a more universal algorithm, capable of performing detailed tissue 3D reconstruction of any histological section.

Another future improvement would be the incorporation of a functional and general lesion detector, able to distinguish special tissues from the other stained healthy ones. The improvement of the stain deconvolution method, implementing supervised classification of the stained tissues, using as training set a portion of the entire image dataset, could lead to more accurate staining discrimination and possibly to define other interesting tissues, such as neoplasic tissues.

An interesting future development would be the implementation of the produced computational framework in opencv (Open Source Computer Vision), enabling a faster image processing, for larger image datasets, such as case 1, and the creation of an intuitive user interface for input image dataset manipulation and 3D reconstructed volume observation.

References

Arganda-Carreras, I., R. Fernandez-Gonzalez and C. Ortiz-de-Solorzano (2004). Automatic registration of serial mammary gland sections. Engineering in Medicine and Biology Society, 2004. IEMBS'04. 26th Annual International Conference of the IEEE, IEEE.

Aubert, G. and P. Kornprobst (2006). Mathematical problems in image processing: partial differential equations and the calculus of variations, Springer Science & Business Media.

Bautista, P. A. and Y. Yagi (2010). "Improving the visualization and detection of tissue folds in whole slide images through color enhancement." Journal of pathology informatics 1: 1-25.

Bay, H., A. Ess, T. Tuytelaars and L. Van Gool (2008). "Speeded-up robust features (SURF)." Computer vision and image understanding 110(3): 346-359.

Beare, R. and G. Lehmann (2006). "The watershed transform in ITK-discussion and new developments." Insight J: 1-24.

Bengtsson, E. (2003). Computerized cell image analysis: Past, present, and future. Image Analysis, Springer: 395-407.

Blake, C. A., H. A. Lavoie and C. F. Millette (2003). "Teaching medical histology at the University of South Carolina School of Medicine: transition to virtual slides and virtual microscopes." The Anatomical Record Part B: The New Anatomist 275(1): 196-206.

Bonnet, N. (2004). "Some trends in microscope image processing." Micron 35(8): 635-653.

Bookstein, F. L. (1980). "The Measurement of Biological Shape and Shape Change." Syst. Zool 29(1): 102-104.

Braumann, U.-D., J.-P. Kuska, J. Einenkel, L.-C. Horn, M. Loffler and M. Hockel (2005). "Three-dimensional reconstruction and quantification of cervical carcinoma invasion fronts from histological serial sections." Medical Imaging, IEEE Transactions on 24(10): 1286-1307.

Caicedo, J. (2009, 06 November). "Features for Histology Images." Retrieved 03 February, 2015, from http://www.informed.unal.edu.co/jccaicedo/docs / review.pdf.

Chakravarty, M. M., B. J. Bedell, S. P. Zehntner, A. C. Evans and D. L. Collins (2008). Three-dimensional reconstruction of serial histological mouse brain sections. Biomedical Imaging: From Nano to Macro, 2008. ISBI 2008. 5th IEEE International Symposium on, IEEE.

Chakravarty, M. M., G. Bertrand, C. P. Hodge, A. F. Sadikot and D. L. Collins (2006). "The creation of a brain atlas for image guided neurosurgery using serial histological data." Neuroimage 30(2): 359-376.

Chan, A. C. S. (2013, 21 July 2013). "Tumor cell extraction by color deconvolution." Retrieved 15 June, 2015, from http://web.hku.hk/~ccsigma/color-deconv/color-deconv.html.

Chaudhuri, B., K. Rodenacker and G. Burger (1988). "Characterization and featuring of histological section images." Pattern Recognition Letters 7(4): 245-252.

Cheung, R. (2012). "InSPIRE utility to calculate DICE Coefficient." Retrieved 20 June, 2015, from http://www.mathworks.com/matlabcentral/fileexchange/36322-inspire-utility-to-calculate-dice-coefficient/content/DiceSimilarity2DImage.m.

Chomphuwiset, P., D. Magee, R. Boyle and D. Treanor (2011). Context-based classification of cell nuclei and tissue regions in liver histopathology. Proc. Medical Image Understanding and Analysis.

Cisneros, F. J., P. Cordero, A. Figueroa and J. Castellanos (2011). "Histology image segmentation." International Journal of Information Technology and Management 5(1): 67-76.

Collins, D. L. and A. C. Evans (1997). "Animal: validation and applications of nonlinear registration-based segmentation." International Journal of Pattern Recognition and Artificial Intelligence 11(08): 1271-1294.

Collins, D. L., P. Neelin, T. M. Peters and A. C. Evans (1994). "Automatic 3D intersubject registration of MR volumetric data in standardized Talairach space." Journal of computer assisted tomography 18(2): 192-205.

D., B. (1978). "Three Dimensional Reconstruction in Biology." Journal of Anatomy 127.

Davatzikos, C., J. L. Prince and R. N. Bryan (1996). "Image registration based on boundary mapping." Medical Imaging, IEEE Transactions on 15(1): 112-115.

De Castro, E. and C. Morandi (1987). "Registration of translated and rotated images using finite fourier transforms." IEEE Transactions on pattern analysis and machine intelligence 9(5): 700-703.

de Ryk, J., E. Namati, J. M. Reinhardt, C. Piker, Y. Xu, L. Liu, E. A. Hoffman and G. McLennan (2004). A whole organ serial sectioning and imaging system for correlation of pathology to computer tomography. Biomedical Optics 2004, International Society for Optics and Photonics.

Della Mea, V., F. Demichelis, F. Viel, P. Dalla Palma and C. A. Beltrami (2006). "User attitudes in analyzing digital slides in a quality control test bed: A preliminary study." Computer methods and programs in biomedicine 82(2): 177-186.

Díaz Iriberri, J. (2007). "Inspección Interactiva de Estructuras Anatómicas Tubulares." Retrieved 04 February, 2015, from http://hdl.handle.net/2099.1/11297.

Dive, A. M., A. S. Bodhade, M. S. Mishra and N. Upadhyaya (2014). "Histological patterns of head and neck tumors: An insight to tumor histology." Journal of Oral and Maxillofacial Pathology 18(1): 58.

Efford, N. (2000). Digital image processing: a practical introduction using java (with CD-ROM), Addison-Wesley Longman Publishing Co., Inc.

Ford, A. and A. Roberts (1998). "Colour space conversions." Westminster University, London 1998: 1-31.

Gilbertson, J. R., J. Ho, L. Anthony, D. M. Jukic, Y. Yagi and A. V. Parwani (2006). "Primary histologic diagnosis using automated whole slide imaging: a validation study." BMC clinical pathology 6(1): 4.

Gonzalez, R. and R. Woods (2008). Digital Image Processing, Prentice Hall.

Goshtasby, A. A. (2005). 2-D and 3-D image registration: for medical, remote sensing, and industrial applications, John Wiley & Sons.

Gray, H. and H. V. Carter (2008). Gray's anatomy, Hinkler Books.

Halper, J. and M. Kjaer (2014). Basic Components of Connective Tissues and Extracellular Matrix: Elastin, Fibrillin, Fibulins, Fibrinogen, Fibronectin, Laminin, Tenascins and Thrombospondins. Progress in Heritable Soft Connective Tissue Diseases, Springer: 31-47.

Hammer, P. (2011, 11 August 2011). "Marching Cubes." Retrieved 9 June, 2015, from http://www.mathworks.com/matlabcentral/fileexchange/32506-marching-cubes.

Han, L., J. I. van Hemert and R. A. Baldock (2011). "Automatically identifying and annotating mouse embryo gene expression patterns." Bioinformatics 27(8): 1101-1107.

Hartley, R. and A. Zisserman (2003). Multiple view geometry in computer vision, Cambridge university press.

He, L., L. R. Long, S. Antani and G. Thoma (2010). "Computer assisted diagnosis in histopathology." Sequence and genome analysis: methods and applications: 271-287.

Hill, D. L., P. G. Batchelor, M. Holden and D. J. Hawkes (2001). "Medical image registration." Physics in medicine and biology 46(3): R1.

Hovanes, M. E., J. R. G. Deal and A. H. Rowberg (1999). "Seamless multiresolution display of portable wavelet-compressed images." Journal of digital imaging 12(1): 109-111.

Hukkanen, J., A. Hategan, E. Sabo and I. Tabus (2010). Segmentation of cell nuclei from histological images by ellipse fitting. The 2010 European Signal Processing Conference.

Jain, A. (1981). "Image data compression: A review." Proceedings of the IEEE 69(3): 349-389.

Johnson, H. J. and G. E. Christensen (2002). "Consistent landmark and intensity-based image registration." Medical Imaging, IEEE Transactions on 21(5): 450-461.

Junqueira, L. C. U. and J. Carneiro (1987). Histología básica, Guanabara Koogan.

Kaczmarek, E. and R. Strzelczyk (2005). "From two to three-dimensional visualisation of structures in light and confocal microscopy-applications for biomedical studies." Current issues on multidisciplinary microscopy research and education. FORMATEX microscopy book series no. II Formatex Research Centre, Badajoz: 289-295.

Kaufman, M., R. Brune, R. Baldock, J. Bard and D. Davidson (1997). "Computer-aided 3-D reconstruction of serially sectioned mouse embryos: its use in integrating anatomical organization." The International journal of developmental biology 41(2): 223-233.

Kaur, M., J. Kaur and J. Kaur (2011). "Survey of contrast enhancement techniques based on histogram equalization." IJACSA) International Journal of Advanced Computer Science and Applications 2(7).

Kierszenbaum, A. L. (2007). Histology and cell biology: an introduction to pathology, Elsevier.

Klein, C. A. (2008). "The metastasis cascade." Science 321(5897): 1785-1787.

Kley, N. J. (2006). "Morphology of the lower jaw and suspensorium in the Texas blindsnake, Leptotyphlops dulcis (Scolecophidia: Leptotyphlopidae)." Journal of morphology 267(4): 494-515.

Kong, J., O. Sertel, H. Shimada, K. L. Boyer, J. H. Saltz and M. N. Gurcan (2009). "Computer-aided evaluation of neuroblastoma on whole-slide histology images: Classifying grade of neuroblastic differentiation." Pattern Recognition 42(6): 1080-1092.

Koshi, R., S. J. Holla and G. Chandi (1997). "Introduction to histology through the use of familiar objects: innovative teaching module." Clinical Anatomy 10(5): 333-336.

Kroon, D.-J. (2008, 16 May 2011). "B-spline Grid, Image and Point based Registration." Retrieved 16 June, 2015, from http://www.mathworks.com/matlabcentral/fileexchange/20057-b-spline-grid--image-and-point-based-registration.

Kroon, D.-J. (2008, 03 Jun 2010). "Multimodality non-rigid demon algorithm image registration." Retrieved 16 June, 2015, from http://www.mathworks.com/matlabcentral/fileexchange/21451-multimodality-non-rigid-demon-algorithm-image-registration.

Kroon, D.-J. (2009, 02 November 2010). "FMINLBFGS: Fast Limited Memory Optimizer." Retrieved 16 June, 2015, from http://www.mathworks.com/matlabcentral/fileexchange/23245-fminlbfgs-fast-limited-memory-optimizer/content/fminlbfgs.m.

Kumar, R. K., G. M. Velan, S. O. Korell, M. Kandara, F. R. Dee and D. Wakefield (2004). "Virtual microscopy for learning and assessment in pathology." The Journal of pathology 204(5): 613-618.

Kurien, T., R. Boyce, E. Paish, J. Ronan, J. Maddison, E. Rakha, A. Green and I. Ellis (2005). "Three dimensional reconstruction of a human breast carcinoma using routine laboratory equipment and immunohistochemistry." Journal of clinical pathology 58(9): 968-972.

Lau, J. C., J. P. Lerch, J. G. Sled, R. M. Henkelman, A. C. Evans and B. J. Bedell (2008). "Longitudinal neuroanatomical changes determined by deformation-based morphometry in a mouse model of Alzheimer's disease." Neuroimage 42(1): 19-27.

Liu, D. C. and J. Nocedal (1989). "On the limited memory BFGS method for large scale optimization." Mathematical programming 45(1-3): 503-528.

Lorensen, W. E. and H. E. Cline (1987). Marching cubes: A high resolution 3D surface construction algorithm. ACM siggraph computer graphics, ACM.

Maes, F., A. Collignon, D. Vandermeulen, G. Marchal and P. Suetens (1997). "Multimodality image registration by maximization of mutual information." Medical Imaging, IEEE Transactions on 16(2): 187-198.

Maes, F., D. Vandermeulen and P. Suetens (1999). "Comparative evaluation of multiresolution optimization strategies for multimodality image registration by maximization of mutual information." Medical image analysis 3(4): 373-386.

Magee, D., D. Treanor and P. Quirke (2008). A new image registration algorithm with application to 3D histopathology. Proceedings of the 3 rd Medical Image Computing and Computer Assisted Intervention (MICCAI) Workshop on Microscopic Image Analysis with Applications in Biology (MIAAB). New York.

Mahalanobis, P. C. (1936). "On the generalized distance in statistics." Proceedings of the National Institute of Sciences (Calcutta) 2: 49-55.

MathWorks, R. a. "adapthisteq." Retrieved 3 June, 2015, from http://www.mathworks.com/help/images/ref/adapthisteq.html.

MathWorks, R. a. "applycform." Retrieved 3 June, 2015, from http://www.mathworks.com/help/images/ref/applycform.html.

MathWorks, R. a. "Find Image Rotation and Scale Using Automated Feature Matching." Retrieved 10 June, 2015, from http://www.mathworks.com/help/images/examples/find-image-rotation-and-scale-using-automated-feature-matching.html.

MathWorks, R. a. "hsv2rgb." Retrieved 3 June, 2015, from http://www.mathworks.com/help/matlab/ref/hsv2rgb.html.

MathWorks, R. a. "imadjust." Retrieved 12 June, 2015, from http://www.mathworks.com/help/images/ref/imadjust.html.

MathWorks, R. a. "Intensity-Based Automatic Image Registration." Retrieved 10 June, 2015, from http://www.mathworks.com/help/images/intensity-based-automatic-image-registration.html.

MathWorks, R. a. "interp3." Retrieved 10 June, 2015, from http://www.mathworks.com/help/matlab/ref/interp3.html.

MathWorks, R. a. "isosurface." Retrieved 28 May, 2015, from http://www.mathworks.com/help/matlab/ref/isosurface.html.

Mathworks, R. a. "kmeans." Retrieved 3 June, 2015, from http://www.mathworks.com/help/stats/kmeans.html.

MathWorks, R. a. "makecform." Retrieved 3 June, 2015, from http://www.mathworks.com/help/images/ref/makecform.html.

MathWorks, R. a. "Nearest Neighbor, Bilinear, and Bicubic Interpolation Methods." Retrieved 16 June, 2015, from http://www.mathworks.com/help/vision/ug/interpolation-methods.html#f13687.

MathWorks, R. a. "patch." Retrieved 10 June, 2015, from http://www.mathworks.com/help/matlab/ref/patch.html.

MathWorks, R. a. "registration.metric.MeanSquares class." Retrieved 20 May 2015, from http://www.mathworks.com/help/images/ref/registration.metric.meansquares-class.html.

MathWorks, R. a. "rgb2hsv." Retrieved 3 June, 2015, from http://www.mathworks.com/help/matlab/ref/rgb2hsv.html.

MathWorks, R. a. "rgb2ycbcr." Retrieved 3 June, 2015, from http://www.mathworks.com/help/images/ref/rgb2ycbcr.html.

MathWorks, R. a. "smooth3." Retrieved 10 June, 2015, from http://www.mathworks.com/help/matlab/ref/smooth3.html.

MathWorks, R. a. "ycbcr2rgb." Retrieved 3 June, 2015, from http://www.mathworks.com/help/images/ref/ycbcr2rgb.html.

Maxwell, J. C. and Q. Zaidi (1993). "On the Theory of Compound Colours, and the Relations of the Colours of the Spectrum." Color Research & Application 18(4): 270-287.

Michelle Peckham, A. K., Steve Paxton. (2003). "The Histology Guide." Retrieved 02 February, 2015, from http://histology.leeds.ac.uk/.

Mosaliganti, K., T. Pan, R. Sharp, R. Ridgway, S. Iyengar, A. Gulacy, P. Wenzel, A. de Bruin, R. Machiraju and K. Huang (2006). Registration and 3d visualization of large microscopy images. Proc. of SPIE Vol.

Muja, M. and D. G. Lowe (2012). Fast matching of binary features. Computer and Robot Vision (CRV), 2012 Ninth Conference on, IEEE.

Nakhleh, R. E. (2008). "Patient safety and error reduction in surgical pathology." Archives of pathology & laboratory medicine 132(2): 181.

Namati, E., J. De Ryk, J. Thiesse, Z. Towfic, E. Hoffman and G. Mclennan (2007). "Large image microscope array for the compilation of multimodality whole organ image databases." The Anatomical Record 290(11): 1377-1387.

Nedzved, A., A. Belotserkovsky and S. Ablameyko (2005). "Computer systems of histology image analysis in Belarus." Endocrinology 3: 5.

Oliveira, F. P. and J. M. R. Tavares (2014). "Medical image registration: a review." Computer methods in biomechanics and biomedical engineering 17(2): 73-93.

Otsu, N. (1975). "A threshold selection method from gray-level histograms." Automatica 11(285-296): 23-27.

Ourselin, S., A. Roche, G. Subsol, X. Pennec and N. Ayache (2001). "Reconstructing a 3D structure from serial histological sections." Image and vision computing 19(1): 25-31.

Paulsson, M. (1992). "Basement Membrane Proteins: Structure, Assembly, and Cellular Interactions." Critical Reviews in Biochemistry and Molecular Biology 27(1-2): 93-127.

Pelizzari, C. A., G. T. Chen, D. R. Spelbring, R. R. Weichselbaum and C.-T. Chen (1989). "Accurate three-dimensional registration of CT, PET, and/or MR images of the brain." Journal of computer assisted tomography 13(1): 20-26.

Pennec, X., P. Cachier and N. Ayache (1999). Understanding the “demon’s algorithm”: 3D non-rigid registration by gradient descent. Medical Image Computing and Computer-Assisted Intervention–MICCAI’99, Springer.

Perry, C. N., D. P. Cartamil, D. Bernal, C. A. Sepulveda, R. J. Theilmann, J. B. Graham and L. R. Frank (2007). "Quantification of red myotomal muscle volume and geometry in the shortfin mako shark (Isurus oxyrinchus) and the salmon shark (Lamna ditropis) using T1-weighted magnetic resonance imaging." Journal of morphology 268(4): 284-292.

Petrie, I., A. Flynn, R. Pedley, A. Green, E. El-Emir, J. Dearling, G. Boxer, R. Boden and R. Begent (2002). "Spatial accuracy of 3D reconstructed radioluminographs of serial tissue sections and resultant absorbed dose estimates." Physics in medicine and biology 47(20): 3651.

Pham, D. L., C. Xu and J. L. Prince (2000). "Current methods in medical image segmentation 1." Annual review of biomedical engineering 2(1): 315-337.

Prima, S., N. Ayache, T. Barrick and N. Roberts (2001). Maximum likelihood estimation of the bias field in MR brain images: Investigating different modelings of the imaging process. Medical Image Computing and Computer-Assisted Intervention–MICCAI 2001, Springer.

Ramaprabha, R., M. Balaji and B. Mathur (2012). "Maximum power point tracking of partially shaded solar PV system using modified Fibonacci search method with fuzzy controller." International Journal of Electrical Power & Energy Systems 43(1): 754-765.

Randell, R., G. Hutchins, J. Sandars, T. Ambepitiya, D. Treanor, R. Thomas and R. Ruddle (2012). Using a high-resolution wall-sized virtual microscope to teach undergraduate medical students. CHI'12 Extended Abstracts on Human Factors in Computing Systems, ACM.

Randell, R., R. A. Ruddle, C. Mello-Thoms, R. G. Thomas, P. Quirke and D. Treanor (2013). "Virtual reality microscope versus conventional microscope regarding time to diagnosis: An experimental study." Histopathology 62(2): 351-358.

Randell, R., R. A. Ruddle, R. Thomas and D. Treanor (2012). "Diagnosis at the microscope: a workplace study of histopathology." Cognition, Technology & Work 14(4): 319-335.

Rehorek, S. and T. Smith (2007). "Concurrent 3-D visualization of multiple microscopic structures." Modern Research and Educational Topics in Microscopy no 3: 917-923.

Reza, A. M. (2004). "Realization of the contrast limited adaptive histogram equalization (CLAHE) for real-time image enhancement." Journal of VLSI signal processing systems for signal, image and video technology 38(1): 35-44.

Roberts, N., D. Magee, Y. Song, K. Brabazon, M. Shires, D. Crellin, N. M. Orsi, R. Quirke, P. Quirke and D. Treanor (2012). "Toward routine use of 3D histopathology as a research tool." The American journal of pathology 180(5): 1835-1842.

Rueckert, D., L. I. Sonoda, C. Hayes, D. L. Hill, M. O. Leach and D. J. Hawkes (1999). "Nonrigid registration using free-form deformations: application to breast MR images." Medical Imaging, IEEE Transactions on 18(8): 712-721.

Ruifrok, A. C. and D. A. Johnston (2001). "Quantification of histochemical staining by color deconvolution." Analytical and quantitative cytology and histology/the International Academy of Cytology [and] American Society of Cytology 23(4): 291-299.

Schroeder, W., K. Martin and B. Lorensen (2003). "The visualization toolkit: an object oriented approach to 3D graphics. New York: Kitware." Inc. Publisher 156.

Sertel, O., U. V. Catalyurek, H. Shimada and M. Guican (2009). Computer-aided prognosis of neuroblastoma: Detection of mitosis and karyorrhexis cells in digitized histological images. Engineering in Medicine and Biology Society, 2009. EMBC 2009. Annual International Conference of the IEEE, IEEE.

Sertel, O., J. Kong, U. V. Catalyurek, G. Lozanski, J. H. Saltz and M. N. Gurcan (2009). "Histopathological image analysis using model-based intermediate representations and color texture: Follicular lymphoma grading." Journal of Signal Processing Systems 55(1-3): 169-183.

Shea, S. M. (1979). "Glomerular hemodynamics and vascular structure: The pattern and dimensions of a single rat glomerular capillary network reconstructed from ultrathin sections." Microvascular research 18(2): 129-143.

Sørensen, T. (1948). "{A method of establishing groups of equal amplitude in plant sociology based on similarity of species and its application to analyses of the vegetation on Danish commons}." Biol. Skr. 5: 1-34.

Studholme, C., D. L. Hill and D. J. Hawkes (1996). "Automated 3-D registration of MR and CT images of the head." Medical image analysis 1(2): 163-175.

Tabesh, A., M. Teverovskiy, H.-Y. Pang, V. P. Kumar, D. Verbel, A. Kotsianti and O. Saidi (2007). "Multifeature prostate cancer diagnosis and Gleason grading of histological images." Medical Imaging, IEEE Transactions on 26(10): 1366-1378.

Teot, L. A., R. Sposto, A. Khayat, S. Qualman, G. Reaman and D. Parham (2007). "The problems and promise of central pathology review: development of a standardized procedure for the children's oncology group." Pediatric and Developmental Pathology 10(3): 199-207.

Thirion, J.-P. (1998). "Image matching as a diffusion process: an analogy with Maxwell's demons." Medical image analysis 2(3): 243-260.

Torr, P. H. and A. Zisserman (2000). "MLESAC: A new robust estimator with application to estimating image geometry." Computer Vision and Image Understanding 78(1): 138-156.

Treanor, D., N. Jordan-Owers, J. Hodrien, J. Wood, P. Quirke and R. A. Ruddle (2009). "Virtual reality Powerwall versus conventional microscope for viewing pathology slides: an experimental comparison." Histopathology 55(3): 294-300.

Unpublished, W. (2015). A Discriminative Framework for Stain Deconvolution of Histopathology Images in the Maxwellian Space.

Vercauteren, T., X. Pennec, A. Perchant and N. Ayache (2009). "Diffeomorphic demons: Efficient non-parametric image registration." NeuroImage 45(1): S61-S72.

Vernon, D. (1991). Machine vision-Automated visual inspection and robot vision, Prentice Hall.

Wang, H., L. Dong, J. O'Daniel, R. Mohan, A. S. Garden, K. K. Ang, D. A. Kuban, M. Bonnen, J. Y. Chang and R. Cheung (2005). "Validation of an accelerated'demons' algorithm for deformable image registration in radiation therapy." Physics in medicine and biology 50(12): 2887.

Watson, M. L. (1958). "Staining of tissue sections for electron microscopy with heavy metals." The Journal of Biophysical and Biochemical Cytology 4(4): 475-478.

Weszka, J. S. (1978). "A survey of threshold selection techniques." Computer Graphics and Image Processing 7(2): 259-265.

Xu, R. and D. Wunsch (2005). "Survey of clustering algorithms." Neural Networks, IEEE Transactions on 16(3): 645-678.

Zitova, B. and J. Flusser (2003). "Image registration methods: a survey." Image and vision computing 21(11): 977-1000.